THE LINK BETWEEN HEMODYNAMICS AND WALL STRUCTURE IN CEREBRAL ANEURYSMS

by

Xinjie Duan

B.S., Tsinghua University, 2007

M.S., Tsinghua University, 2010

Submitted to the Graduate Faculty of

Swanson School of Engineering in partial fulfillment

of the requirements for the degree of

Doctor of Philosophy

University of Pittsburgh

2016

UNIVERSITY OF PITTSBURGH

SWANSON SCHOOL OF ENGINEERING

This dissertation was presented

by

Xinjie Duan

It was defended on

December 17, 2015

and approved by

Juan R. Cebral, Ph.D., Professor, Department of Bioengineering, George Mason University

Giovanni P. Galdi, Ph.D., Professor, Department of Mechanical Engineering and Materials Science

William S. Slaughter, Ph.D., Associate Professor, Department of Mechanical Engineering and Materials Science

David A. Vorp, Ph.D., Professor, Department of Bioengineering

Dissertation Director: Anne M. Robertson, Ph.D., Professor, Department of Mechanical Engineering and Materials Science

THE LINK BETWEEN HEMODYNAMICS AND WALL STRUCTURE IN CEREBRAL ANEURYSMS

Xinjie Duan, PhD

University of Pittsburgh, 2016

Intracranial aneurysms (IAs) are pathological enlargements of the walls of cerebral arteries. Rupture of aneurysms causes 80% of subarachnoid hemorrhages. It is generally accepted that the abnormal hemodynamics within the aneurysm sac can lead to a breakdown in the normal process of collagen renewal and remodeling leaving the aneurysm vulnerable to rupture. However, the link between hemodynamics and wall integrity, as well as the underlying mechanisms governing the aneurysm pathophysiology remain poorly understood.

To investigate the variability of wall structure and mechanical properties within the human unruptured aneurysms, we performed uniaxial mechanical testing on samples resected from aneurysm walls with simultaneous multiphoton microscopy imaging of collagen structure. Significant variations in collagen architecture and mechanical response were found in unruptured aneurysms. Factor of Safety (FoS) was used to quantitatively assess the structural integrity of aneurysms, and subcategorize the unruptured population.

In order to further improve the assessment of the structural integrity of the unruptured population, intramural stresses were obtained from FEA with patient-specific models and used for FoS estimation. In this case study, histological investigation of ECM suggests that aneurysms with high FoS are capable of bearing biaxial loading with collagen fibers in two main directions inside the wall and dispersed on the abluminal side. The robust IAs display a rich cell content

that is distributed into distinct layers. The collagen architecture in these layers displays similar functional roles to the medial and adventitial layers of the control basilar artery.

To study the connection between aneurysmal hemodynamic conditions and the mechanical properties of the aneurysms wall, we constructed computational fluid dynamics models from 3DRA images. Statistically significant correlations between hemodynamic quantities and failure characteristics and high strain stiffness of the wall were found.

In order to assess the correlation between local hemodynamics and local wall structure, we developed a methodology for mapping the resected aneurysm sample onto a reconstruction of the lumen. Local collagen structure was accessed at multiple areas, and was correlated with the local hemodynamics. In the case study used to illustrate this methodology, high wall shear stress was found to be associated with sparse, inhomogeneous fiber architectures.

TABLE OF CONTENTS

LIST OF TABLES

LIST OF FIGURES

PREFACE

This dissertation could not have been possible without the help and support from many people. Foremost, I would like to express my deepest gratitude to my advisor Dr. Anne M. Robertson, for her tremendous support and guidance throughout this research work. Her advice on both research and career development have been invaluable to me. I am very grateful for her enthusiasm, patience, and knowledge in biomechanics and aneurysm area. She has set an excellent example for me as a great scientist and mentor.

I would like to thank my committee members, Dr. Juan Cebral, Dr. Giovanni Galdi, Dr. William Slaughter and Dr. David Vorp for serving on my dissertation committee and their brilliant suggestions and comments.

I am very thankful to our collaborators in Dr. Cebral's group at George Mason University. Dr. Cebral provided significant support on computational fluid dynamics study of aneurysmal hemodynamics and valuable suggestions on my research.

I would also like to thank our collaborators in Dr. Khaled Aziz's group at Allegheny General Hospital. Dr. Aziz provided human aneurysm tissue harvested following surgical clipping, which was extremely crucial for this research work.

I wish to thank the Alzheimers Disease Research Center (ADRC) of the University of Pittsburgh and Dr. Julia K. Kofler, Director of the Neuropathology Core of the ADRC for providing the cadaveric human cerebral vessels that were used in this study.

My gratitude is also extended to the Center for biologic imaging (CBI), Dr. Simon Watkins, director of the CBI, Greg Gibson, Mark Ross and Callen Wallace for training and technical support on microcopies used in this work.

I want to thank Aerotech and Dr. Stephen Ludwick for providing high-precision linear actuators that were used for development of mechanical testing devices.

I am grateful to my colleagues in our lab Dr. Mike Hill, Dr. Zijing Zeng, Mike Durka, Fangzhou Cheng, Piyusha Gade, Chao Sang for help, collaborations, discussions and sharing experience. I also wish to acknowledge Joshua Selling, a talented undergraduate student, for his development and implementation of a meticulous protocol for fiber diameter measurements.

I appreciate the grant support from the National Institute of Neurological Disorders and Stroke of the National Institute of Health (1R21NS080031-01A1).

Lastly, I would like to give my most sincere appreciation to my family for all their love and encouragement. For my parents and parents in law who consistently supported me throughout my Ph.D. study. And most of all for my beloved wife and best friend, Xiaoli Yang, whose love, support and constant encouragement helped me through the hard times in those years.

Dedicated to my wife Xiaoli Yang and my daughter Zoe Duan.

1.0 INTRODUCTION

Intracranial aneurysms are focal dilatations of the wall of cerebral arteries, with prevalence in 2% to 8% of adult population [1-4]. 80% to 85% of intracranial aneurysms are located in the anterior circulation, most frequently found at the junction of the internal carotid artery and posterior communicating artery, the anterior communicating-artery complex, and the trifurcation of middle cerebral artery, Figure 1. In the posterior circulation, the basilar artery bifurcation is the most common location of aneurysm [5]. Although the rupture rate of incidental aneurysms is very low (estimated at 0.3-3% per year), rupture of aneurysms causes 80% of subarachnoid hemorrhages (SAH), which is a major clinical problem in the United States, with occurrence of approximately 1 in 10000 people each year. The mortality rate of SAH from ruptured aneurysm is ~50%, including 12% pre-hospital deaths, and one-third of survivors suffer morbidity [6-9].

The management of unruptured aneurysms is controversial, because the risk associated with treatment options, including surgical clipping and endovascular therapies, can exceed the natural risk of rupture [10-12]. Therefore, treatment or observation is the important decision clinicians and patients often have to make. Aneurysm size, location, aspect ratio, and presence of bleb or blister morphology, as well as patient's age, family history and smoking status are used in assessing the development, enlargement and rupture of intracranial aneurysms [13-18]. Although aneurysm size is widely used as a measure for evaluating rupture risk, a significant number of aneurysms smaller than the critical size (7 mm) were ruptured in previous studies,

indicating size is insufficient as a single parameter to assess rupture risk [13, 19]. Improving the clinical management of aneurysm requires an understanding of the underlying mechanisms governing the development, enlargement and rupture of cerebral aneurysms.

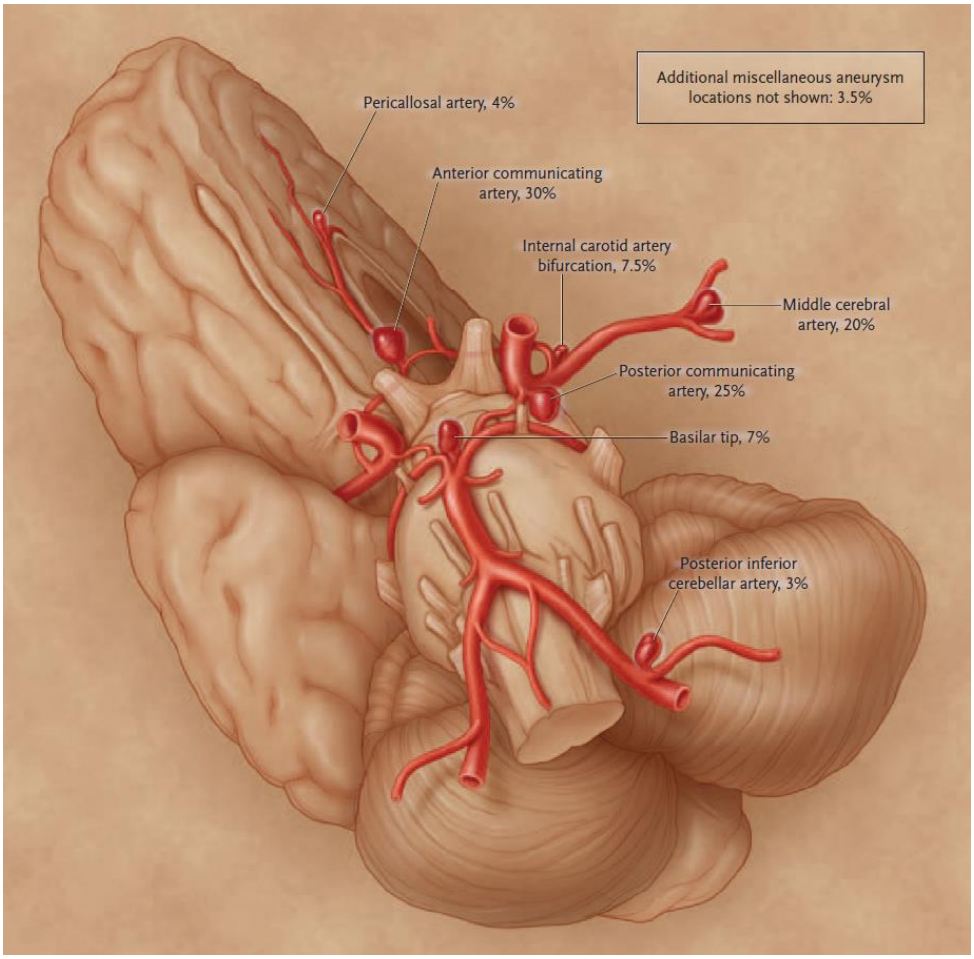

Figure 1. Circle of Willis, showing the most frequent locations of intracranial aneurysms and their corresponding incidence (Reproduced with permission from [1], Copyright Massachusetts Medical Society).

It is commonly accepted that the natural history of cerebral aneurysms is driven by flow-induced progressive degradation of the wall [20-22]. Histological analysis of resected human aneurysm tissue suggested that abnormal aneurysmal flow conditions likely cause endothelial dysfunction, which induces accumulation of cytotoxic and pro-inflammatory substances in the wall as well as thrombus formation, that leads to loss of mural cells and wall degeneration [21].

However, the mechanisms and interactions between the various factors involved in the evolution of IAs remain poorly understood [20].

A large body of research has been focused on identifying a link between rupture and hemodynamic parameters such as magnitude of wall shear stress (WSS) and oscillatory shear index (OSI) [23-29]. However, to date these results are inconsistent and have not identified a clinically useful hemodynamic marker. An underlying assumption of this past work is the cells necessary to sense and respond to hemodynamic loads exist within the aneurysm sac. However, this has been shown not to be the case. In a large percentage of aneurysms, the endothelium is missing [21]. In many of these aneurysms, the wall is hypo-cellular and hence has lost its capacity for wall maintenance and remodeling. Clearly, there are different stages of aneurysm pathology, with some stages lacking the means to sense and respond to hemodynamic loading [30]. The interconnection between intra-aneurysmal hemodynamics and wall structure has never been studied. Until we have a more integrated understanding of hemodynamics, wall structure and wall strength, it is unlikely we will be able use patient specific hemodynamics to gauge rupture risk.

The current approach is generally binary, looking for correlation between hemodynamics parameters and rupture status (rupture/unrupture). This binary approach is questionable since all unruptured aneurysms are lumped together in one group even though some unruptured aneurysms may rupture at any time. There is substantial heterogeneity within the unruptured walls demonstrating that a continuum ranking of some kind or at least sub-classification would be more appropriate than a binary scoring.

There are at least three categories of unruptured aneurysm wall with great variability in intramural structure including cellular content and organization: (A) endothelialized wall with

linearly organized SMC, (B) thickened wall with disorganized smooth muscle cells (SMC), and (C) hypocellular wall with either myointimal hyperplasia or organizing luminal thrombosis, as shown in Figure 2 A, B, and C. The extracellular matrix is manufactured by SMCs and fibroblast cells, so we would expect the heterogeneity in collagen architecture and therefore mechanical properties within the unruptured aneurysms due to this variability in mural content.

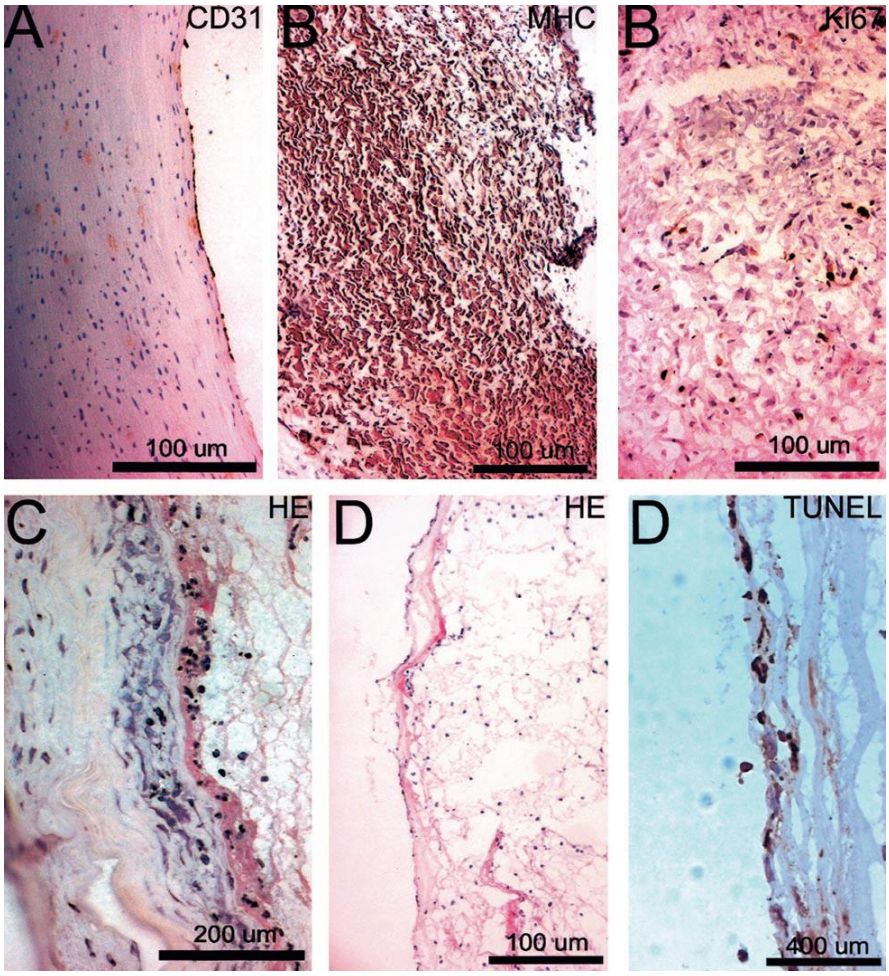

Figure 2. Four aneurysm wall types identified. A, Endothelialized wall with linearly organized SMCs; B, Thickened wall with disorganized SMC; C, Hypocellular wall with either intimal hyperplasia or organizing luminal thrombosis; D. An extremely thin thrombosis-lined hypocellular wall. Only type D is 100% associated with ruptured aneurysms. (Reproduced with permission from [21], Copyright Wolters Kluwer Health, Inc.)

A large variety of flow patterns in unruptured aneurysms was found [25-27]. Four flow types with very difference inflow and vortex characteristics were reported by Cebral et al. in unruptured aneurysms, unchanging direction of inflow jet with one vortex; unchanging direction of inflow jet with multiple associated vortices lasting during the whole cardiac cycle; changing direction of inflow jet with one vortex; changing direction of the inflow jet with creation or destruction of multiple vortices [27]. More recently, Cebral's group has developed a quantitative method for scoring IA flows [31].

Although mechanical properties of the aneurysm wall have been hardly investigated, differences in failure properties have been reported. Two unruptured aneurysms were pressurized to failure and large inter-specimen variation in mechanical strength was found by Scott et al. [32]. One aneurysm ruptured at transmural pressure of 325 mmHg (estimated failure stress of 0.31 MPa), and the other aneurysm was pressurized up to 550 mmHg without rupture. An average failure stress of 0.50 MPa with standard deviation of 0.26 MPa in uniaxial tests of 7 aneurysms was reported [33]. In another study of uniaxial mechanical tests of aneurysm wall, the failure stress ranges from 0.14 to 0.93 MPa for samples in the circumferential direction and 0.34 to 1.00 MPa for samples in meridional direction [34].

In order to rank the unruptured population, a metric is needed to assess which of these aneurysms are more vulnerable to rupture. Wall strength alone is not sufficient because rupture of the aneurysm wall is a local failure that occurs when the local stress exceeds the local strength of the wall. This indicates that a score of mechanical integrity of aneurysm could be used for assessing the vulnerability of unruptured population. Therefore, aneurysm specific intramural stress and wall strength are needed for identifying the vulnerable aneurysms. Differences in

aneurysm shape, wall thickness as well as transmural pressure result in different levels of intramural stress between patients.

Moreover, the transmural pressure may vary in time due to physical or physiological stress. In a study of five men performing heavy lifting, the average peak arterial pressure was 320/250 mmHg, with one subject's pressure rising above 480/350 mmHg [35]. The effect of acute physiological pressure was reported in a rare situation, where a male patient with hypertension was attacked by an assaulter with a knife, and the blood pressure was recorded by ambulatory blood pressure monitor. During the incident the systolic pressure rose from 190 mmHg to 312 mmHg [36, 37]. This is relevant with the fact that rupture has been found to be associated with activities that increase the mechanical load on the wall. In another study, 42.8% of ruptures in 445 patients were associated with physical or emotional stress [38]. In one study of 250 patients, 8 triggers have been found for rupture, and all of them involved sudden, short increases in pressure [39].

The factor of safety (FoS) is a frequently used quantity for estimation of structural integrity in engineering design. It is defined as a ratio of structural capacity to the applied loads, in other words the ratio of the ultimate stress of the material to the maximum stress expected to be borne by the material. The FoS provides a direct measure of how over designed the system is. Namely, how many times larger the wall strength is compared with the expected maximum stress that will be experienced. In cases of the resected aneurysm tissue, mechanical tests can be performed to assess the mechanical properties including mechanical strength. The local loads within the body are a result of the bulk loads on the body and the design of the body which in the case of the aneurysm refers to the geometry including wall thickness and size. The spatial and time dependent quantities (von Mises stress, wall tension, deformation, etc) can then be

determined using the finite element method. Isaksen et al. analyzed wall tension and wall displacement in aneurysms using a fluid-structure interaction model with patient specific geometry, and the area of high wall tension and wall displacement was found to be located at the rupture site [40]. In another study, based on the numerical simulations with different material properties, volume variation has been suggested to be used as a biomechanical index to identify aneurysms at risk for rupture [41]. The FoS has been used for rupture risk assessment of abdominal aortic aneurysm (AAA) as well. Vorp et al. developed a four-parameter statistical model for the noninvasive estimation of AAA wall strength distribution based on failure mechanical tests and patient clinical data. Patient specific rupture potential of AAA was then assessed using a statistical modeling of wall strength and finite element analysis of wall stress [42, 43].

The overall objective of the present work is to better understand how hemodynamics are tied to wall structure (cellular and extra-cellular) and thereby to wall strength in human cerebral aneurysms, and to assess the structural integrity of aneurysm. This objective is broken down into the following three specific aims:

- To assess the variability of wall structure and structural integrity in unruptured human IAs, and to determine what types of wall structures are associated with high structural integrity
- To determine how wall extracellular matrix (ECM) structure and mechanical properties depend on global hemodynamic characteristic in human IAs
- To determine how local ECM structure depends on local hemodynamics in human IAs

To achieve the first specific aim, in Chapter 2, the aneurysm domes are resected and mechanically tested to failure with a uniaxial testing system under multiphoton microscopy in order to assess the wall structure and wall mechanical properties in human IAs. In Chapter 3,

wall stress in aneurysms is estimated using patient-specific biomechanical models, and FoS is used to evaluate the structural integrity of the wall. Furthermore, ECM and cellular content are investigated using multiphoton imaging and immunohistochemistry staining, and this data is then used to determine the wall structure associated with the high structural integrity n a case study of two aneurysms..

To achieve the second specific aim, in Chapter 4, the in vivo hemodynamic environment is estimated from image-based patient-specific computational fluid dynamics (CFD). Statistical analysis is performed to explore the correlations between global hemodynamic parameters and the mechanical characteristics of the wall.

To achieve the third specific aim, in Chapter 5, a methodology is developed to enable local flow dynamics to be mapped to data for wall structure obtained for the resected aneurysm domes. This mapping is then illustrated for data on collagen orientation, obtained using multiphoton imaging.

2.0 INVESTIGATION OF SPECTRUM OF WALL STRUCTURE AND MECHANICAL PROPERTIES IN UNRUPTURED POPULATION OF INTRACRANIAL ANEURYSMS

2.1 ABSTRACT

A major issue in treatment of cerebral aneurysms is risk stratification of presenting aneurysm cases. Namely, the identification of aneurysms at risk for rupture that warrant treatment rather than close monitoring. A major focus of engineering studies on cerebral aneurysms is improved risk stratification using measurable clinical parameters such as aneurysm flow dynamics and aneurysm geometry. These studies [23] are largely directed at looking at correlations between hemodynamic and geometric parameters and rupture status. In this approach, unruptured aneurysms are lumped together in one group even though some aneurysms which are unruptured may be vulnerable to rupture, either due to continued wall degradation or when exposed to significant mechanical triggers such as increased transmural pressure. In fact, any ruptured aneurysm would have been categorized as unruptured just before it ruptured. In this section, we discuss the variability in mechanical properties and wall structure within even the unruptured population of aneurysm walls. Eight unruptured aneurysm domes were harvested after surgical clipping and imaged under multiphoton microscopy for accessing the wall structure while being mechanical tested to failure with a custom designed uniaxial testing system. The extracellular

matrix and wall mechanical properties were accessed, and aneurysm wall was categorized by wall strength. Using this data, we then considered an alternate method of stratifying aneurysm walls based on a structural integrity index rather than rupture status. The majority of the content of this chapter was previously published in Annals of Biomedical Engineering, 2015 Jul;43(7):1502-15. The permission of republishing the material in this PhD dissertation was granted by Springer. Mechanical testing data and multiphoton images for additional cases were included in this chapter.

2.2 BACKGROUND

Prior studies have already shown a large variability in the intramural content in even unruptured aneurysm walls, supporting our conjecture that wall mechanical properties and structure vary in the unruptured population. In particular, Frösen et al. evaluated the wall structure of human aneurysms domes, and categorized the aneurysm wall based on classical histological findings. Four types of aneurysm wall were identified, as shown in Figure 2. Unruptured aneurysms displayed three of the four wall types (A, B, C in Figure 2), namely a great variability in intramural structure [21]. Since the intramural SMCs and fibroblast cells play a vital role in collagen manufacture, we would anticipate the differences in mural content would be associated with differences in collagen matrix and hence mechanical properties within the unruptured population.

Mechanical properties of cerebral aneurysm wall have been rarely studied. Scott et al. found the mechanical strength of unruptured aneurysms has large inter-specimen variation. Two aneurysms were pressurized to failure. A 5 mm aneurysm ruptured experimentally at transmural

pressure of 325 mmHg, giving an estimated failure stress of 0.31 MPa, while a 6 mm aneurysm was able to maintain the pressure up to 550 mmHg [32]. Steiger et al. measured an average failure stress of 0.50 MPa with standard deviation of 0.26 MPa in uniaxial tests of cerebral aneurysm fundi [33]. Toth et al. carried out uniaxial tests of aneurysm wall, and reported the failure stress ranging 0.14 to 0.93 MPa for strips taken in the circumferential direction and 0.34 to 1.00 MPa for those aligned in meridional direction [34].

In looking for a means to subcategorize the unruptured population it is necessary to assess which of these aneurysms are more vulnerable to rupture. Rupture occurs when the intramural stress exceeds wall strength. Hence, it is not sufficient to study just the variability in material strength to identify vulnerable aneurysms; we must consider the aneurysm specific intramural stress. The in-vivo intramural stress will vary between unruptured aneurysms due to differences in aneurysm geometry as well as differences in transmural pressure between patients. A quantitative assessment of structural integrity called factor of safety is commonly used in structural design. It is defined as a ratio of structural strength to design load. FoS has been used for rupture risk assessment of abdominal aortic aneurysms [42, 43]. In the following sections, we will return to the use of this structural integrity index to assess vulnerability of cerebral aneurysms.

2.3 MATERIALS AND METHODS

2.3.1 Aneurysm tissue retrieval and handling

Aneurysm domes were harvested following surgical clipping in consented patients being treated for unruptured aneurysms at the Allegheny General Hospital. The harvested tissue was placed in a vial of saline solution, stored in an insulated cooler and transported to the University of Pittsburgh. Mechanical testing was performed on aneurysm samples within 48 hours. The protocols for patient consent, handling of patient data, tissue harvest, and analysis were approved by the institutional review boards (IRB) at both the Allegheny General Hospital and the University of Pittsburgh. While 47 patients were consented for the study, based on clinical decisions at the time of treatment, tissue was harvested from 16 patients.

Human basilar arteries (n=6) and internal carotid arteries (n=6) were obtained from the circles of Willis of human cadavers from patients that died from causes unrelated to cerebral aneurysms (Brain Bank of the University of Pittsburgh). The Circles of Willis were harvested from these cadavers during autopsy, snap frozen and stored at -80C. Prior to testing, the tissue was thawed at room temperature and circumferential sections removed. Human cadaveric arteries were obtained using protocols approved by CORID.

2.3.2 Patient clinical data

Clinical data was collected for each patient including gender, age, and family history of IAs. Lifestyle and health information including cigarette smoking, hypertension, diabetes mellitus and treatment with statins were obtained. Patients were considered positive for hypertension if they

were currently being treated for hypertension or if they were previously diagnosed with hypertension but declined treatment. Smoking status was reported with respect to packs of cigarettes per week. Patients were categorized as nonsmokers if they had never smoked cigarettes or had not smoked within the last five years. Patients who currently smoked or who had quit within the last five years were categorized as smokers. Notation was made of patients who used smokeless tobacco (snuff). Assessment of number of aneurysms, SAH status and aneurysm location was made from CT scan. In cases of multiple aneurysms, choice of aneurysm for tissue harvest was based on patient need. The control arteries were obtained from 8 male and 4 female cadavers with an average age of 80.8 ± 10.6.

2.3.3 Morphology assessment

Vascular models of the aneurysm and surrounding arteries were constructed from 3D rotational angiography images. Unstructured volumetric grids composed of tetrahedral elements were generated to fill the interior of the vascular models. The mesh resolution was approximately 0.2 mm. The aneurysm neck was delineated by connecting points interactively selected on the vascular reconstructions following paths of minimal geodesic distance. The aneurysm orifice, defined by the neck contour, was triangulated and used to label mesh points on each side as "aneurysm" or "parent artery". The following geometric quantities were then calculated (see, [44] for further details of these definitions): 1) aneurysm volume: computed by adding the volume of all tetrahedral elements within the aneurysm region; 2) aneurysm surface area: computed by summing the area of all triangles of the surface mesh within the aneurysm region; 3) equivalent sac diameter: diameter of a sphere of volume equal to the aneurysm volume. 4) maximum aneurysm size: computed as the maximum Euclidean distance between any two points

in the aneurysm region; 5) aneurysm depth (sometimes referred to as height): computed as the length of the maximal path from any aneurysm point to the orifice surface; 6) neck area: computed by adding the areas of all the triangles of the orifice surface; 7) neck maximum size: computed as the maximum Euclidean distance between any two points on the orifice surface; and 8) aspect ratio: defined as the ratio between the aneurysm depth over the maximum aneurysm neck size. This morphology assessment was done by Dr. Juan Cebral's group at George Mason University.

2.3.4 Mechanical testing protocol

Aneurysm and artery wall samples were tested in a custom designed uniaxial loading system compatible with an Olympus FV1000 MPE multiphoton microscope (Tokyo, Japan) [45]. Using this UA-MPM system, it is possible to simultaneously perform mechanical testing and structural imaging under MPM (Section 2.3.5). Rectangular strips of the aneurysm were obtained in the meridional direction. Circumferential strips of artery were cut from cerebral arteries from the human cadaveric circles of Willis. Unloaded wall thickness was defined as the average of wall thickness measured at five positions using micro-calipers. The test samples were gripped by mechanical clamps and placed in a bath of 0.9% (weight/volume) saline at room temperature in the UA-MPM system. Fine-grade sandpaper was adhered to tissue-contacting surfaces on the UA-MPM device to avoid the need for adhesives. 9 of the 15 samples met the minimum size of 4mm × 5mm necessary for mechanical testing.

Specimens were subjected to uniaxial extension at a speed of 20 um/s along the meridional direction for aneurysm and circumferential direction for artery. Displacement was controlled by a linear actuator (ANT-25LA, Aerotech, PA), and force was recorded with a 5 lb

load cell (MDB-5, Transducer Techniques, Rio Nedo Temacula, CA). Force versus displacement curves were obtained after five cycles of preconditioning to 0.3 N and used to calculate Cauchy stress as a function of strain. Zero strain was defined as the configuration of the tissue under 0.005N load. Current area was calculated from the unloaded cross sectional area and longitudinal strain assuming an isochoric deformation. For purposes of quantitative comparison between samples, a simple exponential model for the strain energy function (per unit volume) was fit to the mechanical data

$$W = \frac{C_1}{2C_2}(e^{C_2(I_1-3)^2} - 1) \quad (1)$$

The loading curves were broken into four regions, a nearly linear toe region (low strain response), a transition region, a nearly linear post transition-pre-failure region (high strain response), and a sub-failure region. Low strain stiffness was defined as the slope of a linear fit for the toe region, and high strain stiffness as the slope of a linear fit for the high strain region (in the post-transition and pre-failure region). The transition stretch was defined as that corresponding to the point of intersection of the two fitted lines.

2.3.5 Multiphoton imaging and post-processing

Collagen and elastin content in the samples were assessed using multiphoton microscopy (MPM). An Olympus FV1000 MPE (Tokyo, Japan) equipped with a Spectra-Physics DeepSee Mai Tai Ti-Sapphire laser (Newport, Mountain View, CA) with an 1.12NA 25x MPE water immersion objective was used for all samples. The excitation wavelength was 870 nm. The second harmonic generation (SHG) signals from collagen were collected using non-descanned, backscatter epi detectors and 400nm Chroma emission filters with a 50 spectral bin (Brattleboro,

VT). The dwell time was 10 microseconds/pixel at a scan pixel count of 1024X1024. An in plane resolution of 0.12 um was achieved with this system.

The en face images were obtained for fresh samples loaded in the UA-MPM system. Samples were imaged from both luminal and abluminal sides (termed luminal and abluminal images, respectively), with stacks commencing from the layer furthest from the lens and moving upward in 2um intervals. Fiber diameters were measured (Image J) at 15 randomized locations in superposed stacks (Imaris, Bitplane) of MPM images. In cases where fibers were banded, diameters of individual fibers were used (Appendix F).

Images were obtained from some fixed samples that were sectioned in a cross sectional cut in order to assess the collagen architecture across the wall thickness. These samples were fixed in 2% paraformaldehyde in PBS at 4 °C for 4 h, and slowly frozen in liquid nitrogen. Eight micron thick sections were obtained by slicing the sample with a cryostat (HM 505E, Microm). Slides were kept at 20 °C until ready for use.

2.3.6 Statistical analysis

Linear regression analysis was carried out to test for possible correlations between wall thickness and other geometric parameters. The slope of the linear regression was considered significantly different from zero if the corresponding p-values were below 0.05. The non-parametric Wilcoxon test was used to test whether the mean values of material properties of different groups of tissue samples (e.g. aneurysms against control arteries) were statistically different. Differences were considered statistically significant if the p-values were less than 0.05 (95% confidence). All statistical analysis was performed using Matlab.

2.4 RESULTS

2.4.1 Study population

16 unruptured aneurysms were included in this study of which 10 were symptomatic, Table 1. No patients had signs of subarachnoid hemorrhage. 9 of the patients were female and the mean and median patient ages were 59 and 61 respectively. Notably, the patient population included a 27 year old, whose aneurysm was found incidentally and had no other identifiable medical conditions and no reports of drug use. Nine of the patients had multiple aneurysms and five had a family history of aneurysms. Of the resected aneurysms, 9 (56%) were from the middle cerebral artery (MCA), 4 (25%) were from the internal carotid artery (ICA), 2 (13%) were from the anterior cerebral artery ACA and 1 (6%) was from the anterior communicating artery (AcomA).

2.4.2 Morphology of the aneurysm sac and dome

The equivalent diameters of the aneurysms ranged from 4.5 mm to 11mm, Table 2. No correlation was found between wall thickness, which ranged from 130 to 450 μm and any other geometric parameters of the sac in Table 2. In particular, the wall thickness was not linearly related to the aneurysm equivalent diameter.

2.4.3 Subfailure properties

The loading curves for the uniaxial loading tests to failure for 9 aneurysm samples are shown in Figure 3 with a magnified insert to show the low strain region. These curves are shown relative

to the corresponding results for the control cerebral arteries in Figure 4. The loading curves for both the control arteries and aneurysm tissue are qualitatively exponential in shape, with the exception of Sample CA-11, Figure 3. This is consistent with the lower R^2 value for the fit of the exponential hyperelastic strain energy function to the data for CA-11, Table 3.

Table 1. Summary of clinical data for the 15 cases studied.

ID	Location Resected IA	Age	Gender	Symptomatic?	SAH	Family History IA?	No. of IAs	Cigarette Smoker? (Packs/wk)	Hyper-tension?	Diabetic?
CA-1	MCA	61	F	Yes	No	Yes	1	Yes (10)	Yes	No
CA-6	MCA	62	F	Yes	No	No	1	No	No	No
CA-7	MCA	53	M	Yes	No	No	1	Yes (7)	Yes	No
CA-8	ICA	46	F	Yes	No	Yes	2	Yes (7)	No	No
CA-9	ICA	27	M	Incidental	No	Yes	1	-	No	No
CA-11	ICA	63	M	Incidental	No	No	2	No	Yes	Yes
CA-12	MCA	69	M	Incidental	No	Yes	3	No	No	No
CA-15	MCA	69	F	Incidental	No	No	2	Yes (1)	No	No
CA-18	ACA (distal)	56	F	Yes	No	No	4	Yes (7)	No	No
CA-21	ICA	57	M	Yes	No	No	3	Yes (10)	No	No
CA-23	MCA	54	M	Yes	No	No	3	No	No	No
CA-25	AcomA	53	F	Yes	No	Yes	2	No	No	No
CA-26	ACA (distal)	50	M	Yes	No	No	1	No	No	No
CA-39	MCA	61	F	Yes	No	No	4	No	Yes	No
CA-46	MCA	66	F	Incidental	No	No	1	Quit(7)	Yes	No
CA-65	MCA	59	F	Incidental	No	Yes	1	Quit(7)	Yes	No

All aneurysm were unruptured. MCA = Middle Cerebral Artery, AcomA = Anterior Communicating Artery, ICA = Internal Cerebral Artery, ACA = Anterior Cerebral Artery. "Quit" means the patient quit smoking and had not smoked within the last five years.

The toe region for the aneurysm tissue is noticeably shortened relative to the control arteries with a stiffer response than that seen in the control arteries, Figure 4, which is consistent with the lack of internal elastic lamina in the aneurysm tissue (discussed below). The difference in low strain stiffness between the aneurysm and all control arteries is statistically significant with a p-value of 0.021, whereas the high strain stiffness did not reach statistical significance

(p=0.06). There was no statistical difference between the stiffness of the basilar and carotid arteries (p=0.784 for low strain stiffness and p=0.632 for high strain stiffness).

Table 2. Morphology of the aneurysm lumen and wall

	Lumen Morphology								Wall Morphology
ID	Volume (mm^3)	Surface Area (mm^2)	Equiv. Diam. (mm)	Max. An. Size (mm)	An. Depth (mm)	Neck Area (mm^2)	Neck Max. Size (mm)	Aspect Ratio	Wall Thickness (mm)
CA-1	440	275	9.4	11.9	9.3	27.0	6.5	1.4	0.24
CA-6	90	100	5.6	8.0	5.6	20.3	5.2	1.1	0.13
CA-7	110	105	6.0	7.9	6.0	22.4	6.6	0.9	0.23
CA-8	710	405	11.1	16.2	15.0	20.0	5.1	3.0	0.19
CA-9	290	215	8.2	10.6	8.9	24.9	5.7	1.6	0.16
CA-11	215	170	7.5	9.2	7.1	18.3	4.9	1.4	0.21
CA-12	65	80	5.0	7.2	6.2	6.9	3.0	2.0	0.20
CA-15	420	270	9.3	11.6	9.4	36.0	7.0	1.3	0.13
CA-18	45	55	4.3	6.0	4.0	18.5	5.2	8.8	0.22
CA-21	110	110	6.0	7.5	6.3	16.4	4.7	1.3	0.20
CA-23	50	60	4.6	5.56	4.5	12.8	4.3	1.0	0.17
CA-25	45	60	4.5	5.8	6.3	16.4	4.7	1.3	0.24
CA-26	160	145	6.8	9.3	4.5	12.8	4.3	1.0	0.45
CA-39	170	160	6.9	10.3	6.8	22.6	5.7	1.2	0.21
CA-46	493	283	9.8	11.7	9.3	39.8	9.2	1.0	0.30

2.4.4 Failure properties

Failure stress values for the aneurysm tissue fell into distinct low and high failure stress categories, Figure 4. The average failure stress (Cauchy) for the three low strength walls was 0.59 ± 0.16 MPa, Table 3. These three weaker samples (CA-11, CA-15 and CA-65) display two qualitatively different responses, suggesting distinct failure modes. Both CA-15 and CA-65 had shorter toe regions than any of the samples, with an exponential shaped stress strain curve. In

contrast, CA-11 was more linear than all other aneurysm samples, and comparatively stiffer at low strain and softer at high strain. CA-65 has the lowest failure stress, and the medial failure stretch among the three. Samples CA-11 and CA-15 displayed the extremes of high strain stiffness with values of 3.42 MPa and 25.1 MPa, respectively. In contrast, the high failure samples had a mean high strain stiffness of 11.8 ± 4.6 MPa.

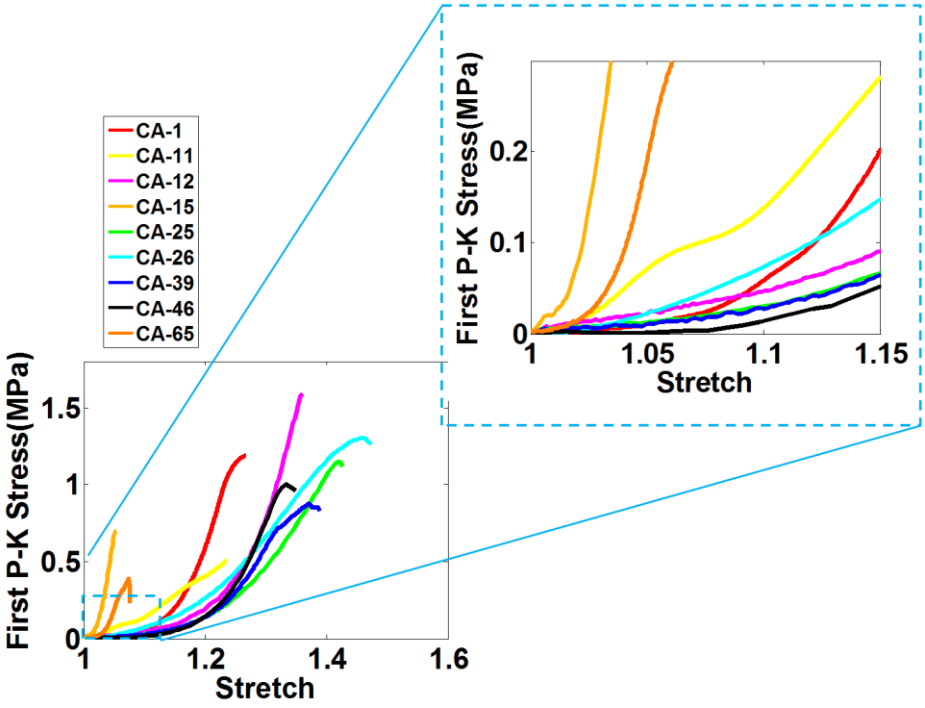

Figure 3. Results for stress (1st Piola-Kirkoff) vs. stretch for the uniaxial loading tests to failure for 9 aneurysm samples. A magnified insert is included to enlarge the low strain region

The high strength aneurysms (CA-1, CA-12, CA-25, CA-26, CA-39, CA-46) displayed a more uniform response. The low strain stiffness had a mean of 0.46 ± 0.28 MPa. The Cauchy ultimate stress of the high strength aneurysms ranged from 1.2 MPa to 2.2 MPa with an average of 1.6 ± 0.36 MPa. The strength of even the high strength aneurysms was significantly lower (p=0.001) than that of the basilar arteries that ranged from 2.7 MPa to 3.3 MPa with an average of 3.0 ± 0.26 MPa and those of the internal carotid arteries from 2.6 to 3.5 MPa with an average

of 3.0 ± 0.29 MPa. Differences between the ultimate stress of basilar and carotid arteries were not statistically significant (p=0.908).

Table 3. Mechanical Properties of Aneurysm Domes and Control Arteries

ID	Trans. Stretch	Low Strain Stiffness (MPa)	High Strain Stiffness (MPa)	Ultimate Stretch	Ultimate Stress (Cauchy) (MPa)	Ultimate Stress (1st PK) (MPa)	Ultimate Tension (kg/s^2)	C_1 (MPa)	C_2	R_2
Aneurysm Domes										
CA-1	1.15	0.37	14.75	1.27	1.50	1.19	285	5.47	1.10	0.986
CA-11	1.10	1.72	3.42	1.24	0.63	0.51	105	3.76	0.54	0.872
CA-12	1.26	0.62	18.84	1.36	2.16	1.59	320	1.79	5.69	0.999
CA-15	1.02	2.10	25.06	1.05	0.73	0.70	90	338.13	0.54	0.962
CA-25	1.23	0.26	8.25	1.42	1.63	1.15	280	1.40	0.68	0.999
CA-26	1.21	0.95	7.37	1.47	1.90	1.30	580	1.84	0.54	0.981
CA-39	1.22	0.33	8.35	1.37	1.20	0.87	183	1.26	7.32	0.999
CA-46	1.23	0.24	12.99	1.33	1.34	1.00	300	1.45	8.38	0.994
CA-65	1.03	0.73	10.68	1.07	0.42	0.39	133	86.6	0.38	0.994
Avg	1.16	0.81	12.19	1.29	1.28	0.97	253	54.23	2.80	
Basilar Arteries										
BA-1	1.52	0.05	5.94	2.16	3.15	1.46	374	0.160	0.224	0.989
BA-2	1.68	0.05	5.36	2.31	3.30	1.43	365	0.096	0.036	0.974
BA-3	1.61	0.04	4.51	2.27	2.65	1.17	255	0.104	0.043	0.990
BA-4	1.77	0.17	7.15	2.27	2.91	1.28	390	0.062	0.174	0.999
BA-5	1.79	0.08	5.44	2.39	3.23	1.35	400	0.071	0.038	0.993
BA-6	1.81	0.05	8.88	2.17	2.79	1.29	430	0.063	0.121	0.951
Avg	1.70	0.08	6.21	2.26	3.01	1.33	369	0.093	0.106	
Internal Carotid Arteries										
ICA-1	1.81	0.06	5.95	2.04	3.15	1.54	400	0.029	0.498	0.996
ICA-2	1.60	0.03	7.10	2.03	2.93	1.45	363	0.071	0.566	0.982
ICA-3	1.64	0.05	3.02	2.15	3.22	1.50	525	0.042	0.209	0.994
ICA-4	1.82	0.07	10.03	2.06	2.58	1.25	413	0.031	0.353	0.996
ICA-5	1.66	0.12	8.68	1.97	2.84	1.45	421	0.110	0.241	0.993
ICA-6	1.56	0.07	6.03	2.10	3.48	1.66	415	0.185	0.101	0.982
Avg	1.68	0.07	6.80	2.06	3.03	1.47	423	0.08	0.33	

BA: basilar artery; ICA: internal carotid artery, adjacent to circle of Willis.

While the stress provides information about the material properties, failure tension, which is equal to the product of the failure stress (engineering) and unloaded thickness, provides a

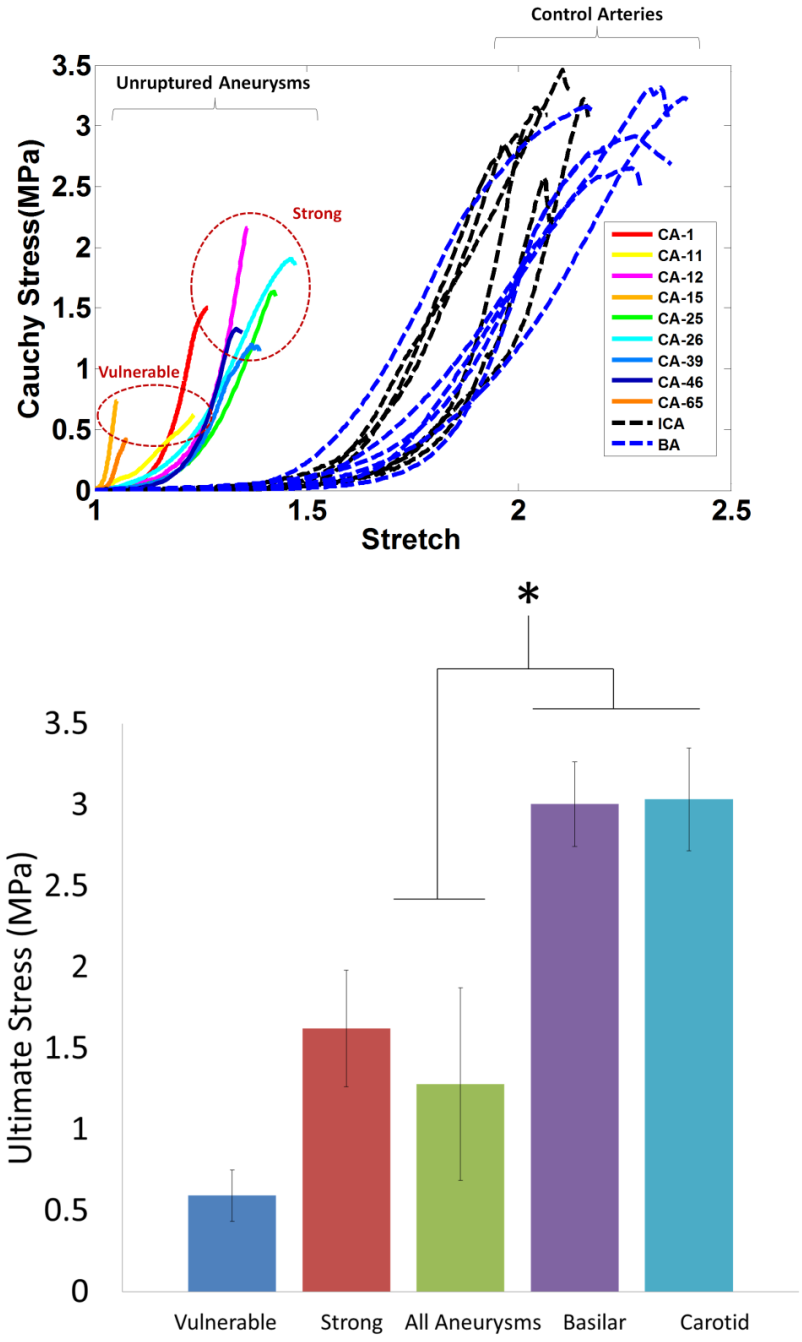

Figure 4. Results for the uniaxial loading tests for nine human aneurysm samples (unruptured) and twelve human control (basilar and internal carotid) arteries. All tissues were tested to failure. In (a) the stress (Cauchy) vs. stretch is shown. The loading curves for the more vulnerable aneurysm samples (n=3) are qualitatively different from the stronger samples (n=6). All aneurysm samples are weaker than the control arteries and displayed a greatly shortened toe region. In (b) the average failure stress (Cauchy) and standard deviation are shown for aneurysms and control arteries.

measure of the ability of the wall to withstand loading. For example, while the failure stress of CA-25 and CA-26 are quite similar, the thickness of CA-26 is nearly twice that of CA-25, resulting in a much larger ability to bear load. Namely, sample CA-26 has a failure tension of 580 kg/s^2, compared with 275 kg/s^2 for CA-25. This increased failure tension is necessary, given the increased intramural loading in CA-25 due to its larger equivalent diameter, Table 3. Following prior work [33] [47], we use a simple equilibrium equation for spherical membranes loaded under uniform pressure (Laplace's Law) and estimate the transmural pressure under which each aneurysm would fail ΔP_f ,

$$\Delta P_f = 4\sigma_f \frac{t_0}{D}\left(\frac{D}{d}\right)^3 \tag{2}$$

where σ_f is the ultimate Cauchy stress, D is the effective (unloaded diameter), t_0 is the wall thickness (unloaded) and d is the effective loaded diameter. Detailed derivation of equation 2 is shown in Appendix A. If we conservatively estimate the failure radius as 1.05 times the unloaded radius, then domes of CA-11 and CA-15 would fail with ΔP_f of 454 mmHg, 264 mmHg, respectively, whereas the estimated failure pressures of the higher strength domes range from 945 mmHg to 3300 mmHg. During weight training, arterial pressures can rise well above 200 mmHg [35]. If we consider 180 mmHg as a design load, then the factor of safety for CA-15 and CA-11 are 1.5 and 2.5, respectively, whereas the values for the stronger group range from 5.25 to 18.4. Motivated by the reported pressures during weight training [35], we might select a design load of 300 mmHg. In this case, the factor of safety would drop to 1.5 for CA-11 and CA-15 would fail.

2.4.5 Wall structure

The passive load bearing components in healthy arteries are elastin and collagen, (e.g. [48]). In cerebral vessels, the elastin is nearly confined to the internal elastic lamina, shown in green in Figure 5(a). Medial collagen fibers are wavy in the unloaded vessel, Figure 5(b). The adventitial collagen fibers display a larger range of fiber angles and fiber diameters than the medial collagen fibers, Figure 5(c). In contrast, no elastin is visible in the MPM images of the aneurysm wall (not shown), consistent with prior reports of the aneurysm wall [49, 50]. When viewed from the luminal side, there is a great variability in the fiber architecture and diameter between aneurysm samples, Figure 5. In some samples, the collagen fibers are densely packed, for example CA-12 in Figure 5 and CA-26 in Figure 6(a). In others, there is an abnormal sparse structure, for example CA-21. When viewed in a cross-sectional slice under MPM, the densely packed fibers of CA-26 can be seen to form a layered collagen structure, Figure 6(b).

The average wall thickness for sample CA-26 is 0.45 mm, substantially thicker than the average of 0.277 mm found for basilar arteries, Table 2. The average diameter of the collagen fibers on the luminal side is 0.99 μm and is statistically different from the average of 1.325 μm in the media of the basilar artery ($p=0.001$), suggesting a change in the fiber maintenance and/or creation process, Figure 7. In contrast, the average diameter of the collagen fibers from the abluminal side of the aneurysm wall is not statistically different from that of the basilar arteries ($p= 0.42$).

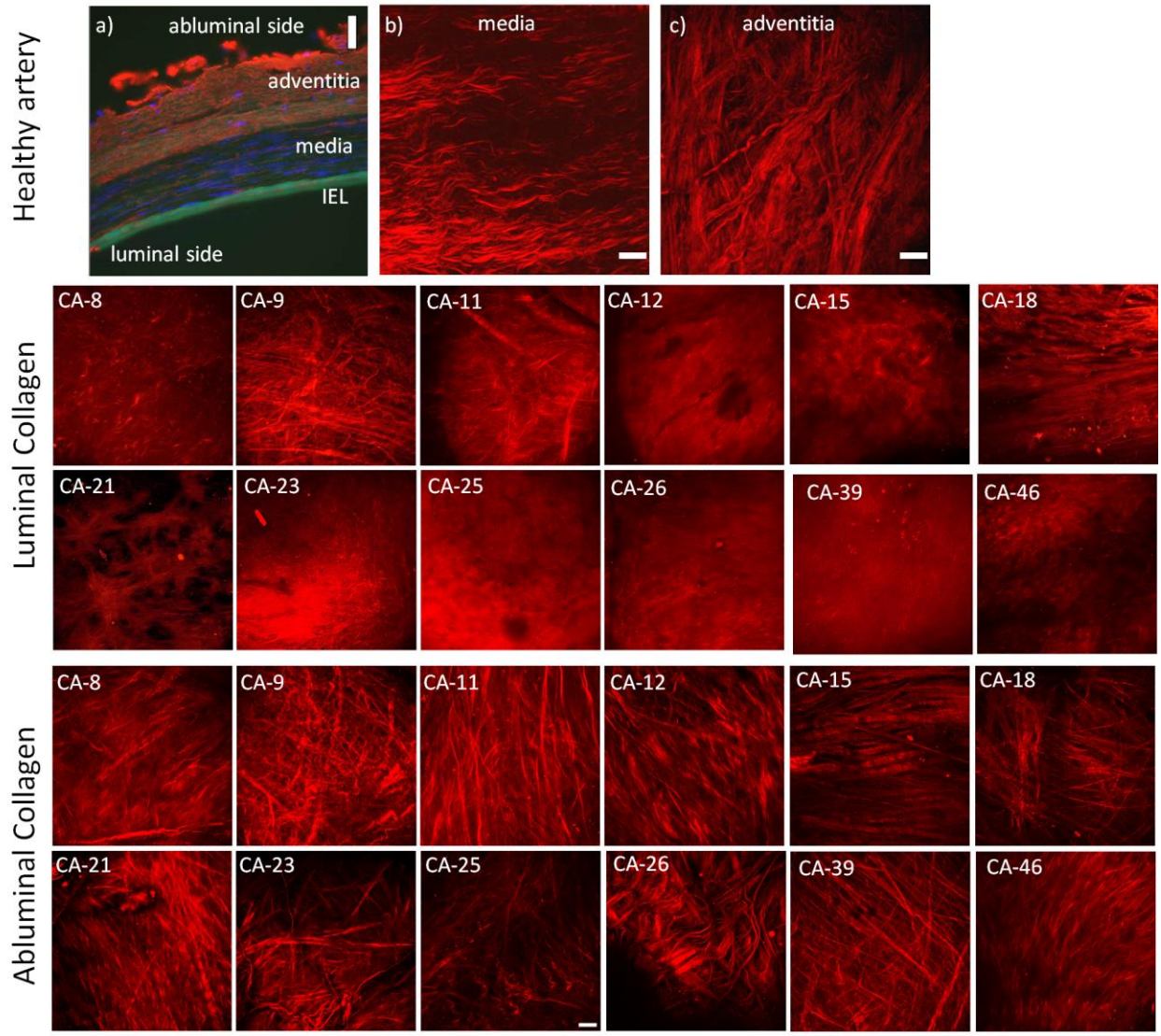

Figure 5. Images of the aneurysm and basilar wall structure. In (a) fluorescence microscopy image of cross sectional preparation of the human left vertebral artery (cerebral) fixed at 30% stretch. The immunohistochemical staining of the arterial wall reveals elastin (green) localized in the internal elastic lamina, cell nuclei (blue, DAPI stain), collagen fibers (red). Figs. (b) and (c) display collagen fibers in projected stacks of multiphoton images of the media and adventitia, respectively, for a basilar control artery. Projected stacks of multiphoton images for collagen fibers seen in the luminal and abluminal sides of the aneurysm are shown in (d) and (e), respectively. Substantial variability in the collagen fiber architecture can be seen in the luminal images. Scale bars in all figures are 50μm. (Fig. 5(a) is obtained and modified from [46], with permission from Springer)

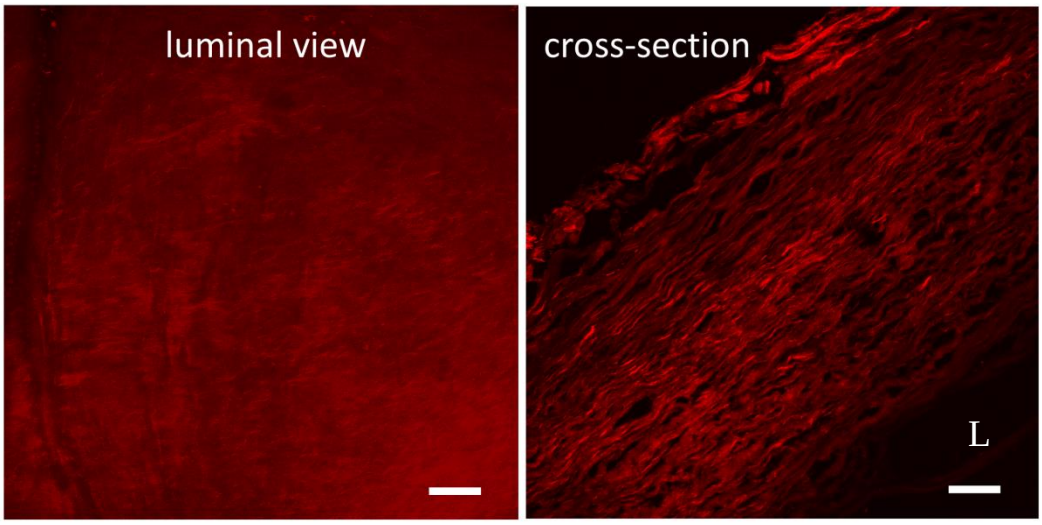

Figure 6. Luminal view (a) from sample CA-26 displaying an abnormally dense collagen signal relative to that from the control artery. A cross sectional view of this sample (b), showing increased layering of collagen fibers and increased wall thickness relative to control arteries shown in Fig. 5(a). Scale bars in all figures are 50μm. "L" denotes the lumenal side of the vessel.

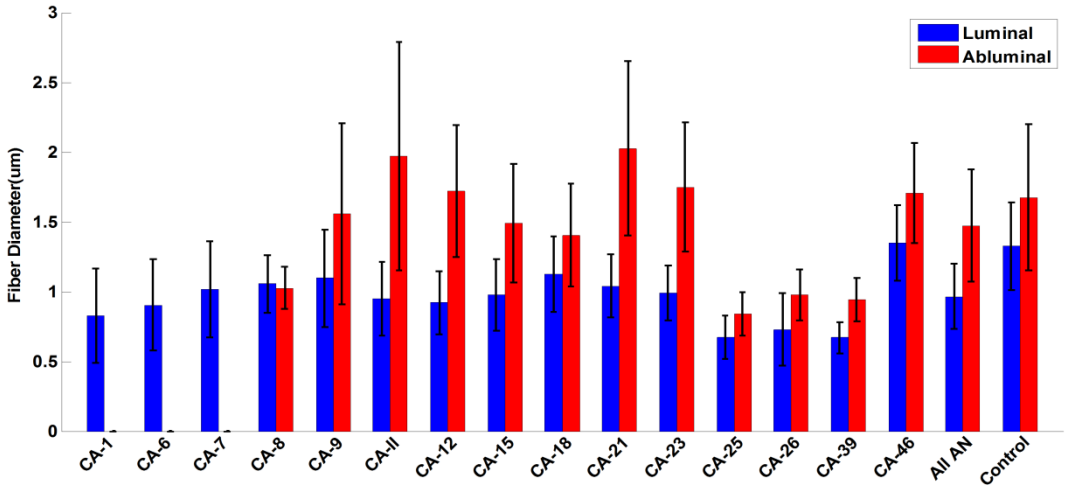

Figure 7. Results for collagen fiber diameter obtained for projected stacks from cerebral aneurysm and cerebral artery tissue. The bars shown average fiber diameter for a single location along with standard deviation denoted.

2.4.6 Recruitment of abluminal collagen

In order to better understand the role of adventitial collagen during loading, collagen fibers were imaged from the abluminal side of a representative sample during uniaxial loading with the UA-MPM system, Fig. 6. In the unloaded tissue, the abluminal collagen architecture was relatively disorganized with a wide range of fiber orientations. With increasing loads, fibers can be seen to be recruited to load bearing via two mechanisms- fiber straightening and fiber reorientation, consistent with recruitment mechanisms in healthy control arteries [45]. The fibers are nearly aligned by a stretch of 1.3, in line with the marked increase stiffness. At stretches lower than 1.2, the wall is approximately 30 times more compliant than the response in the high strain region.

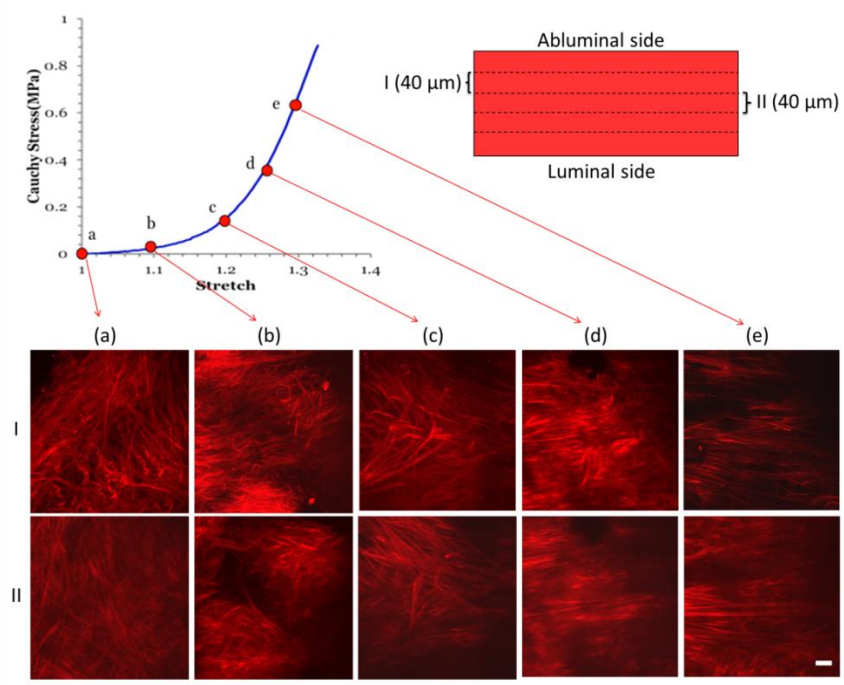

Figure 8. Recruitment of collagen fibers during uniaxial loading of a single sample obtained using the UA-MPM system for CA-25 at stretches of (a) 1.0 (b) 1.1 (c) 1.2 (d) 1.26 (e) 1.3 and are formed from a projection of stacks over an approximately 40um width of tissue. The images I and II are obtained at a depth of approximately 40um and 80um relative to the abluminal surface. Scale bars in all figures are 50µm.

2.5 DISCUSSION

In this work, we have demonstrated that even the unruptured population of cerebral aneurysms displays a diversity of mechanical properties and collagen architecture. Moreover, the current results suggest the existence of distinct sub-populations in the group of unruptured aneurysms: 1) more fragile aneurysms with failure properties similar to those of ruptured aneurysms, and 2) those well suited for load bearing under physiological conditions. The first group can be considered more vulnerable in that the estimated pressure loading for failure was closer to physiological attainable levels with a safety factor for loading to 180 mmHg of 1.5 and 2.5. In contrast, the second group could be considered robust at the time of harvest. Even though they were found to be statistically weaker than cerebral arteries, they were strong relative to expected physiological loads with safety factors of 5.26 and higher.

The possibility that rupture of a vulnerable aneurysm can be triggered by mechanical loads is supported by the fact that aneurysm rupture is often associated with strenuous physical activity including weight training [51, 52]. For example, in a study population of 445 patients, 42.8% of the ruptures aneurysms were associated with physical or emotional stress (e.g. [52]). This possibility is also consistent with the similarity between the failure strength of the weaker group and reported strength of ruptured aneurysms.

A large spread in mechanical strength of two unruptured aneurysms was also reported by Scott et al. [32]. Interestingly, the failure pressure of the weaker aneurysm (325 mmHg) lies between that of CA-11 and CA-15 in the weaker group in our study. The average values for the peak systolic and diastolic pressure were reported to be 320/250 mmHg during weight training, suggesting the weaker aneurysm was vulnerable to rupture under some conditions [32].

Though the failure stresses for the walls of the vulnerable group in our study were similar, the loading curves were qualitatively different, suggesting different pathologies. The high strength aneurysms displayed a greater uniformity in mechanical response with smaller variation of failure stresses, high strain stiffness and toe region. Sample CA-11 was resected from the only diabetic patient. This patient was asymptomatic and the aneurysm walls were of normal thickness, relative to the control arteries. The loading curve for this sample was qualitatively different from all others with a relatively poor fit to the exponential constitutive model. In contrast, sample CA-15 had one of the thinnest walls and a greatly shortened toe region relative to the other samples. Further, the abluminal collagen fibers of CA-15 demonstrated a morphology that was markedly different from all other samples.

A healthy cerebral artery is composed of three distinct wall layers. Moving from the lumen to the abluminal side, these layers are the intima which is separated from the medial layer by an internal elastic lamina (IEL), followed by the adventitia, Fig. 3(a). Collagen fiber diameters, measured from MPM images of the control arteries demonstrated a statistical difference in the collagen fiber diameter in the adventitial and medial layers with larger fiber diameters being located in the adventitial layer, consistent with the differences in collagen types found in these layers. For example, collagen I fibers are nearly entirely confined to the adventitial layer of cerebral arteries, with small amounts in the basement membrane of the endothelial cells [49]. In contrast, collagen type III is distributed across the wall. With the exception of one sample (CA-9), distinct collagen diameters were also identified from the luminal and abluminal views of the aneurysm tissue. In all other samples, the collagen layer on the luminal side was significantly different between aneurysm and control, suggesting the normal turnover of collagen fibers on the luminal (media orientating) side is substantially impacted

relative to the control artery. This is consistent with the large range of abnormal collagen architecture seen in this layer. In contrast, the diameter of the abluminal collagen fibers were similar to those found in the adventitia of the control arteries, suggesting an adventitial origin of this tissue. The findings for collagen fiber diameter in CA-9 appear to be of entirely adventitial type and suggest a different mechanism of remodeling. Differences in load bearing capacity in the medial layer across samples is certainly a contributing factor for the diversity in the adventitial remodeling and warrants further investigation (e.g. [53]).

Consistent with other reports, there was no IEL seen in any of the aneurysm samples. The loss of the IEL has structural implications as seen in the reduced toe region of the aneurysm tissue relative to the control cerebral arteries. The IEL also acts as a barrier or impediment to cellular movement and other transport between the endothelium and medial layers. Its absence is likely is a factor in this malfunction.

Recently, it has been reported that ruptured aneurysms have diminished stiffness relative to unruptured aneurysms, when separated by gender [54]. Further, it has been suggested that the larger deformations arising from the diminished wall stiffness could possibly be used to identify aneurysms at risk for rupture, when improved clinical imaging modalities become available [41]. This conjecture addresses the important issue of identifying a clinically accessible metric for identifying at risk aneurysms. The range of strains considered in those uniaxial loading studies was less than 15%, and corresponds to the magnified region in Figure 3. It can be seen that the two of the vulnerable aneurysms CA-11 and CA-15 in the current study had the highest low strain stiffness, in contrast to this earlier study. The present results suggest that aneurysms that are stiffer at low strain are not stronger. In fact, the more robust aneurysm walls displayed values of low strain stiffness that were closer to control arteries wall. Namely both were softer at low

loads than the vulnerable aneurysms studied in this work. Further investigations are warranted on this subject.

Uniaxial loading was used to assess the failure properties of the cerebral aneurysm tissue. While uniaxial testing is commonly used for failure testing, it should be recognized that in vivo loading of cerebral aneurysm walls is closer to equibiaxial than uniaxial. As shown in Figure 8, under uniaxial loading, collagen fibers experienced large reorientation up until stretches of approximately 1.25. Under equibiaxial loading, reorientation of this kind would not be seen. Therefore, the low strain regions shown in Figure 3 provide information about the ability of the fibers to reorient and uncrimp rather than providing information about collagen load bearing relevant to physiological biaxial loading conditions. We caution against using material properties obtained from low strain, uniaxial loading to model biaxial aneurysm deformations. The aneurysm wall is an anisotropic material, and therefore, the anisotropic response cannot be determined from uniaxial experiments, in the absence of other information about the fiber structure. We emphasize that material properties were obtained in this work for a relatively simple phenomenological model for the purpose of characterizing the mechanical response. The use of a structurally motivated model that incorporates fiber recruitment and fiber orientation such as was introduced in Hill et al [45] is the subject of an ongoing investigation.

It should be noted that the control cerebral arteries used in this study were stored at -80°C prior to testing. Stemper et al. reported that the uniaxial mechanical properties, including high-strain stiffness and ultimate stresses of porcine aortas were not significantly different between fresh samples and those stored at -80°C for 3 months [55].

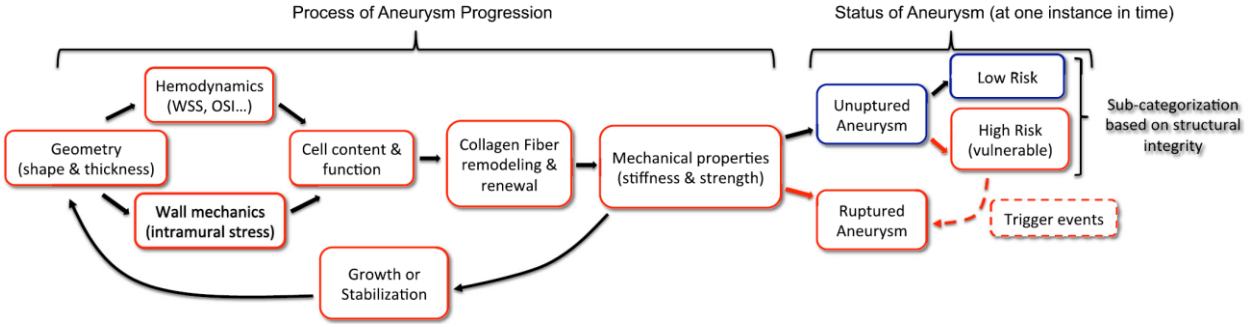

Figure 9. Schematic of the coupled factors driving aneurysm progression toward stabilization or growth, illustrating how the mechanical loading drives cellular response which in turn drives the collagen production/turnover process (either pathological or normal), that in turn determines the mechanical properties of the wall. These properties then determine the geometry of the aneurysm wall under the given loads. At a given point in time, the status of the aneurysm is either ruptured or unruptured. Using a structural integrity index, the unruptured aneurysms can be categorized as low risk (strong) or high risk (vulnerable). The high risk unruptured aneurysms have the potential to shift to the ruptured category given an appropriate trigger event such as rise in blood pressure. When the sub-categorization in unruptured status is available, correlations can be explored between wall structure and cell content and strong versus vulnerable/ruptured walls.

For a given hemodynamic waveform, the nature of the local mechanical loads on the aneurysm wall (both surface shear and intramural stresses) are largely a function of the geometry of the parent vasculature and aneurysm sac. Intramural loads that vary too greatly from physiological levels can negatively impact the cellular health. It is believed that some, as yet unidentified aspect, of the intra-saccular flow leads to a degeneration of the endothelium, that can in turn negatively influence the wall cellular content and ultimately interfere with the normal process of collagen renewal and maintenance (e.g, [56, 57, 58, 59]). Prior efforts to identify clinically useful methods for risk stratification have therefore focused on identifying correlations between rupture status and clinically accessible quantities such as sac geometry and intra-

saccular hemodynamics, Figure 9. Work is ongoing to identify a clinically useful metric that goes beyond the current use of aneurysm size. More recently, efforts have been made to correlate intramural cell content and rupture status [21]. Frösen and collaborators have clearly demonstrated the great variability in cell content in aneurysm walls. The intramural content of even an unruptured aneurysm was found to vary from an endothelialized wall with linearly organized smooth muscle cells (SMCs) to a hypocellular wall [21, 56].

The current findings complement these studies, demonstrating variability in collagen content and mechanical properties within even the unruptured population that is consisted with this range of intramural cell content. Namely, given the large range of cell content in unruptured walls, we would expect the collagen fabric that is maintained by these cells should also vary, as should the mechanical properties which are dependent on the collagen fabric.

To date, a definitive rupture index using hemodynamic, geometric or biological markers has not been identified [56, 60, 61, 30]. The existence of a sub-population of unruptured aneurysms with failure properties similar to those of ruptured aneurysms underlines the challenge in using rupture status as an endpoint to interpret data. Namely, if the objective is to predict whether an aneurysm is vulnerable to rupture, then categorizing a vulnerable unruptured aneurysm as safe can confound the interpretation of the data, since this aneurysm may soon rupture under suitable triggers. In cases where it is possible to obtain resected aneurysm tissue, we can overcome this limitation in classification by looking for correlations with an index of wall integrity rather than rupture status, Figure 9. Such an index would account for the combined effect of material properties (e.g. failure stress), geometry (e.g. wall thickness, shape and diameter) and expected loads through, for example, a factor of safety. While such an integrity index is not yet useful in the clinic, we believe it will be valuable for future studies of wall

biology and provide a more solid framework for understanding the mechanisms responsible for aneurysm wall degradation. Insights gained from studies using an index of wall integrity may enable more effective use of clinically available data such as aneurysm hemodynamics. Noninvasive method for estimations of wall strength and wall stress based on clinically available data in AAA [35, 42] could be useful for developing similar method in IA. Ultimately, an improved understanding of the mechanisms responsible for the progressive degeneration or stabilization of cerebral aneurysms will be useful for development of improved treatment strategies.

2.6 CONCLUSIONS

This work is the first to combine MPM imaging with mechanical testing for studying the pathology of human cerebral aneurysms. Using this approach, we found substantial variability in collagen architecture and mechanical response even within walls of unruptured aneurysms. This variability is consistent with earlier studies using classical histological approaches that found a large variability in mural content, even within unruptured human aneurysms domes [21].

The collagen architecture on the luminal side of the aneurysms was generally quite different from the healthy artery and showed a great variability between samples. Some samples displayed a dense fiber network, likely produced through remodeling mechanisms. Others had a sparse, inhomogeneous fiber architecture suggestive of impaired remodeling. Fibers from the luminal side were nearly always thinner compared with medial fibers in normal arteries. In contrast, the abluminal side was more similar to the adventitia of healthy arteries with respect to fiber diameter and orientation.

Even unruptured aneurysms displayed a wide range of mechanical behaviors. Two sub-categories were identified: i) vulnerable aneurysms with lower failure stress and lower estimated failure pressure, and ii) more robust aneurysms with higher failure stress and higher estimated failure pressure. Although the stronger aneurysm walls were weaker than control arteries, they were strong relative to estimated physiological loads with a safety factor of 5.2 and higher, suggesting an effective remodeling process. In contrast, the failure stress of the vulnerable aneurysms was similar to values reported for ruptured aneurysms and had factors of safety of 2.5 and less. Such a sub-categorization of unruptured aneurysms is therefore an important consideration when using rupture as an end-point of risk assessment studies.

This work suggests a structural integrity index will be useful for interpreting biological and hemodynamic data in future investigations of the mechanisms responsible for the progressive degeneration of the wall of intracranial aneurysms.

3.0 ESTIMATE OF STRUCTURAL INTEGRITY IN CEREBRAL ANEURYSMS: A CASE STUDY

3.1 INTRODUCTION

Rupture of intracranial aneurysms is the leading cause of subarachnoid hemorrhage, a devastating type of stroke with high mortality and disability rates. In order to better estimate the rupture risk of aneurysm, it is necessary to understand the pathophysiology of aneurysm. Figure 10 illustrates how the mechanical loading, including hemodynamics and wall biomechanics, are conjectured to influence the collagen production and remodeling, that in turn affects the mechanical properties of the wall. As discussed in Chapter 2, unruptured aneurysms can be categorized as robust or fragile, and our prior analysis suggests that the fragile aneurysms may rupture when a trigger event happens, for example, rise in blood pressure [62].

Since the intermediate steps in the pathology are poorly understood, efforts have been made to identify correlations between clinically obtainable factors such as geometric features [13, 19], patients characteristics [71], intrasaccular hemodynamics [23, 24], cellular content [21] and outcome, as shown in Figure 10. The current approach is generally binary (rupture/unrupture) and the larger variation within the unruptured aneurysms is not considered in this binary approach. To improve the risk estimation, a continuum ranking of the unruptured population or at least sub-classification would be more appropriate.

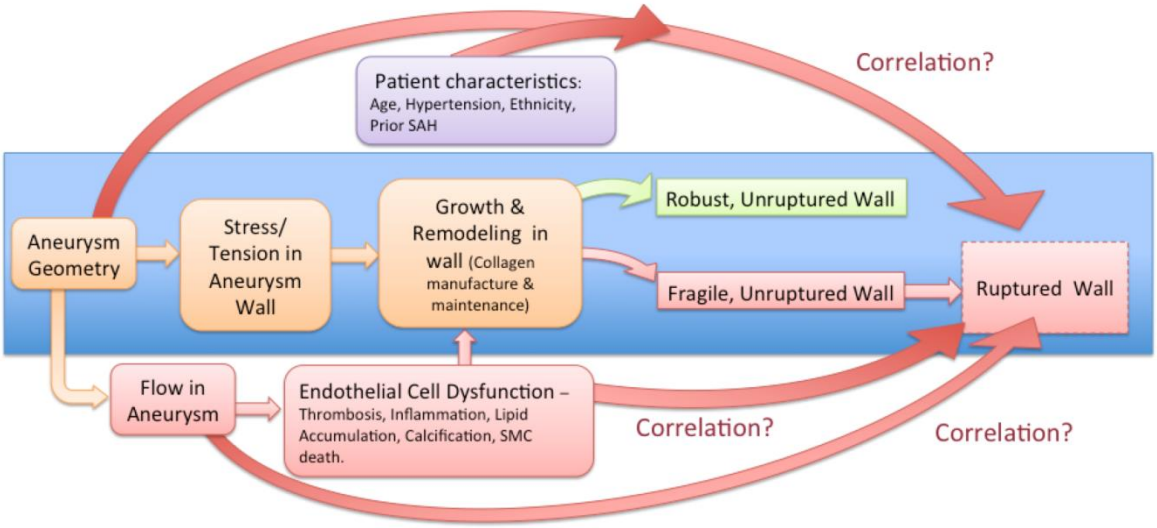

Figure 10. Diagram of the coupled factors governing aneurysm pathophysiology and their correlation with rupture risk

A metric is needed in order to rank the unruptured population. Like other mechanical entities, rupture of the aneurysm wall is a local failure that occurs when the local stress rises above the ability of the wall to bear loads (strength). This suggests that a ranking of the mechanical integrity of the aneurysm wall using Factor of Safety could be used to score the unruptured aneurysms.

The Factor of Safety is defined as

$$FoS \equiv \sigma_F / \sigma_{\max} \tag{3}$$

where σ_F is the ultimate stress of the material and $\sigma_{\max}$ is the maximum stress expected to be borne by the material. The FoS is a measure of how much stronger the system is than the design load. For resected aneurysm, the mechanical properties including mechanical strength was obtained by performing mechanical tests [62]. The design load is the maximum wall stress on the

aneurysm sac. We can estimate the stress, wall tension, and other quantities using the FEM method [41, 72].

In a previous work [62], we analyzed the mechanical properties for 8 unruptured human aneurysms. Laplace's Law for a sphere was used to estimate the intramural stress and assess the structural integrity of these aneurysms. Here, we build on this work and provide a more accurate estimate of the structural integrity using patient specific biomechanical models. We provide an in depth analysis of two robust, unruptured aneurysms (CA-25 and CA-26 from Chapter 1), evaluating their FOS based on stresses estimated from finite element studies of the mechanics using patient specific geometries and material properties. We assess their collagen architecture and cellular content to explore the capacity of at least some aneurysms to reduce intramural stresses through effective growth and remodeling. We utilize our UA-MPM system to image the collagen structure during uniaxial loading to better understand the role of abluminal collagen during loading. Immunohistochemistry staining of ECM and cellular content are performed to investigate the wall structure and similarity of functional roles to that of the control basilar artery. A third unruptured aneurysm (CA-09) from a young patient (27 years old) is also considered. The fiber distribution found in this wall was different from all other aneurysms studied in Chapter 2.

3.2 MATERIALS AND METHODS

3.2.1 Aneurysm harvest, mechanical testing

Aneurysm tissue harvest, transportation and handling followed the protocols described in section 2.3.1. Resected tissue was tested using the UA-MPM system to obtain the failure mechanical response and multiphoton images of collagen structure. The testing methods were introduced in section 2.3.4 for mechanical testing.

3.2.2 Multiphoton imaging and image post processing

Images of collagen fibers were obtained from MPM imaging (section 2.3.5), and imported into MATLAB (MATLAB R2012b, The MathWorks Inc., Natick, MA), in which a previously developed program was used to obtain collagen fiber orientation [45]. In this program, orientation histograms were computed based on an edge detection algorithm. The dominant direction in predefined sub-regions (12 pixel × 12 pixel) of MPM image was computed from maximum pixel intensity gradient, and values of gradient measure associated with the dominate direction of each sub-region were accumulated in directional bins [-90°, 90°) to form an orientation distribution histogram [45]. The histogram was normalized to the maximum magnitude in all directions. This procedure was performed for all MPM images in a z-stack, and a contour plot was generated to show the orientation distribution along the thickness direction (Appendix C).

3.2.3 Immunofluorescent staining

Specimens were dissected from aneurysm samples and basilar arteries, and then fixed under unloaded condition in 2% paraformaldehyde for 2h. Cross sections were obtained by freezing the specimen in liquid nitrogen and 8 um thick slices were cut using a cryostat (HM 505E, Microm). Sections were stained with antibodies against collagen type I, collagen type III and alpha smooth muscle actin (αSMA). Immunofluorescent staining was performed following the protocol provided by Center for Biological Imaging (CBI) at University of Pittsburgh. Sections were permeabilized with 0.1% Triton X-100 in PBS for 10 min, and then blocked in 2% BSA for 45 min. Subsequently, sections were incubated with the primary antibody of collagen type I (ab34710, Abcam), collagen type III (ab7778, Abcam) or αSMA (ab7817, Abcam) for 60 min, washed 5 times with PBB, incubated with fluorescent secondary antibody (Cy3, CBI) for 60 min. DAPI was added to stain nuclei and cover slip was adhered for imaging. Detailed protocol and antibody information are presented in Appendix B. All sections were imaged using Olympus Fluoview 1000 confocal microscopy (Olympus Imaging America, Melville, NY).

3.2.4 Image quantification

Image analysis was used to determine the thickness fraction of positive αSMA, collagen type I and collagen type III in the wall, as well as nuclei count per wall area. To quantify the thickness fractions of αSMA, collagen I and collagen III, a custom image analysis program was developed in Matlab to identify the wall thickness, αSMA, collagen I and collagen III layer thickness. The RGB image was enhanced and thresholded to a binary image to define the wall boundary using an edge detection algorithm (bwboundaries function in Matlab). Similarly, the red channel

images (αSMA, collagen I and collagen III labeled with Cy3) was used to identified the boundary of αSMA, collagen I and collagen III layers. The shortest distance from a point on the luminal boundary to any point on the abluminal boundary was defined as wall thickness. Wall thickness was measured at 20 locations on the image and averaged. The normalized thickness was defined as the thickness of positive fluorescence layer divided by the total wall thickness. Cell nuclei counts were determined by identifying objects according to size and intensity threshold on the blue channel (DAPI). Cell density was calculated as cell count divided by the wall area, which is the area between the wall boundaries.

3.2.5 Factor of safety analysis

Factor of safety (FOS), defined in Equation 3 was used to estimate the structural integrity of cerebral aneurysms. In particular, the structural integrity is defined as failure stress obtained from mechanical testing, divided by the design load, which is the maximum von Mises on the aneurysm dome estimated using the finite element modeling with patient-specific mechanical properties and geometry (Section 3.2.8). Based on the reported pressures during weight training and physiological stress [35,36], we selected 300 mmHg as the maximum transmural pressure drop. The stress distribution of the aneurysm wall under physiological pressure (100 mmHg) and maximum pressure (300 mmHg) was estimated using the finite element method as described in Section 3.2.8.

3.2.6 Patient-specific material properties

For biomechanical modeling, the aneurysm wall was idealized as an isotropic, incompressible hyperplastic material [73],

$$W = \frac{C_1}{2C_2}(e^{C_2(I_1-3)} - 1) \tag{4}$$

where C_1 and C_2 are two material parameters, and I_1=tr$\underline{B}$, where I_1 is the first invariant of the Left Cauchy Green tensor $\underline{B}$. The Cauchy stress tensor for an isotropic incompressible hyperplastic material is,

$$\underline{T} = -p\underline{I} + 2\frac{\partial W}{\partial I_1}\underline{B} - 2\frac{\partial W}{\partial I_2}\underline{B}^{-1} \tag{5}$$

where I_2 is the second invariant of $\underline{B}$. Plug (4) into (5) and the Cauchy stress tensor becomes,

$$\underline{T} = -p\underline{I} + C_1 e^{C_2(I_1-3)}\underline{B} \tag{6}$$

For uniaxial testing, we assume T_{22}=T_{33}=0, and $\lambda_2 = \lambda_3 = 1/\sqrt{\lambda_1}$, thus the first principle stress is,

$$T_{11} = C_1 e^{C_2(\lambda_1 + 2/\lambda_1 - 3)}(\lambda_1^2 - 1/\lambda_1) \tag{7}$$

Uniaxial mechanical testing data [62] were fitted to (7) to obtain the patient specific material parameters C1 and C2, as listed in Table 4.

Table 4. Aneurysm wall morphology and material properties used in modeling

Case	*Wall Thickness t_0 (mm)*	*Equiv. Diam. (mm)*	*K_{11} (N/mm)*	*C_1 (MPa)*	*C_2*	*R^2*
CA-25	0.24	4.5	0.067	0.114	4.38	0.99
CA-26	0.45	6.8	0.176	0.303	1.71	0.96

3.2.7 Governing equations

The balance of linear momentum is satisfied if the first equation of motion

$$\nabla \cdot \underline{T} + \rho \underline{b} = \rho \underline{a} \tag{8}$$

is satisfied at every material point in a body at all times during its motion. $\underline{b}$ is the specific body force field, $\underline{a}$ is the material acceleration field, and ρ is the current mass density field in equation (8). For static equilibrium in the absence of body forces, equation (8) becomes,

$$\nabla \cdot \underline{T} = 0 \tag{9}$$

3.2.8 Finite element modeling

The lumen surfaces were obtained from pre-surgical 3D rotational angiography images. The wall thickness was prescribed as a constant, obtained from patient specific measurements [62]. Shell elements were used for the wall, motivated by the small ratio of thickness to equivalent diameter in the aneurysm domes, Table 4. Maximum mesh size was 0.2 mm (Mesh sensitivity study in Appendix D). Transverse shear stiffness needs to be specified for shell element modeling, and it was estimated using the following method introduced by Ma et al. [74],

$$K_{11} = K_{22} = \frac{5}{6} G t_0 = \frac{5}{18} E t_0, \quad K_{12} = 0 \tag{10}$$

where K_{11}, K_{22}, and K_{12} are transverse shear stiffness in the local 11, 22, and 12 directions of the shell element, t_0 is the shell thickness. In this study, E is defined as the Young's modulus at transition strain (assumed within the physiological regime) [1], which was estimated by

$$E = \sigma_{11} / \varepsilon_{11} \tag{11}$$

where σ_{11} and ε_{11} are the first principle stress and strain respectively, whose directions are coincided with loading direction in uniaxial mechanical testing. Transverse shear stiffness was listed in Table 4. Zero displacement boundary conditions were applied at the ends of parent vessels, as shown in Figure 11. ABAQUS/Standard 6.12 was used to perform the finite element analysis at equilibrium.

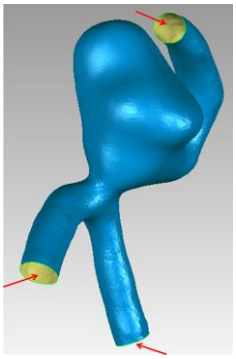

Figure 11. Zero displacement boundary conditions applied at the ends of parent vessels. Red arrows show the locations of zero displacement boundary condition. Because of the lack of sensitivity on the stress results (Appendix D), the parent vasculature was not included in the final simulations.

3.3 RESULTS

3.3.1 Factor of safety

The von Mises stress distribution for loading to 100 mmHg in CA-25 is relatively homogeneous, ranging from 38 KPa to 94 KPa while that in CA-26 ranges from 12 KPa to 160 KPa, Figure 12. Estimates using Laplace's Law predicted intramural stresses in CA-25 and CA-26 of 72 KPa and 58 KPa, respectively, consistent with the range found here. The larger heterogeneity in CA-26 arises from its more complex shape.

A FoS was calculated using measured ultimate stress and maximum von Mises stress on the aneurysm dome for loading to 300 mmHg. The von Mises stress distribution of both CA-25 and CA-26 are shown in Figure 13.The maximum von Mises stress on the dome of aneurysm CA- 25 and CA-26 are 0.32 MPa and 0.40 MPa respectively, shown in Table 5. The FoS for both CA-25 and CA-26 are 5.1 and 4.8, respectively for even this extreme loading condition, suggesting effective remodeling in both cases. The control artery was idealized as a perfect cylinder and the FoS estimated based on Laplace's law is 12.5.

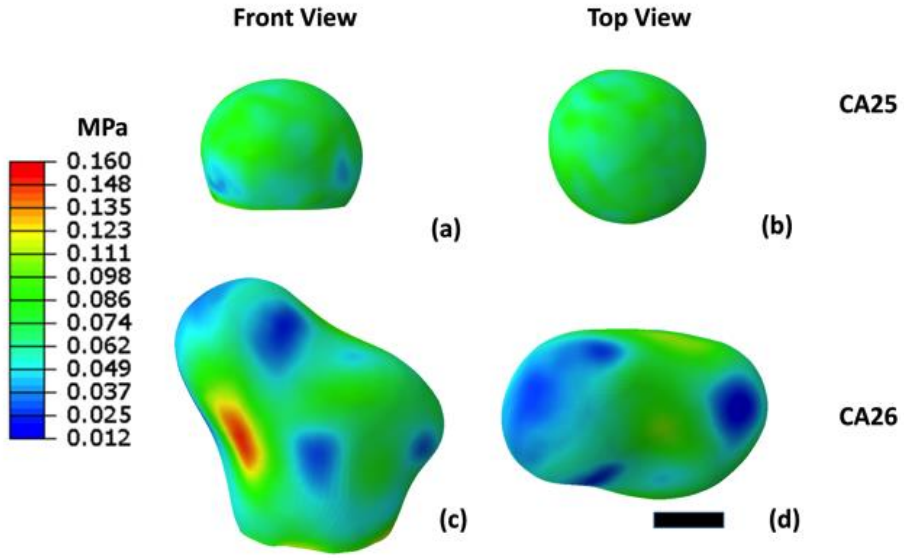

Figure 12. Contours of von Mises stress in patient specific aneurysm models at 100 mmHg. Scale bar = 2 mm.

Table 5. Maximum stress on the dome and Factor of Safety.

(Failure stress was measured by uniaxial mechanical test of resected aneurysm samples to failure)

Case	*Max von Mises Stress (MPa)*	*Failure Stress (MPa)*	*FoS*
CA-25	0.32	1.63	5.1
CA-26	0.40	1.90	4.8
Control	0.24	3.01	12.5

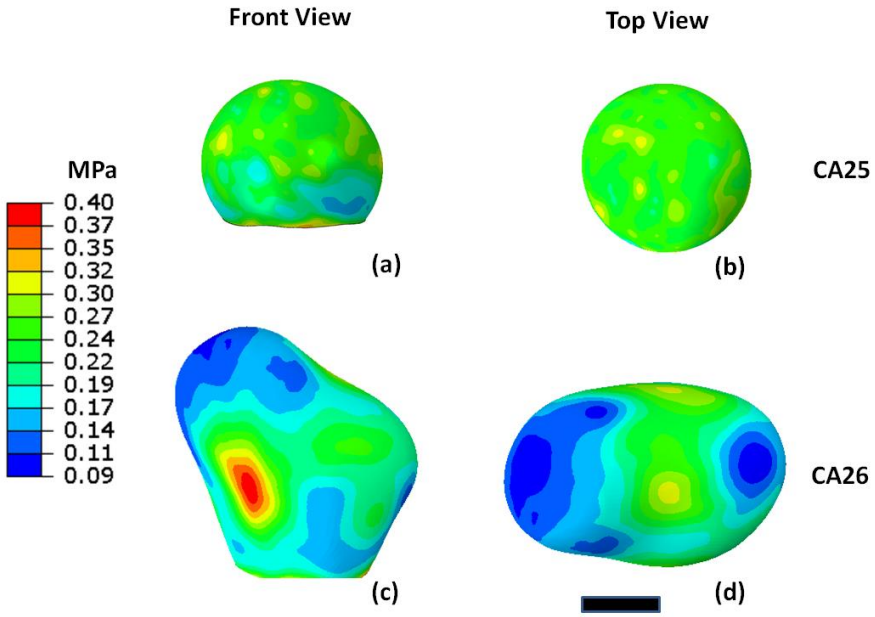

Figure 13. Contours of von Mises stress in patient specific aneurysm models at 300 mmHg. Scale bar = 2 mm.

3.3.2 Parameter sensitivity study

Effect of transverse shear stiffness on von Mises stress on the dome of aneurysm was studied. Transverse shear stiffness K_0 decreasing to 0.1 K_0 alters the maximum stress by 21 KPa in CA-25 and 39 KPa CA-26, respectively, and those are only 2% and 2.5% changes with respect to failure stress. As shown in Table 6, the maximum stress increases with the transverse shear stiffness, while the minimum stress decreases with the transverse shear stiffness.

3.3.3 Extracellular matrix

The passive load bearing ECM components are elastin and collagen in healthy arteries. The internal elastic lamina, media and adventitia of the cerebral artery are shown in Figure 14. Elastin which is the green layer in the cross section view of the basilar artery is almost restricted

to the internal elastic lamina. The medial collagen fibers of the basilar artery are wavy at the unloaded state, while the adventitial collagen fibers exhibit a wider range of fiber orientation and fiber diameters. The luminal, abluminal and cross section MPM images of CA-09, CA-25, CA-26 and control artery are shown in Figure 15. No elastin was observed in the MPM images of any of the aneurysms. The average diameter of the collagen fibers on the luminal side is 0.99 um and is statistically smaller than the average of 1.325 um in the media of control artery. In contrast, the average dimeter of ablumial collagen is not significantly different from that of control artery (p=0.42) [62].

Table 6. Effect of transverse shear stiffness on Von Mises stress on the aneurysm dome

CA-25, P=100mmHg		*Max. Stress (KPa)*	$\frac{Max.Stress\ at\ P}{Failure\ Stress}$	*Min. Stress (KPa)*
K_0	$K_{0=}K_{11}=K_{22}=0.067$	94	5.8%	38
10 K_0	$K_{11}=K_{22}=0.67$	99	6.1%	34
0.1 K_0	$K_{11}=K_{22}=0.0067$	78	4.1%	56
CA-26, P=100mmHg				
K_0	$K_{11}=K_{22}=0.176$	156	9.6%	12
10 K_0	$K_{11}=K_{22}=1.76$	161	9.9%	7.7
0.1 K_0	$K_{11}=K_{22}=0.0176$	120	7.4%	21

In order to better understand the wall structure of the aneurysm wall, immunofluorescent staining of collagen type I, collagen type III, αSMA on cross sections of aneurysms and control arteries were imaged under confocal microscopy, Figure 16. In the wall of the cerebral artery, collagen type I is mostly confined to the adventitia and collagen type III is distributed across the wall. CA-25 and CA-26 display a similar layered collagen structure to that of the control artery,

with collagen I on the abluminal side and collagen III distributed across the wall. In contrast, collagen type I is shown across the entire aneurysm wall for CA-09, which is consistent with the adventitial type collagen seen in both luminal and abluminal sides on MPM images, shown in Figure 15. Collagen III in CA-09 is also seen across the wall, similar to the other two aneurysms and the control artery. The existence of a band of collagen I on the abluminal side in all of three aneurysms as well as in the control artery is consistent with a study of four aneurysms imaged using polarized light microscopy [75]. Quantitatively, the average normalized collagen I layer thickness are 1 ± 0.01 for CA-09, 0.14 ± 0.03 for CA-25, 0.17 ± 0.01 for CA-26 and 0.22 ± 0.02 for control artery. Compared to the control artery, CA-25 and CA-26 have significantly thinner collagen I layers ($p=0.011$ and $p=0.01$), while CA-09 has a significantly thicker collagen I layer ($p=0.0001$). In summary, the existence of two layers in CA-25 and CA-26, is similar to that of the basilar artery. However, CA-09 displays a qualitatively different remodeled wall. It may be important that this aneurysm came from the only young patient in our study (27 years old). The two layered wall found in CA-25 and CA-26 is consistent with the existence of luminal and abluminal layers in aneurysms found by Mimata et al. [76].

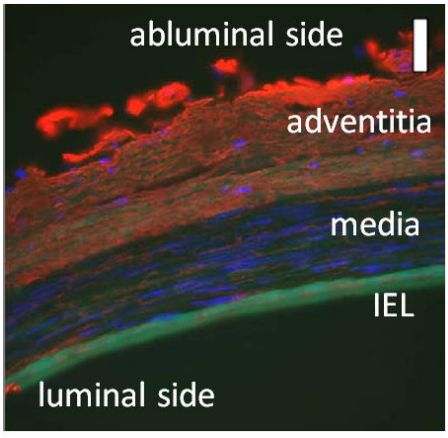

Figure 14. Fluorescence microscopy images of immuno-stained cross sectional preparations of the human left cerebral vertebral artery, fixed at 30% stretch. Bar = 50 um (Reproduced from Figure 5 (a)).

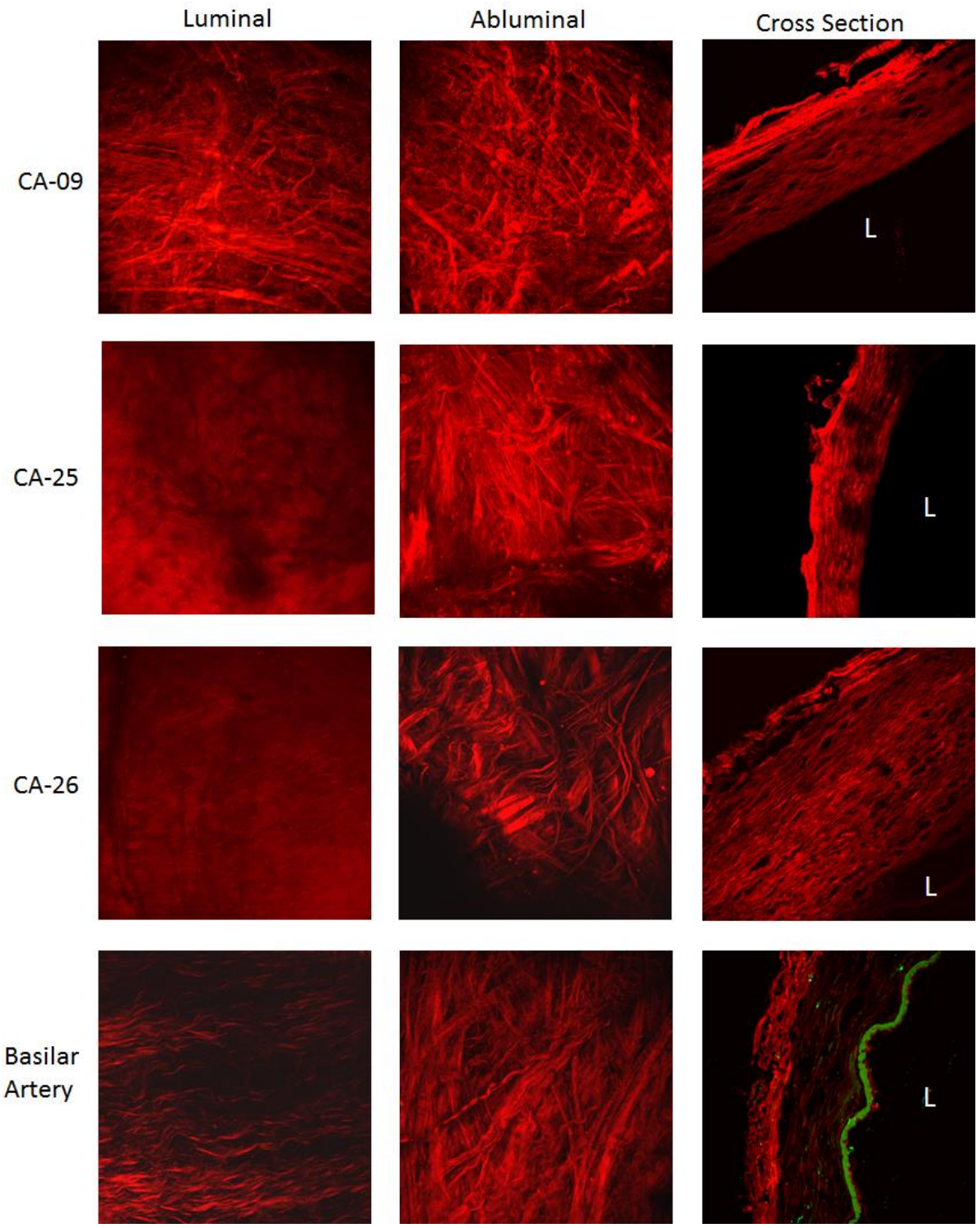

Figure 15. Luminal, abluminal and cross section (left, middle and right column) MPM images of CA-09, CA-25, CA-26 and control artery at unloaded state. Collagen in red and elastin in green.

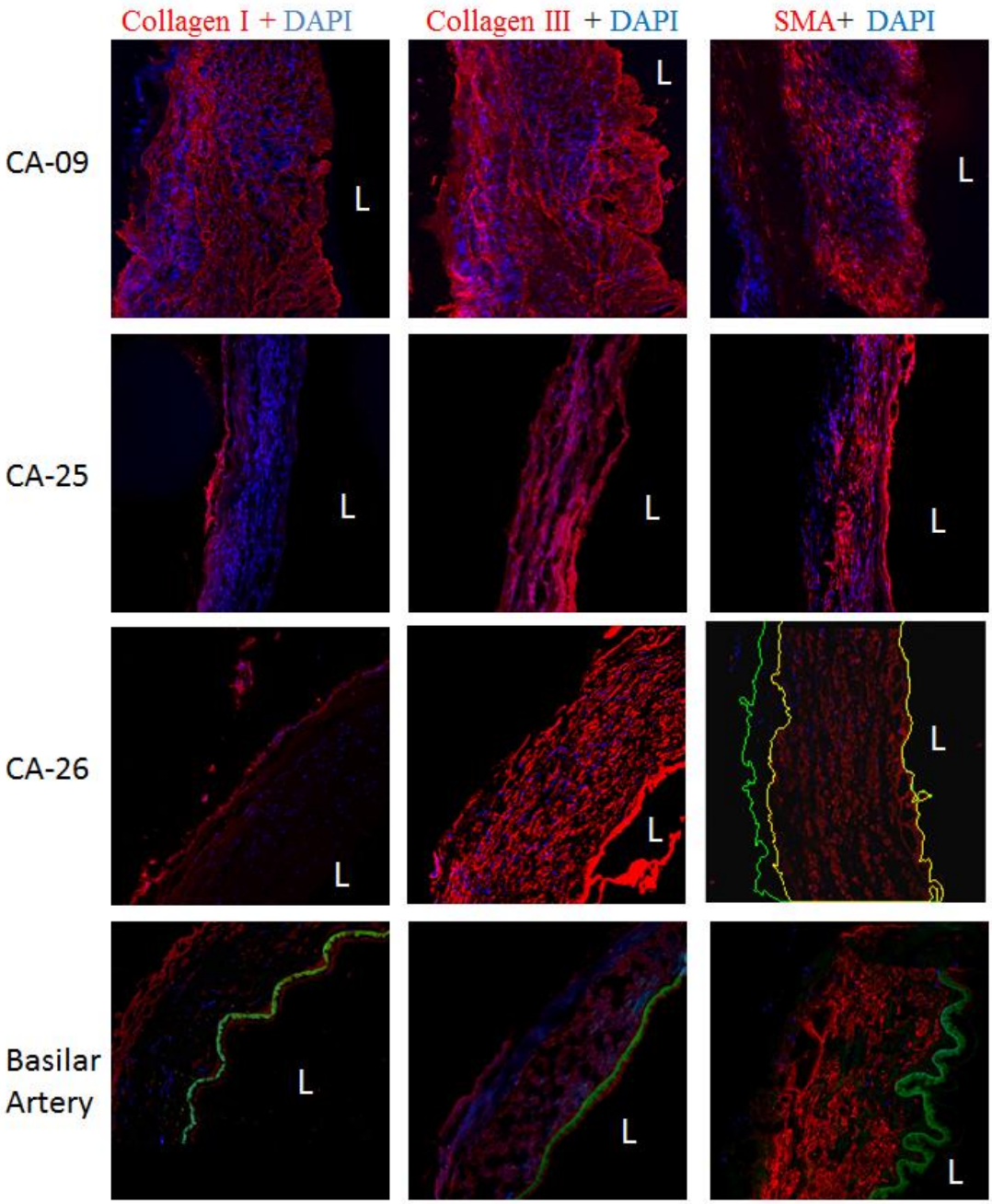

Figure 16. Immunofluorescent staining of collagen type I, collagen type III and αSMA (left, middle, and right column) on cross sections of CA-09, CA-25, CA-26 and basilar artery. Collagen type I, collagen type III and αSMA in red, elastin in green and DAPI in blue. SMA+DAPI image for CA-26 was used to illustrate the automated layer thickness identification. The boundary of αSMA layer was highlighted in yellow, and the abluminal surface was highlighted in green. L denotes the lumenal side of the vessel.

3.3.4 Three dimensional fiber orientation

In this section, we consider how the fiber orientation changes through the aneurysm wall. This is in contrast to the prior section where we considered projected images. The fiber orientation distribution exhibits two main directions inside the wall and is dispersed on the abluminal side in CA-25. As shown in Figure 17, collagen fibers in CA-25 are aligned at single direction of -50° at depth from 64 to 100 um, while the main fiber direction transits from -50° to +50° between 64 to 44 um. The fiber orientation becomes dispersed at abluminal side (0 ~ 44 um), arising from wavy fibers in more evenly distributed directions. Collagen fibers in CA-09 have two main directions around ±25° through the thickness. In CA-26, collagen fibers are almost aligned a single direction around 50° inside the wall, and similar to CA-25, the fiber orientation is dispersed on the luminal side. Layered collagen with different orientations suggests that the wall has remodeled with an ability to bear biaxial loads. This is consistent with an earlier study, in which layered collagen structure with different orientation in adjacent collagen layers was found [75]. In this previous study, aneurysm tissue was fixed, sectioned and imaged with polarized light microscopy, while our method enables investigating the collagen structure of fresh tissue nondestructively. As noted in the next section, this enables imaging of the collagen fibers under load.

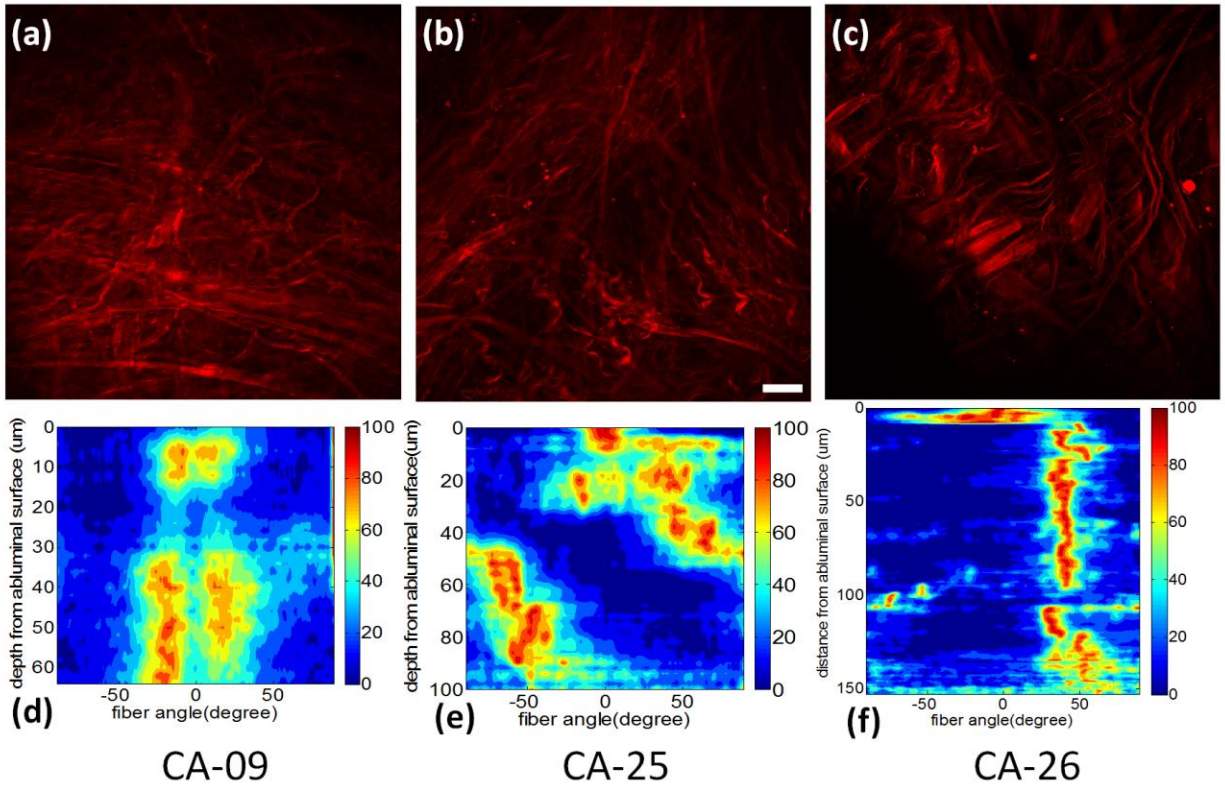

Figure 17. Collagen structure in CA-09, CA-25, CA-26 shown in columns one, two three, respectively. Where (a), (b), (c) show projected MPM stacks viewed from the abluminal side and (d), (e), (f) show histograms of fiber orientation as a function of depth from the abluminal surface. The histogram at each depth was normalized to the maximum magnitudes in all directions. The maximum magnitude is shown as 100 on the color scale of the contour plots.

3.3.5 Recruitment of abluminal collagen

In this section, we discuss results on collagen recruitment during uniaxial loading as imaged in a single sample under increasing load. Abluminal collagen was imaged during uniaxial loading with the UA-MPM system, and the fiber orientation through the thickness is presented in contour plots, Figure 18. Fiber orientations displayed a wide range at the unloaded state. As expected, as the stretch increases, fibers reoriented towards the loading direction. At a stretch of 1.26 and

higher, the fibers are highly aligned in the loading direction, demonstrating the recruitment of abluminal collagen. This is consistent with the steepening of the loading curve at this level of stretch.

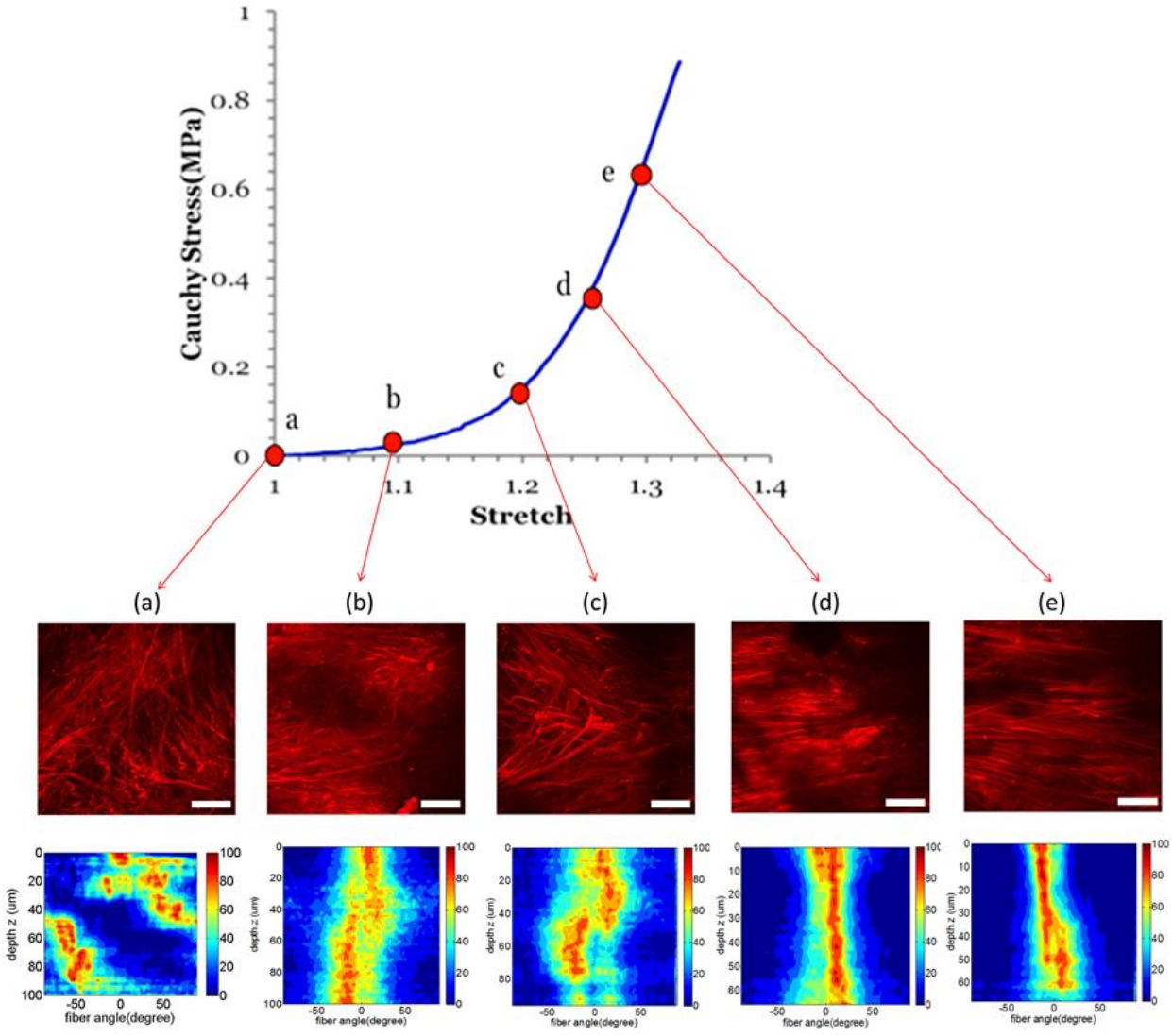

Figure 18. Recruitment of collagen fibers within approximately 100 microns of tissue from the abluinal side during uniaxial loading of CA-25 obtained using the UA-MPM system at stretches of (a) 1.0 (b) 1.1 (c) 1.2 (d) 1.26 (e) 1.3 and the corresponding fiber orientation contour plots along thickness direction, demonstrating the recruitment of abluminal collagen at stretch 1.26.

3.3.6 Cellular content

αSMA in the control artery is largely restricted to the medial layer, as shown in Figure 16. Similar to the control artery, a αSMA layer on the luminal side was observed in all three aneurysms. Thickness of the αSMA layer was normalized to the total wall thickness, Figure 19. The normalized αSMA layer thickness for CA-09, CA-25 and CA-26 are 0.69 ± 0.034, 0.79 ± 0.033 and 0.82 ± 0.054 respectively. Notably, differences between normalized αSMA layer thickness of these aneurysms and basilar artery (0.78 ± 0.070) are not statistically significant (p=0.19, 0.81 and 0.49).

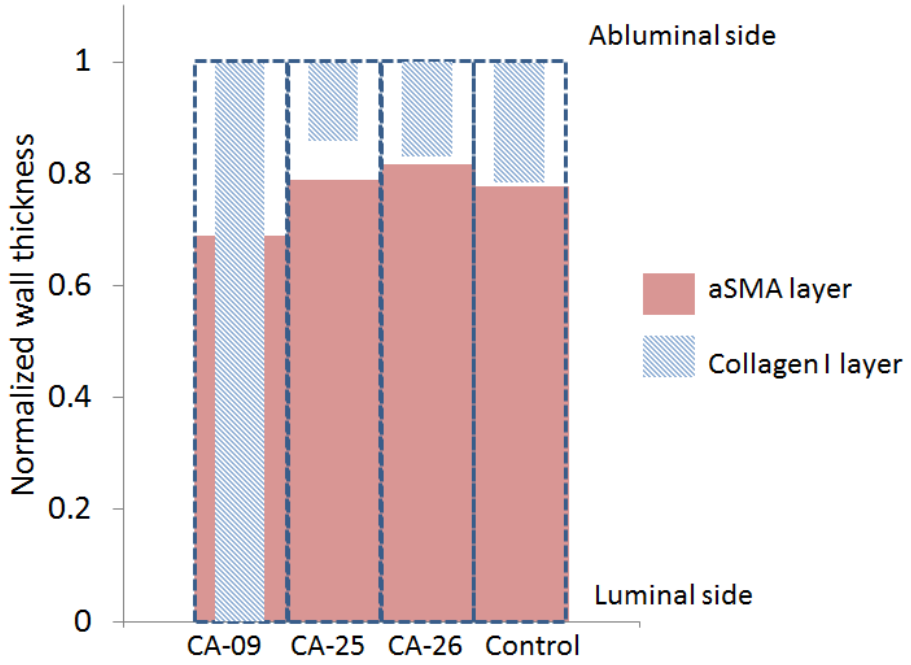

Figure 19. Normalized collagen type I and αSMA layer thickness in aneurysms and control artery.

Cell nuclei were stained with DAPI after the secondary antibody incubation and imaged under confocal microscopy. Cell density was then calculated as cell count per unit area, Figure 20. CA-09 and CA-25 have average cell densities of 5231 ± 490 /mm and 6854 ± 686 /mm^2

respectively, both of which are higher than that of the basilar artery 4540 ± 805 /mm^2. The cell density of CA-26 (3273 ± 659 /mm^2) is lower than that of the basilar artery. However, the difference between cell density of CA-26 and basilar artery was not statistically significant (p=0.13).

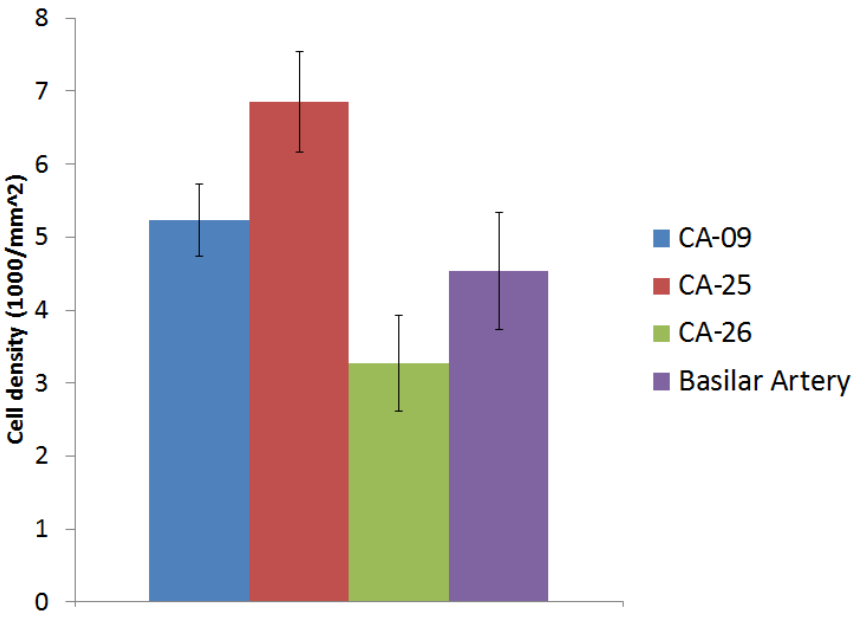

Figure 20. Cell density of CA-09, CA-25, CA-26 and basilar artery with standard deviation. Isolated DAPI signal on the immunofluorescent stained sections (Figure 16) was counted to compute the cell density.

3.4 DISCUSSION

A binary (rupture/unrupture) approach for assessing the structural integrity is necessary if we are using currently available clinical data. In contrast, the FoS is an effective means to provide an assessment of the wall at one instant in time. However, the strength of any structural material can change in time under repeated loading due to material fatigue. It can also change due enzymatic damage such as that arising from collagenases in the case of the vascular wall. Here, we consider

the structural integrity of the aneurysm wall as a means of assessing wall quality. Structural integrity is defined as the ability of structure to support the designed load and perform the designed function during the anticipated life of the structure [77]. We find it valuable to consider the structural integrity of the aneurysm wall, rather than simply the FoS of the wall since it includes the material properties at an instant in time as well as ongoing ability of the wall to perform its structural tasks.

In ex vivo studies, we have the opportunity to use an alternate approach to the rupture/unrupture stratification of aneurysm walls. Rather, we can consider looking for correlations between aneurysm characteristics such as geometry, hemodynamic markers, wall biology and a metric of the structural integrity of the unruptured aneurysm wall. In this work, we consider two cases studies to assess the structural integrity of the aneurysms wall. The FoS of both CA-25 and CA-26 are 5.1 and 4.8, respectively, which suggests that both of them are robust at the time of harvest. It is a conservative estimate since we are using the highest stress for whole dome in the computational study. However, some uncertainty exists since we didn't mechanically test entire dome.

We use the von Mises stress to assess the stress in cerebral aneurysms. This scalar metric is often used to estimate the yield of ductile material due to shear stress [78]. It has been reported that maximum normal stress rather than shear stress is a better metric the failure of AAA, however, little difference was found in results for von Mises and maximum normal stress [79]. This failure criterion could be also true for cerebral artery and aneurysm. Further investigation is needed to better understand the failure mode and thus failure criterion of cerebral aneurysm.

In engineering practice, as well as in the current study, we can only project the expected capacity of the wall to continue to maintain a suitable FoS. Unlike classical engineering

materials such as steel, biological tissues that are endowed with cells have the capacity for maintenance and adaptation over time. In particular, the passive load bearing components of the vascular wall, elastin and collagen fibers, are maintained and manufactured by vascular cells including vascular smooth muscle cells, fibroblasts and even endothelial cells [80, 81]. In this case study, we found robust aneurysm walls have cell density comparable with control artery and are endowed with a substantial αSMA layer, suggesting these walls have the capacity to maintain the ECM structure over time.

3.5 **CONCLUSIONS**

The structural integrity of two unruptured aneurysms was estimated using patient specific biomechanical models. FoS was evaluated based on finite element stress analysis using patient specific geometry and mechanical properties. High FoS for both cases shows that the walls are robust at the time of harvest. Further, investigation of the collagen structure suggests that these walls have capacity to bear biaxial loading, with collagen I found in a distinct outer layer and alpha SMA in an inner layer. Collagen III fibers were distributed throughout the wall. Fibers in the inner layer were concentrated in two main directions, whereas in the outer layer, fibers were more broadly distributed. Dense cell population in the wall is consistent with a wall that is able to maintain its structural integrity through remodeling and renewal of collagen fibers.

4.0 CORRELATION BETWEEN WALL MECHANICAL PROPERTIES AND GLOBAL HEMODYNAMICS IN UNRUPTURED INTRACRANIAL ANEURYSMS

4.1 INTRODUCTION

Improving aneurysm evaluation and clinical management requires an understanding of the pathophysiology of IAs. Hemodynamics is believed to play an important role in initiation, development and rupture of the IAs [27, 82]. Numerous prior studies have been directed at correlating aneurysm rupture with specific hemodynamic markers, such as an abnormally high or low magnitude of WSS and OSI [83-87]. While these studies have produced important and valuable information, the coupling between hemodynamics and the wall structure and mechanical strength, as well as the underlying mechanisms remain largely unknown. It has been suggested that abnormal aneurysmal flow conditions induce endothelial dysfunction, which causes proliferation and luminal migration of SMCs and thrombus formation. As a result of these changes, mural cells are lost and the wall is degraded [21]. In this chapter, we investigate possible associations between hemodynamics within the aneurysm sac and mechanical properties of aneurysm wall. The majority of the content of this chapter was previously published on American Journal of Neuroradiology, 36 (9), 2015: 1695-1703.The permission to republish the material in this PhD dissertation was granted by WILLIAMS & WILKINS CO.

4.2 MATERIALS AND METHODS

4.2.1 Aneurysm tissue handling, mechanical testing and MPM imaging

As described in details in Section 2.3.1, 15 unruptured intracranial aneurysm domes were harvested from surgical clipping. Prior to intervention, aneurysms were imaged with 3D rotational angiography (3DRA). During the intervention, after placing the clip, the aneurysm dome was resected. Harvested tissue samples were placed in prepared vials with 0.9% (weight/volume) saline solution and transported to the lab at University of Pittsburgh (Section 2.3.1). Night of the 16 resected samples were sufficiently large samples (larger than 4mm x 5mm) for mechanical testing in the UA-MPM system (Section 2.3.4). MPM imaging and image post processing methods were described in section 3.2.2.

4.2.2 Hemodynamics modeling

Subject-specific computational fluid dynamics (CFD) models (n=8) were constructed from pre-operative 3DRA images [88]. All aneurysms were located in the anterior circulation. All reconstructions included the internal carotid artery and were extended proximally as much as possible, to minimize the effect of inlet boundary conditions on aneurysm hemodynamics. Pulsatile flow conditions were derived from phase-contrast magnetic resonance measurements in normal subjects [89]. Flow waveforms were scaled with the inflow vessel cross-sectional area to achieve a mean wall shear stress of 15 dyne/cm^2 according to the principle of minimum work (Murray's law) [90]. Vessel walls were assumed rigid and blood a Newtonian fluid with density ρ=1.0 g/cm3 and viscosity μ=0.04 Poise. The 3D incompressible Navier-Stokes equations were

numerically solved with finite elements on unstructured grids with a resolution of 0.2 mm and a time step of 0.01 sec [88]. Computational flow dynamics simulations and associated data analysis of flow parameters were performed by the group of Dr. Juan Cebral at George Mason University.

4.2.3 Data analysis

A number of variables were computed from the CFD simulations to quantitatively characterize the aneurysm hemodynamic environment, including: a) aneurysm inflow rate (Q), b) aneurysm mean velocity (VE), c) inflow concentration index (ICI), d) POD entropy (podent) – a measure of stability of the intra-aneurysmal flow structure, e) vortex core-line length (corelen) – a measure of complexity of the intra-aneurysmal flow pattern, f) shear concentration index (SCI) – a measure of concentration of the wall shear stress distribution, g) mean wall shear stress (WSS), h) mean oscillatory shear index (OSI), and i) percent area under low wall shear stress relative to the parent vasculature (LSA). All quantities were calculated as spatial averages over the aneurysm cavity and time averages over the cardiac cycle. For precise mathematical definitions of these variables and detailed description of the methodology used to compute these quantities see [91, 92].

The stress and strain curves for the aneurysm wall prior to failure is largely exponential in nature [62]. As such, the curves were divided into four regimes, listed in order of increasing load and shown in Figure 21: i) low strain region where the wall is highly elastic (toe region), ii) transition region, iii) high strain regime with a nearly linear response, followed by iv) sub-failure regime, marked by a decrease in slope of the stress strain curve ending with failure of the tissue. The mechanical response was characterized in terms of the following parameters: a) low strain

stiffness - slope of a linear fit for the low strain region, b) high strain stiffness - slope of a linear fit for the high strain region, c) transition strain - strain at intersection of low and high strain stiffness lines, d) ultimate stress – maximum stress prior to failure, e) ultimate strain - the strain corresponding to ultimate stress, and f) ultimate tension (engineering) - product of ultimate stress (engineering) and unloaded thickness. The ultimate tension provides a measure of the ability of the wall to withstand loading. In contrast, the ultimate stress and strain are intrinsic material properties characterizing failure behavior.

Linear regression analysis was performed to explore possible correlations between hemodynamic variables and wall mechanical properties. All correlation analyses were carried out using Minitab.

4.3 **RESULTS**

Mechanical behaviors of the aneurysms are presented in Table 7 and Figure 21, and their corresponding flow characteristics are given in Table 8. Correlations for both high strain stiffness and ultimate strain and hemodynamic variables reached statistical significance. Table 9 lists the slope of the linear regression, the correlation coefficient (R^2) and the p-value of the correlation between each hemodynamic variable and the measured ultimate strain and high-strain stiffness. For $p<0.05$ the slope of the corresponding linear regression is significantly different from zero with a 95% confidence.

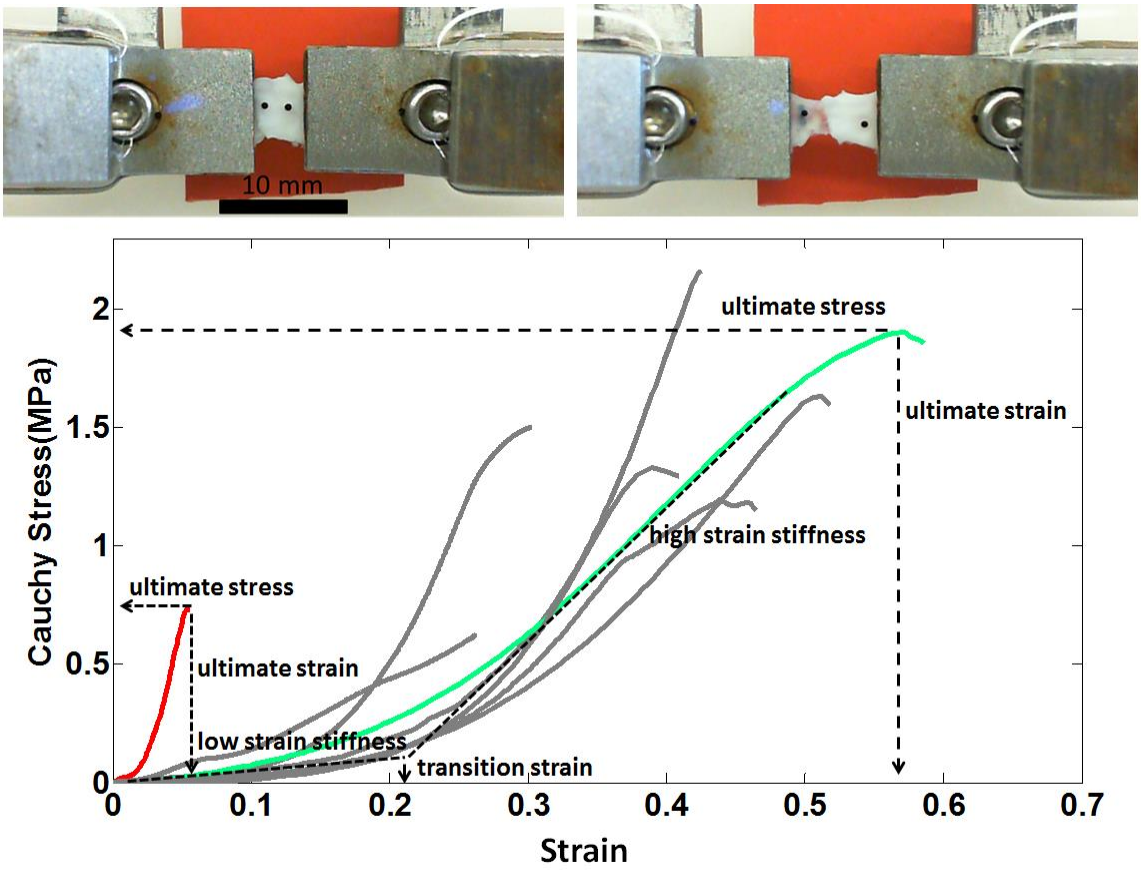

Figure 21. Stress-strain relationships (bottom). Examples of an aneurysm with stiff walls and low ultimate strain and stress (CA-15), and an aneurysm with softer walls and greater ultimate stress and ultimate strain (CA-26) have been highlighted in red and green, respectively. Top insert: picture of a sample with grips before stretching (left) and after it fails (right). Note that the tear occurs near the middle of the sample, not at the grips.

Table 7. Mechanical characteristics of cerebral aneurysms

ID	Transition Strain	low stiffness (MPa)	high stiffness (Mpa)	ultimate strain	ultimate stress(MPa)
CA-1	0.16	0.35	12.24	0.3	1.5
CA-11	0.11	1.66	2.93	0.26	0.63
CA-12	0.28	0.58	14.09	0.42	2.16
CA-15	0.02	2.35	24.41	0.05	0.73
CA-25	0.26	0.24	6.18	0.51	1.63
CA-26	0.22	0.9	5.43	0.57	1.9
CA-39	0.24	0.34	6.38	0.44	1.2
CA-46	0.24	0.22	9.11	0.38	1.34

The relationships between hemodynamic quantities and ultimate strain, ultimate stress and high-strain wall stiffness are presented in Figure 22, Figure 23 and Figure 24, respectively. The lines correspond to the straight lines fitted by the linear regression (slope and intercept given in Table 9). Correlations that reached statistical significance have been indicated with a '*'.

Table 8. Hemodynamic characteristics of cerebral aneurysms

ID	Q (ml/s)	ICI	VE (cm/s)	podent	corelen (cm)	SCI	WSS (dyne/cm^2)	OSI	LSA
CA-1	1.52	2.00	9.53	0.31	2.86	4.39	19.57	0.019	49.3%
CA-11	0.58	0.48	6.68	0.30	1.68	11.58	11.13	0.010	79.7%
CA-12	0.71	0.65	10.18	0.62	2.84	6.00	25.30	0.025	75.5%
CA-15	3.52	2.28	23.62	1.03	5.65	3.92	42.87	0.056	59.5%
CA-25	0.09	0.21	0.98	0.36	0.30	21.70	1.31	0.020	97.1%
CA-26	0.61	0.70	7.24	0.29	2.80	10.22	14.17	0.016	69.1%
CA-39	0.99	0.85	8.55	0.17	3.02	4.23	14.38	0.007	40.2%
CA-46	2.18	1.74	14.11	0.11	1.46	2.80	23.27	0.004	62.3%

The ultimate strain is seen to decrease with aneurysm inflow rate, mean velocity, inflow concentration, flow instability, flow complexity, WSS and OSI; while it increases with the concentration of the WSS distribution and area under low WSS. However, only the associations with inflow rate, mean velocity, and mean WSS reached statistical significance. Ultimate stress followed the same trends but did not reach statistical significance.

The high-strain wall stiffness increases with inflow rate, mean velocity, inflow concentration, flow instability, flow complexity, WSS and OSI; while it decreases with the concentration of the WSS distribution and area under low WSS. The relation to velocity, flow instability, WSS and OSI reached statistical significance.

Table 9. Linear regression of hemodynamic variables against wall ultimate strain and material stiffness at high strain (past the toe region). * Indicates statistically significant

wall property	flow variable	slope	R^2	p-value
ultimate strain	Q	-0.12	0.617	0.021*
	VE	-0.019	0.597	0.025*
	ICI	-0.14	0.474	0.059
	podent	-0.36	0.423	0.081
	corelen	-0.067	0.412	0.086
	SCI	0.011	0.186	0.287
	WSS	-0.010	0.535	0.039*
	OSI	-6.44	0.414	0.085
	LSA	0.24	0.069	0.531
material stiffness at high strain	Q	5.01	0.659	0.014*
	VE	1.20	0.717	0.008*
	ICI	6.44	0.531	0.040*
	podent	19.9	0.741	0.006*
	corelen	3.48	0.629	0.019*
	SCI	-0.52	0.227	0.232
	WSS	0.51	0.813	0.002*
	OSI	369.3	0.772	0.004*
	LSA	-0.101	0.065	0.53
ultimate stress	Q	-0.23	0.229	0.23
	VE	-0.032	0.162	0.32
	ICI	-0.23	0.110	0.42
	podent	-0.31	0.029	0.69
	corelen	-0.092	0.073	0.51
	SCI	0.012	0.021	0.73
	WSS	-0.010	0.057	0.57
	OSI	-6.02	0.034	0.66
	LSA	0.6	0.041	0.63

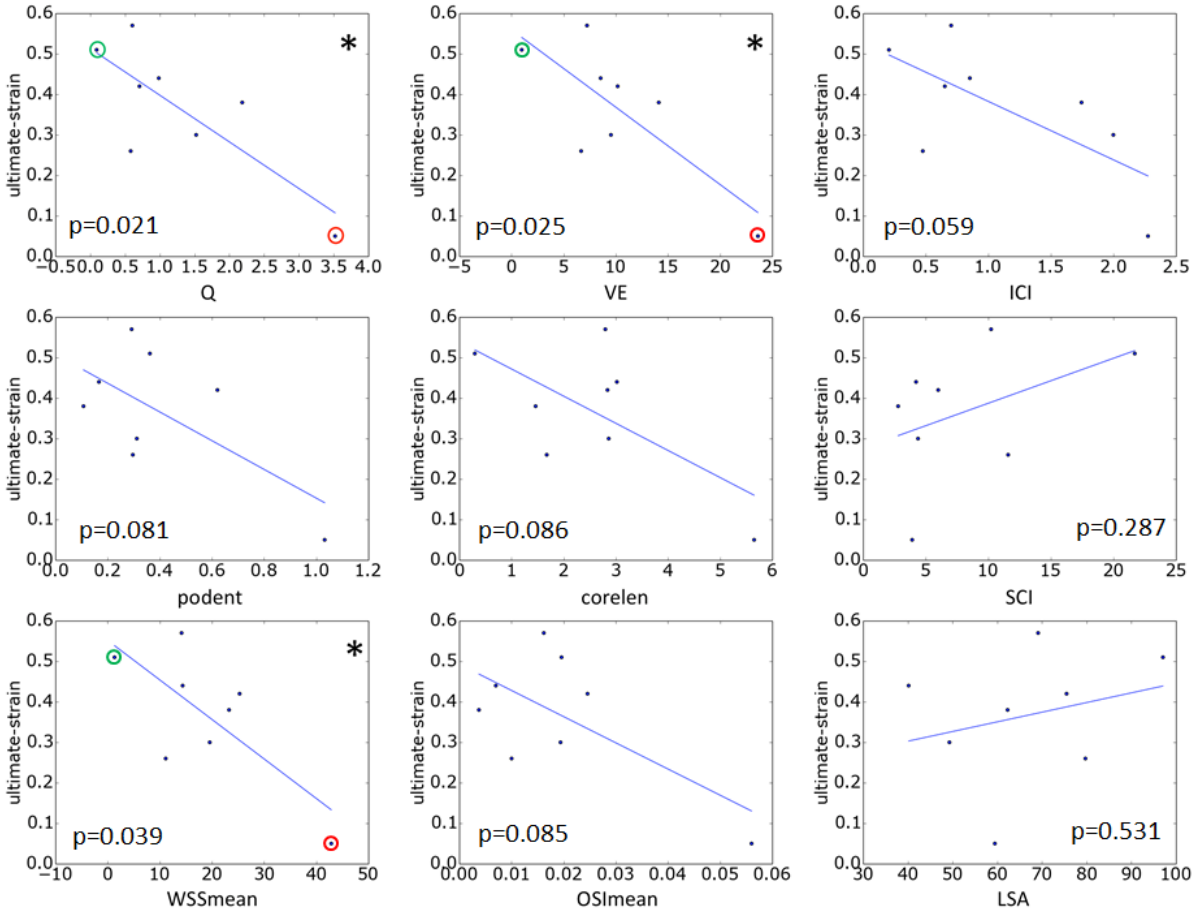

Figure 22. Relationship between hemodynamic variables and wall ultimate strain. Correlations that reached statistical significance (95% confidence) are marked with a *. In the top-left panel aneurysms CA-26 and CA-15, exemplified in Figure 25, are marked with green and red circles, respectively.

Two aneurysms (CA-26 and CA-15), representing distinct mechanical behaviors, are considered in greater detail in Figure 25 to illustrate these trends. In particular, with respect to failure properties, the wall of CA-26 (green circle in Figure 22 and green curve in Figure 21) had the largest ultimate strain, largest ultimate tension and nearly the largest ultimate stress. The wall of CA-15 (red circle in Figure 22 and red curve in Figure 21) had the lowest ultimate strain, lowest ultimate tension and the second lowest ultimate stress. With regards to the nature of the loading curve, CA-26 had the largest transition strain and nearly the lowest stiffness in the high

strain regime. In contrast, the walls of CA-15 had the lowest transition strain and the largest stiffness in the high strain regime. Namely, CA-26 was stronger with a softer response at high strain than CA-15.

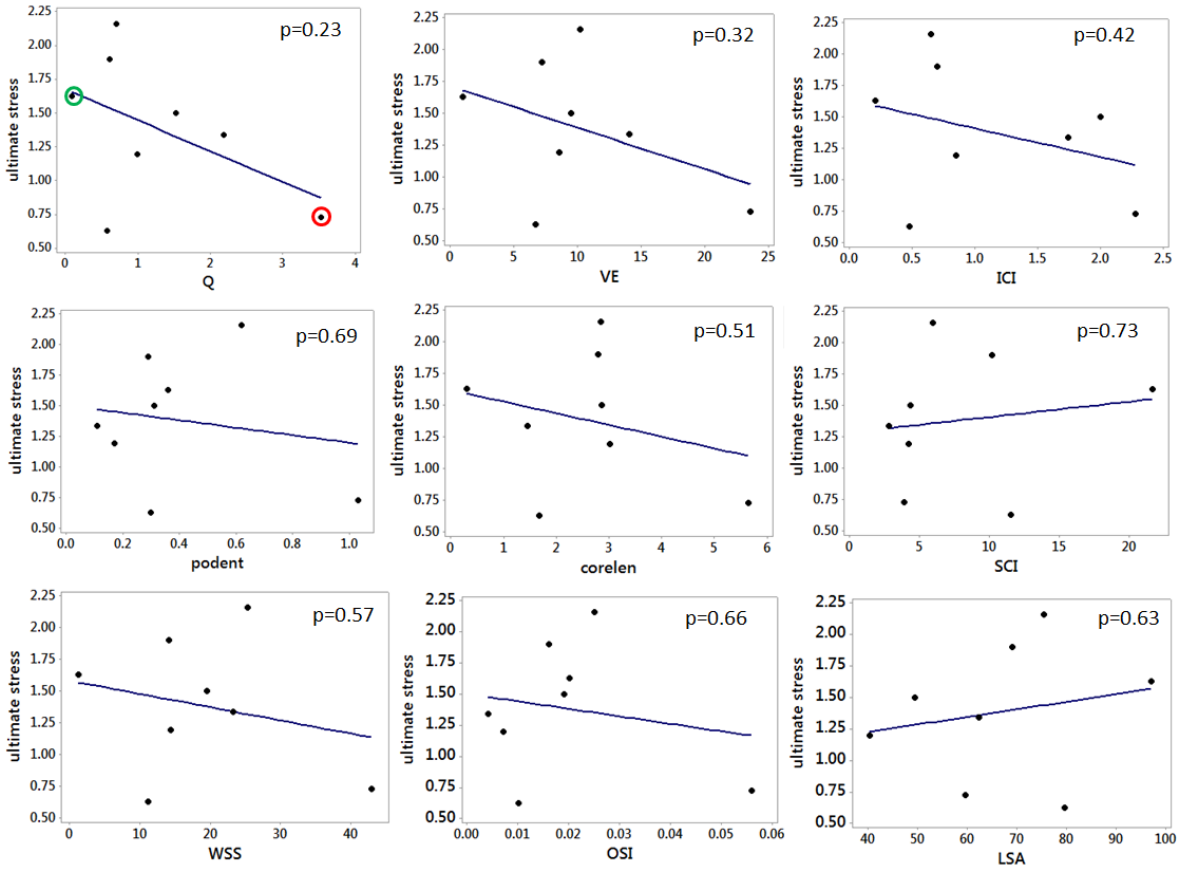

Figure 23. Relationship between hemodynamic variables and ultimate stress. No correlations has reached statistical significance (95% confidence). In the top-left panel aneurysms CA-26 and CA-15, exemplified in Figure 25, are marked with green and red circles, respectively.

Flow visualizations of CA-26 and CA-15 along with MPM images of the collagen fibers of each aneurysm in their unloaded configurations are shown Figure 25. Iso-velocity surfaces (top left frame of each panel) show a stronger inflow stream and larger intra-saccular velocity in CA-15, which is consistent with higher values of inflow rate and mean velocity in Table 8. Flow streamlines (top center frame of each panel) also demonstrate stronger intra-saccular flow

penetrating deeper into the cavity of CA-15. Vortex core-lines (top right frame of each panel) indicate a more complex and unstable flow pattern within CA-15, which is consistent with higher values of POD entropy and corelen in Table 8. The WSS distribution (bottom left frame of each panel) shows higher values and more irregular WSS distribution in CA-15, which is consistent with the increased values of the global measures of WSS (spatial average of WSS over entire dome) seen in Table 8.

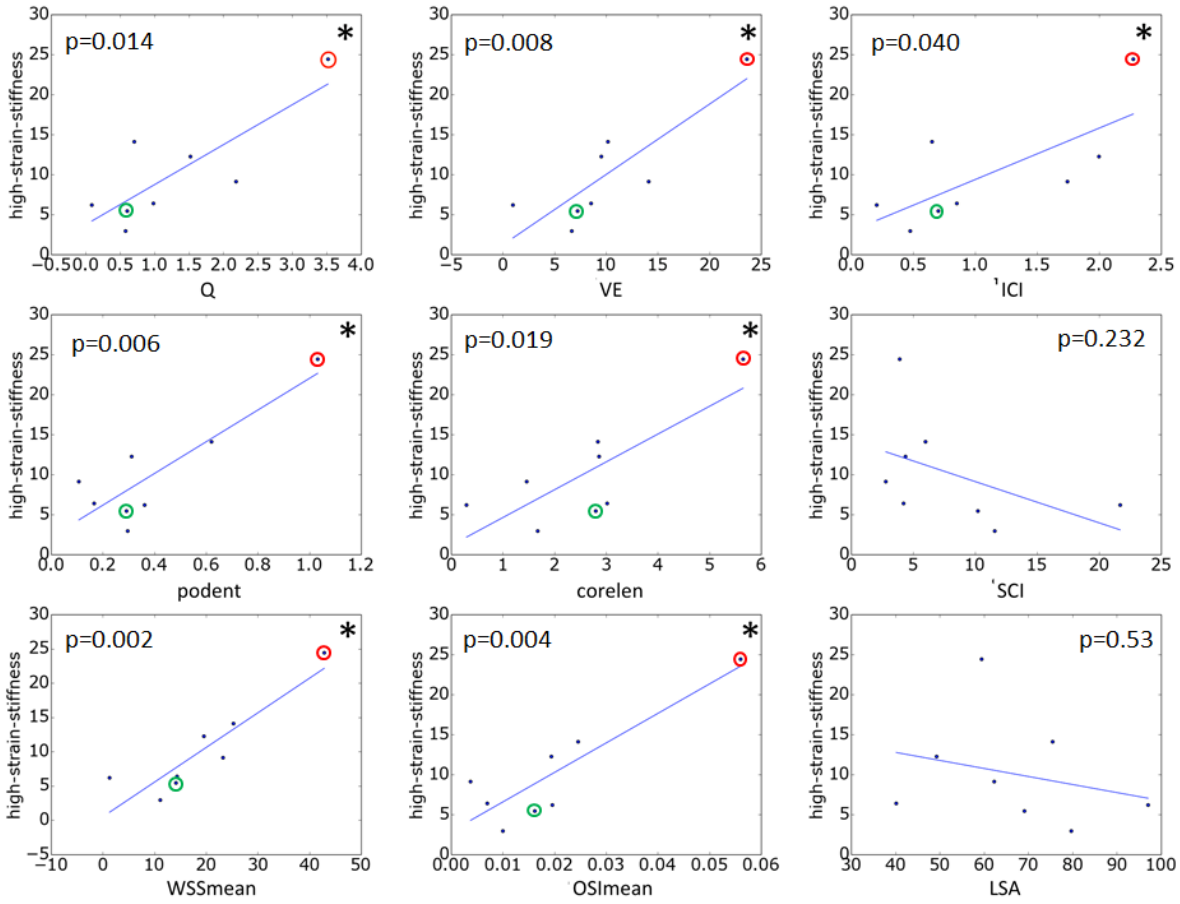

Figure 24. Relationship between hemodynamic variables and wall stiffness at high strain (MPa). Correlations that reached statistical significance (95% confidence) are marked with a *. In the top-left panel aneurysms CA-26 and CA-15, exemplified in Figure 25, are marked with green and red circles, respectively.

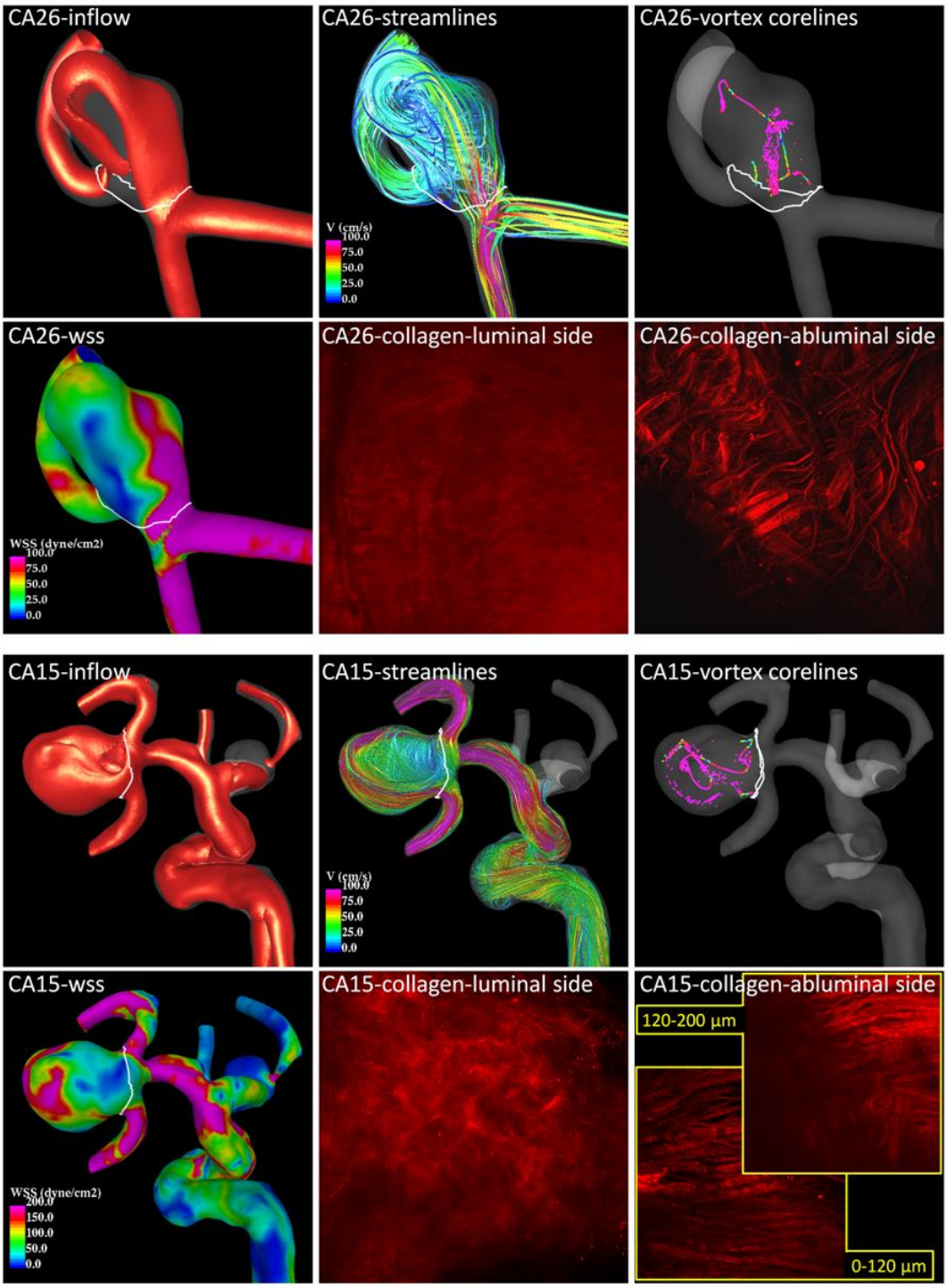

Figure 25. Flow at the peak systole and collagen fibers in two example aneurysms. Aneurysm CA-26 (top panel) corresponds to the green circles of Figure 22 and Figure 24, and the green curve of Figure 21. Aneurysm CA-15 (bottom panel) corresponds to the red circles of Figure 22 and Figure 24, and the red curve of Figure 21. See Appendix E for Flow of other 6 aneurysm cases.

The collagen fiber architectures of these two aneurysms are qualitatively different. On the luminal (medial) side, CA-26 shows a denser distribution resulting in a smoother and more homogeneous appearance under the MPM than CA-15. On the abluminal (adventitial) side, the fibers of CA-26 appear to have more than one preferred orientation direction. The fibers seem to form an interlaced mesh pattern and exhibit a larger degree of waviness. In contrast, the fibers of CA-15 close to the abluminal surface appear to follow roughly a single orientation without much interlacing, while the fibers deeper in the wall are not unidirectional. Fibers of CA-15 exhibit less waviness and are in general thicker. The wall thickness was 450 μm in CA-26 versus 130 μm in CA-15, shown in Figure 26.

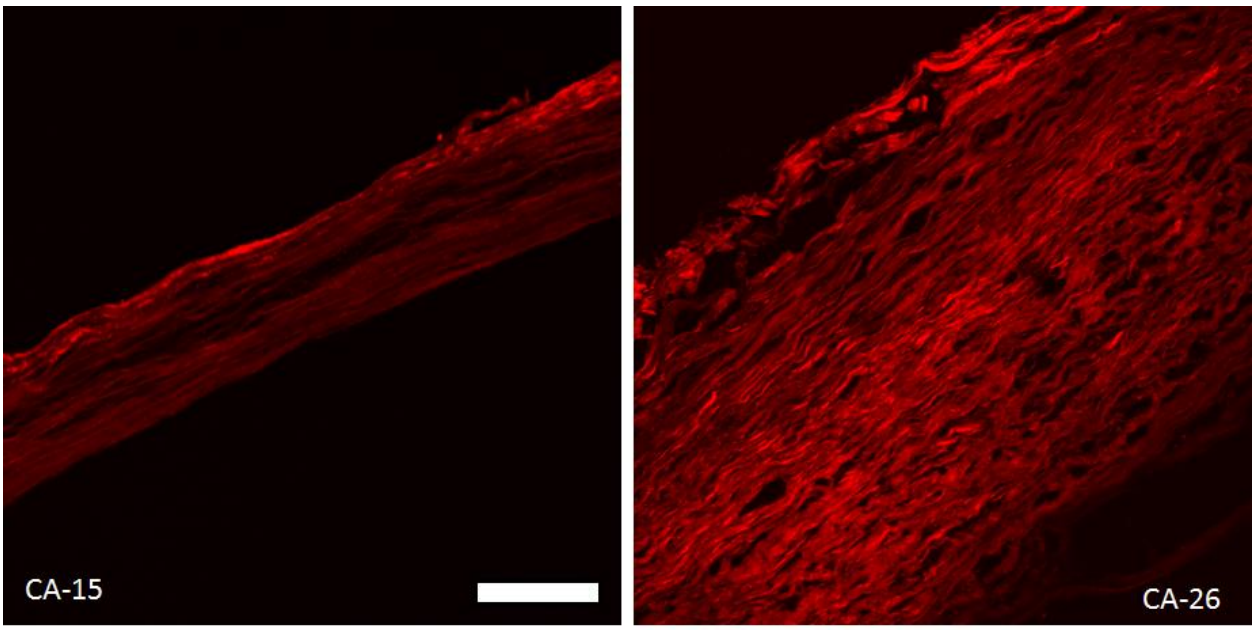

Figure 26. Cross section view of CA-15 and CA-26, Cryosectioned samples were imaged using multiphoton microscopy, scale bar =100 um

4.4 DISCUSSION

Although it is generally accepted that aneurysm evolution is governed by progressive degradation of the wall in response to abnormal hemodynamics [56, 63], the detailed mechanisms that drive the degeneration and weakening of the wall remain unknown [64]. Previous studies have identified possible associations between different hemodynamic factors and aneurysmal rupture [20]. However, it is unclear which parameters are responsible for the mechanisms controlling wall degradation and aneurysm rupture or stabilization [60]. Determining the influence of intra-aneurysmal hemodynamics on wall structure and strength has the potential for resolving this issue.

A prior study found rupture site could best be explained in eight of nine aneurysms through an association of thinner and stiffer walls with regions of abnormally high WSS [65]. Results from the current study seem to support the idea that large flow activity within the aneurysm, as characterized by high velocity and inflow rate, high WSS and OSI, and complex unstable flow structures tend to be associated with lower ultimate strains and stiffer walls at high strain. While parallel trends with respect to ultimate stress did not reach statistical significance, they were in agreement with this trend and warrant further study. In addition, the trends of this study suggest increasing the area exposed to low WSS increases the ultimate strain and decreases the high strain stiffness of the aneurysm wall.

In the low strain region, collagen fibers are found to straighten and reorient as they are recruited to load bearing [62]. This can be seen in Figure 27, which displays MPM images of tissue from CA-26 under increasing uniaxial load, and corresponding histograms of the distribution of fiber orientations calculated following [66]. In the toe region, fibers straighten as the tissue is loaded. As loading progresses through the transition regime, increasing numbers of

fibers are straightened and recruited to load bearing. Finally, in the high strain regime, small changes in stretch require large increases in load, consistent with the extensive state of recruitment of the collagen fibers. Hence, the high-strain stiffness of the tissue reflects the properties of recruited fibers. Stiffer behavior in the aneurysm wall, would suggest a higher density of collagen fibers or a stiffer collagen fabric, perhaps due to increased cross linking. The larger waviness of collagen fibers in CA-26 could explain its increased toe region relative to CA-15 that showed little waviness. The magnitude of ultimate strain is influenced by a number of factors including the size of the toe region, high strain stiffness and ultimate stress. CA-15 failed at lower strain relative to other samples, consistent with the combined effects of a smaller toe region, greater high strain stiffness and lower ultimate stress. The increased stiffness at high strain in this sample is consistent with a higher density of abluminal collagen fibers. In contrast, CA-26 failed at higher strain, which is consistent with its longer toe region, lower high-strain stiffness and greater ultimate stress.

Our results suggest the hemodynamic environment within the aneurysm sac influences the mechanical behavior of the aneurysm wall that in turn is strongly dependent on the architecture and quality of collagen fibers. The direct connection between hemodynamic conditions and collagen architecture has not yet been explored and is the focus of our ongoing research.

We assessed the connection between global hemodynamic variables and wall mechanical and failure properties. Such global hemodynamic characteristics are appealing because they are less sensitive to local geometric features. While this is a sound approach, in some aneurysms local flow properties may cause focal changes to the wall, which can in principle be the cause of failure. While some of the hemodynamic parameters considered here such as shear concentration

index reflect local features, the analysis was not performed locally. In the future, it would be valuable to find ways to directly map local mechanical properties to local hemodynamics to extend the current study.

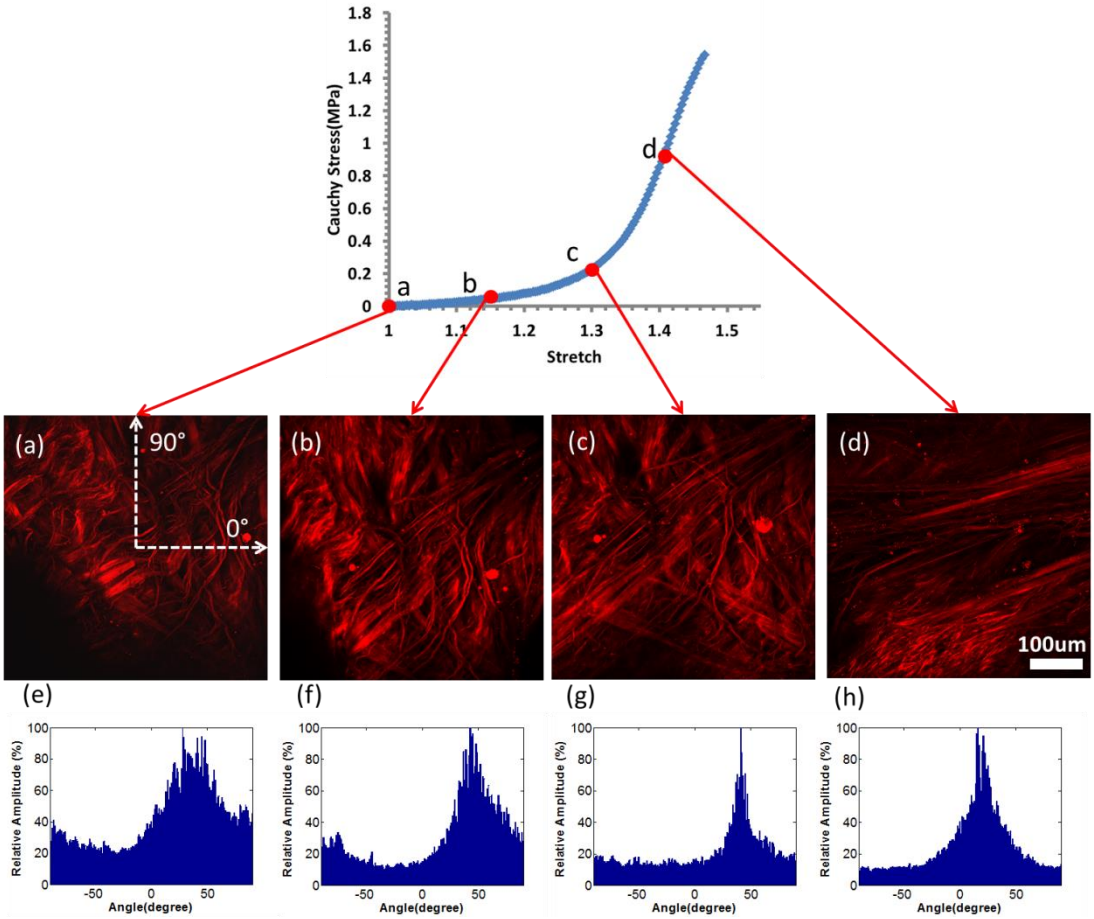

Figure 27. Abluminal view of collagen fiber recruitment during uniaxial loading of aneurysm sample CA-26 (green in Figures 1-3) obtained using the UA-MPM system. The images are obtained at stretches of (a) 1.0 (b) 1.15 (c) 1.3 (d) 1.4 and are formed from a projection of stacks over an approximately 95 μm depth of tissue. (e), (f), (g) and (h) are the histograms of fiber orientation distribution of the MPM images at stretch of 1.0, 1.15, 1.3 and 1.4 respectively. 0° is the horizontal direction on the image, and 90° is the vertical direction on the image (shown in (a)).

The current study considers unruptured aneurysms. While the unruptured population appears to harbor aneurysms vulnerable to rupture [62], it would be valuable to explore whether

trends identified in this study are seen in ruptured aneurysms. The ruptured population is known to include a sub-population with thin hypocellular walls devoid of endothelial cells [21]. Hence, this sub-population may represent a later stage of aneurysm progression where the role of hemodynamics is fundamentally different than for the unruptured population.

The current study suffers from some limitations. The trends reported in this paper need to be confirmed with larger datasets. A number of idealizations are imposed in the hemodynamics studies such as modeling the aneurysm wall as rigid and blood as a single-phase fluid with constant viscosity. Although variations in the aneurysmal hemodynamics were found between the rigid wall model and fluid structure interaction (FSI) model, the flow pattern and WSS distribution do not alter considerably [67, 68]. However, if we are interested in the magnitude of wall motion, then the choice of wall properties could be an important factor [41]. Our flow conditions were derived from normal subjects and scaled with the patient-specific inflow vessel sizes, but the effects of co-morbidities such as hypertension were not considered. While our assumptions may be reasonable [69], the effects of other co-morbidities should be investigated in future studies. In addition, we considered uniaxial loading, recognizing that in vivo loading is closer to equi-biaxial. This choice is motivated largely by the desire to test the tissues to failure coupled with the small size of the aneurysm samples. Nevertheless our preliminary results are the first to study the link between hemodynamics and aneurysm wall properties and suggest several provocative hypotheses about the relationship between in vivo hemodynamics, wall structure and wall mechanical properties that need to be tested with larger series of human aneurysm tissue samples.

4.5 **CONCLUSIONS**

In unruptured intracranial aneurysms, wall ultimate strain is negatively correlated with aneurysm inflow rate, mean velocity and mean wall shear stress. Failure stress shows same trends but not reaching statistical significance. Wall stiffness in the high strain region is positively correlated with aneurysm inflow rate, mean velocity, wall shear stress, flow complexity and stability.

5.0 INVESTIGATION OF LOCAL FLOW AND LOCAL WALL STRUCTURE CONNECTION IN HUMAN INTRACRANIAL ANEURYSMS

5.1 INTRODUCTION

The objective of chapter is to study the relationship between the local hemodynamics and the local structure of the wall of intracranial aneurysms in order to better understand the mechanisms responsible for the progressive degeneration of the wall that can eventually lead to aneurysm rupture. We have shown the diversity in strength and structure of unruptured aneurysms and have suggested connections between global hemodynamic conditions and material properties of cerebral aneurysms. However, the connections between the local hemodynamic conditions and wall structure have not been studied, largely because of the lack of an appropriate methodology to make these connections.

Here we illustrate a methodology of mapping local hemodynamics to the local wall structure with an aneurysm case. In particular, the methodology introduced here employs a computational mapping tool that enables surgeons to mark the location of the resected tissue and visible landmarks directly on the anatomical model, while in the surgical suite. High resolution micro-CT scans of the tissue specimen are then used to create 3D models of the harvested specimen of aneurysm tissue. These specimen models are then aligned on the 3D reconstructed anatomical model, aided by the mapping tool as well as visible landmarks. Once this mapping

is complete, data obtained for the harvested tissue, such as collagen fiber orientation and wall thickness can also be related to local hemodynamics on the anatomical model.

5.2 METHODS

5.2.1 Tissue harvesting and resection documentation

During the surgical intervention, after exposing the aneurysm and placing the clip, the aneurysm dome is marked with a surgical pen to later help determine its orientation, and the dome is then resected. The harvested tissue sample is placed in a vial with a 0.9% (w/v) saline solution and transported in an insulated cooler to the University of Pittsburgh for ex-vivo imaging.

In order to document the region of the aneurysm that was resected, a 3D virtual marking tool has been developed by collaborator J. Cebral that can be used directly in the surgical suite. Three-dimensional rotational angiography (3DRA) images were acquired prior to intervention. 3D anatomical model was constructed from the 3DRA images and loaded into the marking tool. The neurosurgeon rotates the 3D model to the same orientation as the exposed aneurysm, and then interactively delineates the resected region on the surface of the anatomical model and places marks analogous to the marks drawn in vivo with the surgical pen. This information is later used to align the tissue sample to the 3D CFD anatomical model.

5.2.2 Micro CT scan

In order to map the domain of the resected tissue to the anatomical model, it is first necessary to generate a 3D model of the harvested tissue. The resected aneurysm tissue is fixed in 2% paraformaldehyde for 2 hours, mounted in a Styrofoam container sealed with saline-soaked gauze, and then imaged at 8 μm/voxel resolution with a Bruker SkyScan 1272 high-resolution micro-CT system (Bruker microCT, Kontich, Belgium). Images are then reconstructed using the software provided with the micro-CT system and stored as BMP image stacks. Three-dimensional reconstructions of the inner and outer surfaces of the wall of the resected aneurysm sample are created from the BMP stacks using Mimics 13 (Materialise NV, Leuven, Belgium). The distance map between these surfaces is then computed to quantify the local thickness of the wall using Geomagic Studio 12 (3D Systems, Rock Hill, SC). Thickness is reported as the shortest distance from a point on the outer surface to any point on the inner surface.

5.2.3 Aneurysm 3D model to sample mapping

The micro-CT surface reconstruction of the resected dome is interactively aligned to the 3DRA-based anatomical model. For this purpose the 3D virtual marks on the anatomical model, the surgical pen marks, and any geometric feature and/or landmarks (such as blebs or regions of high surface curvature, etc.) are used as guides to identify the dome orientation and position on the anatomical model.

5.2.4 Hemodynamics and MPM imaging

Hemodynamics in the aneurysm sac were analysed by using patient-specific computational fluid dynamics (CFD) models constructed from pre-operative 3DRA images (Section 4.2.2). Flow variables such as wall shear stress (WSS) and oscillatory shear index (OSI) are computed on the aneurysm surface. On the other hand, aneurysm wall structure was assessed experimentally by multiphoton imaging of harvested aneurysm domes (Section 2.3.5). Imaging can be performed for specific sub-regions of the 3D model chosen based on the local hemodynamics, (e.g. WSS distribution), or alternatively, for a set of sub-regions regularly distributed across the resected dome, blinded to the hemodynamic results. Here, we illustrate both these approaches.

MPM images corresponding to layers at different depths through the wall were blended together using maximum intensity projections (MIP) to visualize and characterize the collagen fibers and their architecture. Original MPM images were analyzed using the method described in section 3.2.2 to investigate the through-thickness orientation distribution. Fiber diameters were measured using the method described in section 2.3.5.

5.3 RESULTS

The methodology of mapping local hemodynamics to local wall structure is illustrated with a 10 mm right middle cerebral artery (MCA) bifurcation aneurysm. The aneurysm was imaged with 3DRA prior to the surgery, shown in Figure 30 (a). The 3D model generated from 3DRA image was used for tissue marking right after the surgery.

During the surgery, after placing the clip, Figure 28 (a), a purple dot is placed on the dome of aneurysm using the tissue marking pen, and then the aneurysm tissue is harvested, Figure 28 (b & c), and fixed in 2% paraformaldehyde for two hours. Subsequently, the aneurysm dome was scanned with the high resolution micro-CT. Figure 28 (d & e) shows the surface reconstruction of the aneurysm dome from the micro-CT scan.

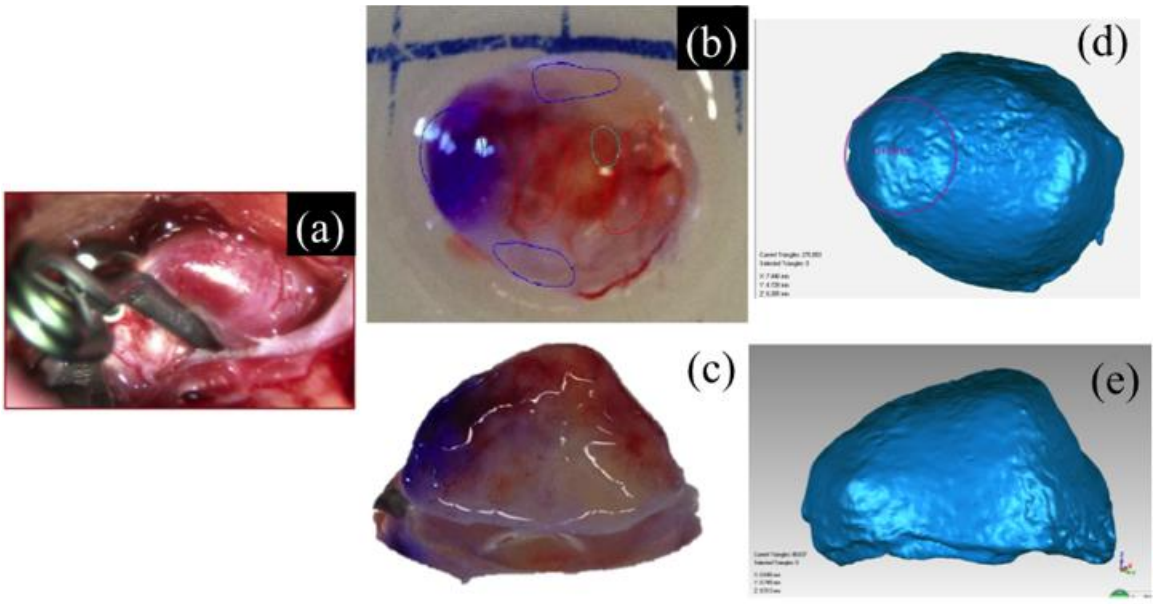

Figure 28. Tissue harvesting and micro-CT imaging: a) in-vivo image of aneurysm clipping, b and c) resected aneurysm dome showing purple marks from surgical marking pen, d and e) 3D reconstructed image of resected dome created using high resolution micro-CT images.

In order to calculate the local wall thickness, the inner and outer surface of the aneurysm wall was reconstructed from the micro-CT images and separated shown in Figure 29 (a). Wall thickness was computed as the shortest distance from a point on the outer surface to the inner surface. The contour plot of wall thickness distribution was shown in Figure 29 (b).

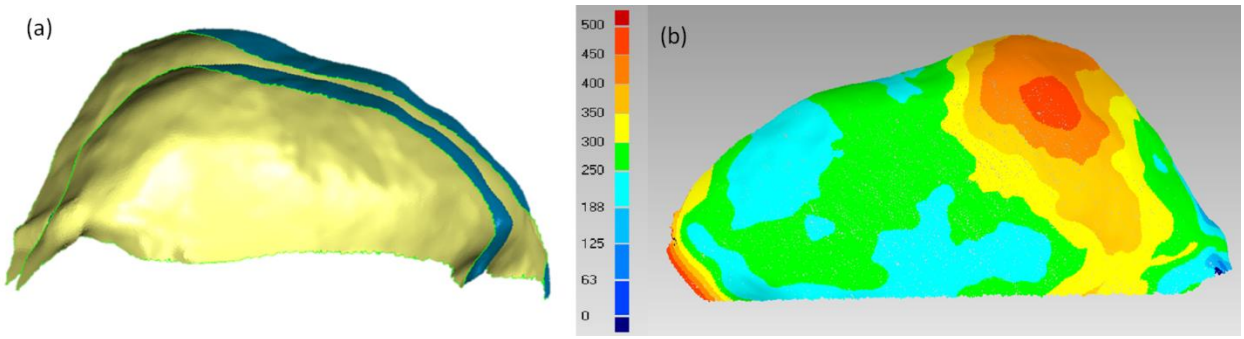

Figure 29. Wall thickness of the resected dome: a) inner and outer surfaces of the aneurysm wall reconstructed from high resolution micro-CT data for resected dome (luminal view), b) wall thickness map (unit: um) calculated as he shortest distance from a point on the outer surface to any point on the inner surface (abluminal view).

The 3D anatomical model was imported into the custom designed software and aligned to the roughly same orientation of the exposed aneurysm during surgery, Figure 30 (a). The resected region of the dome (red line in Figure 30 (b)) and the location of the surgical pen marker (blue dot in Figure 30 (b)) were marked by the neurosurgeon. Figure 30 (e & f) shows the marked 3D anatomical model superposed with the picture of aneurysm sample. The 3D model reconstructed from micro-CT was also aligned with the anatomical model, shown in Figure 30 (c & d).

Visualizations of the CFD results at peak systole are presented in Figure 31. This figure shows, in the same orientation of Figure 28e, iso-velocity surfaces highlighting the inflow jet into the aneurysm (a), instantaneous streamlines colored according to the velocity magnitude illustrating the intrasaccular flow pattern (b), the distribution of wall shear stress magnitude (c), and the WSS vectors (d).

Time average WSS is inhomogeneous in the dome of the aneurysm, as shown in Figure 32. Values of WSS of 5 dyne/cm$^{\wedge 2}$ and 70 dyne/cm$^{\wedge 2}$ have been suggested as critical values, above and below which endothelial health suffers [70]. Regions of low (<5 dyne/cm$^{\wedge 2}$) and high

(>70 dyne/cm^^{2}) WSS were outlined with blue and red colour on the CFD model, and the corresponding regions of the aneurysm were identified on the resected dome and subsequently imaged under MPM to assess the local collagen structure.

Qualitatively, collagen fibers imaged on the abluminal side of the aneurysm wall in the regions of normal to low WSS (MPM images 1, 2 and 4 in Figure 32) had a more coherent structure with long fibers, and the orientation contour plots through the wall thickness show that fibers are mainly aligned in two principal orientations. In contrast, fibers in regions of high WSS (MPM images 3 and 5) had a more pathological appearance compared with the native artery [62], showing thinner and shorter fibers aligned in one main direction (MPM image 3) and gaps between fibers.

A series of 500 μm x 500 μm MPM images were acquired uniformly distributed on the surface of the resected dome, as shown in Figure 33(a). Corresponding sub-regions were marked on the micro-CT surface reconstruction of the resected dome. Collagen fiber diameters were measured on the MPM images and averaged over each image. Similarly, wall thickness was averaged over each sub-region. The interpolated WSS and OSI fields (shown in Figure 33 (b) and (e), respectively) were averaged over each sub-region and compared to corresponding fiber diameters and wall thickness. Figure 33(c) and (d) show scatter plots of fiber diameter and wall thickness against mean WSS, respectively. The blue lines represent linear regression curves and p are the corresponding p-values. Similarly, Figure 33(f) and (g) show plots of fiber diameter and wall thickness against OSI, respectively. Although the linear regressions did not reach statistical significance, a tendency of increasing wall thickness with increasing WSS and OSI, and a decrease of fiber diameter with increasing OSI can be observed. Qualitatively, collagen fibers look healthy and well organized in region 2 where the WSS reaches normal values, while in

regions 6 and 11 the wall shear stress is higher and the collagen fibers look more inhomogeneous and disorganized.

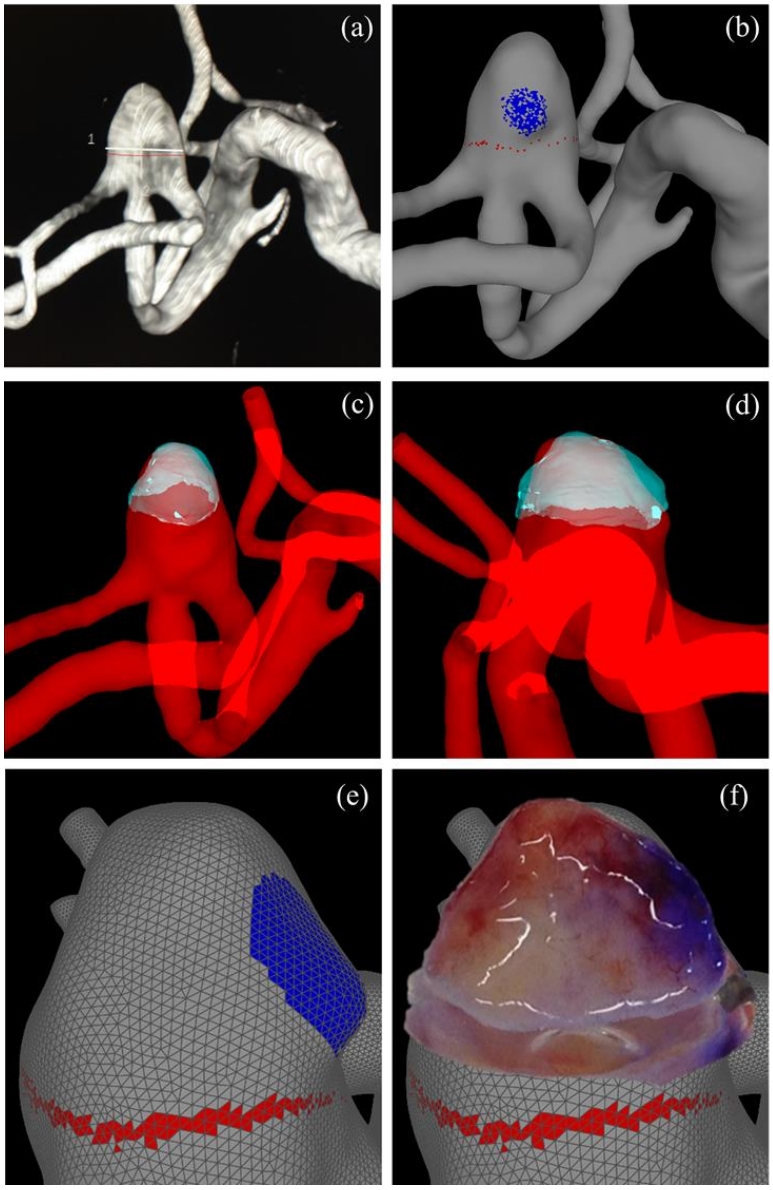

Figure 30. Alignment of resected dome and anatomical model: a) 3DRA image oriented according to surgical approach, b) anatomical model marked post-surgery showing boundary of resected tissue (red) and region of bleb (blue) , c and d) alignment of micro-CT reconstruction of resected dome (light blue) and 3D anatomical model (red), e) marked anatomical model showing boundary of resected tissue (red) and bleb region (blue), f) superposition of picture of resected dome on anatomical model.

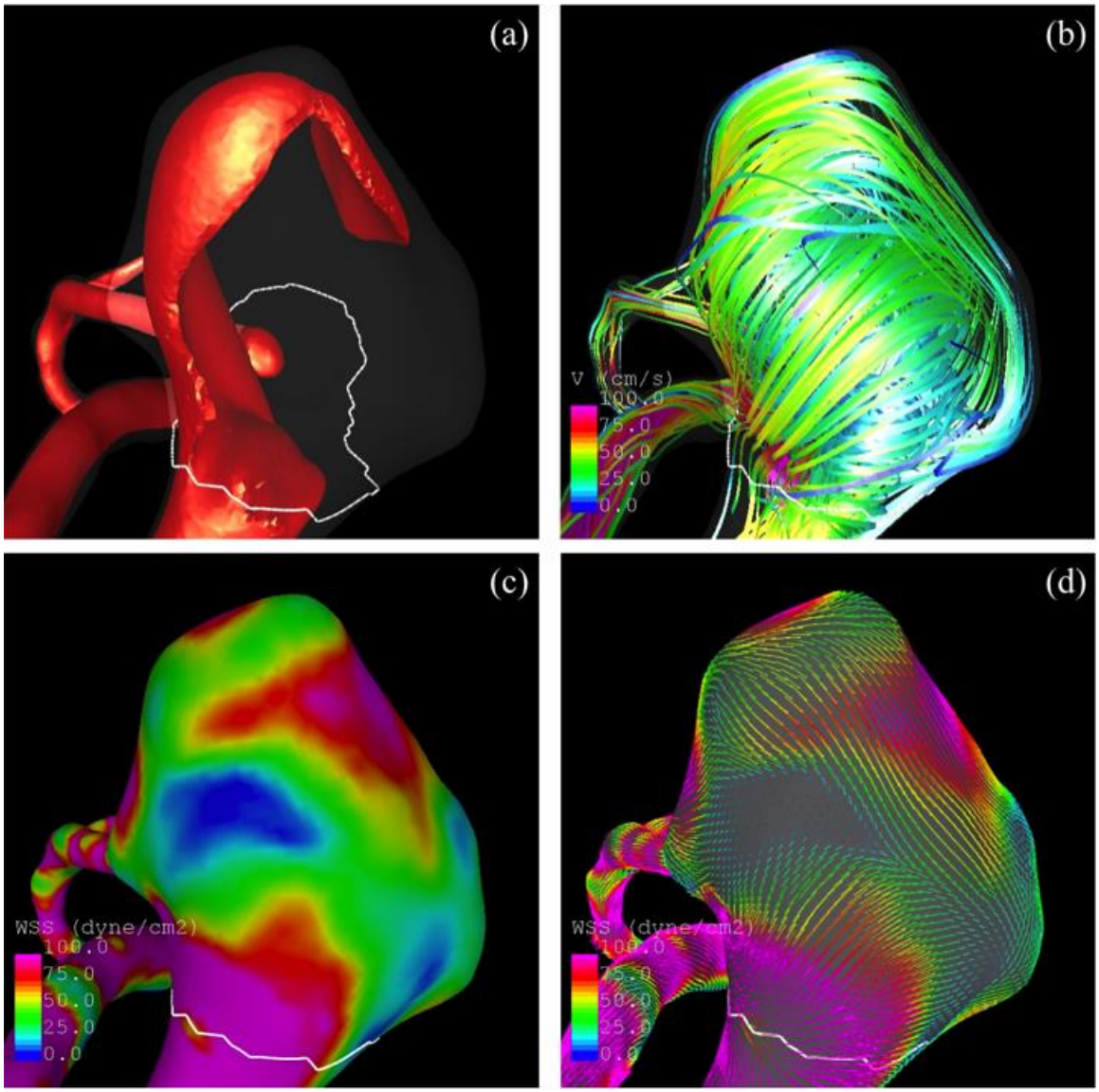

Figure 31. Peak systole flow visualization: a) inflow stream, b) streamlines, c) wall shear stress magnitude, d) WSS vectors.

Collagen fiber architecture at 11 sub-regions was shown in Figure 34. The corresponding orientations through the wall thickness in region 1 to region 10 exhibit one preferred direction almost through the thickness, and another preferred direction close to the luminal side, while region 11 shows completely different orientation distribution with only one preferred direction,

Figure 35. The histograms of collagen fiber have been averaged through the thickness, and scaled to maximum relative amplitude of 100%. The mean WSS vectors distribution have been

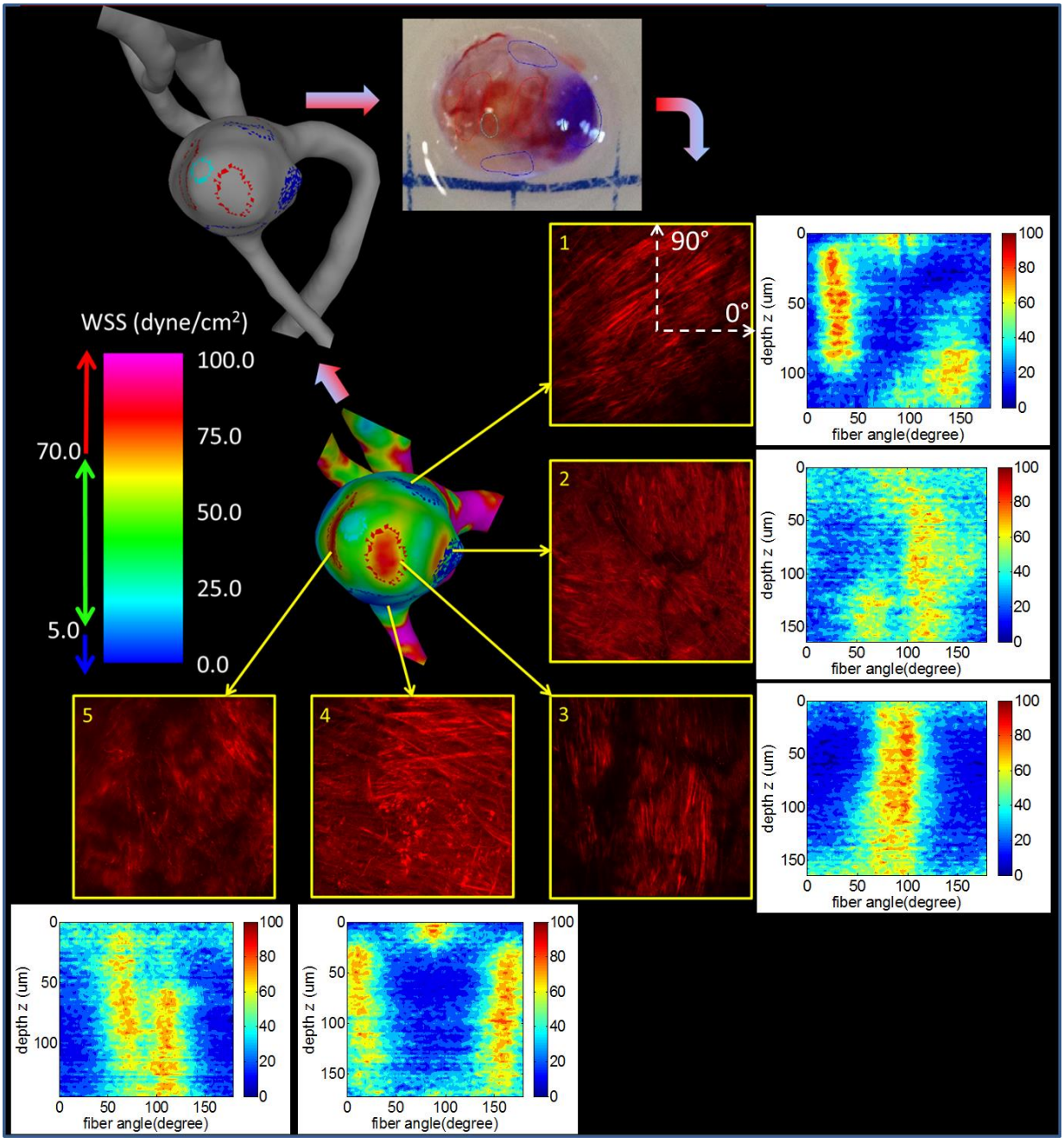

Figure 32. Projected stacks of MPM images of collagen fibers obtained in regions with different levels of WSS magnitude. Fiber orientation distribution through the wall thickness of corresponding MPM images was shown as contour plots.

presented as bar chart with maximum relative amplitude of 100%, and compared with the orientation distribution of collagen fiber at 11 regions, Figure 36. In most regions, it seem to suggest that the main collagen fiber direction is roughly normal to the mean WSS direction, while in region 7, region 8 and region 11, the main fiber direction seems to be aligned with the mean WSS direction.

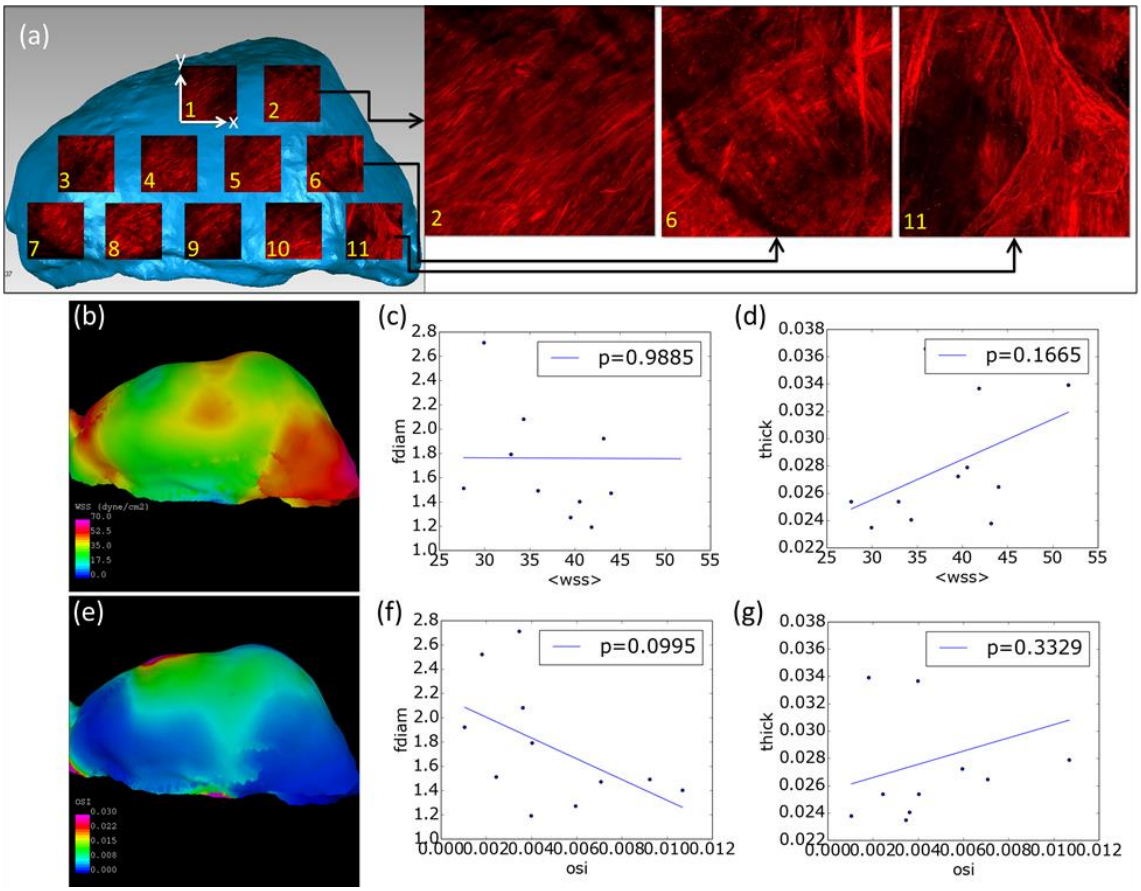

Figure 33. Local imaging of collagen fibers using MPM and comparison with local WSS and OSI: a) location of MPM imaging on micro-CT reconstruction of resected dome and details of fiber architecture at 3 locations with increasing WSS, b) interpolated WSS field, c) fiber diameter vs. <WSS>, d) wall thickness vs. <WSS>, e) interpolated OSI field, f) fiber diameter vs. OSI, and g) wall thickness vs. OSI.

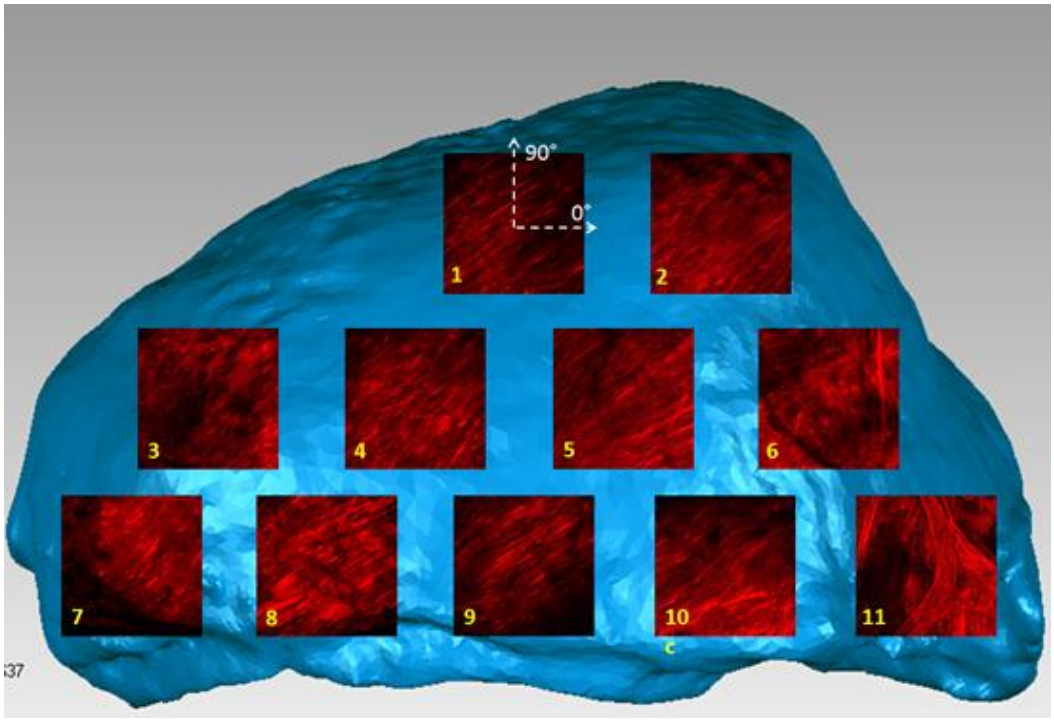

Figure 34. Local collagen fiber architecture on micro-CT reconstruction of resected dome. (11 sub-regions)**.**

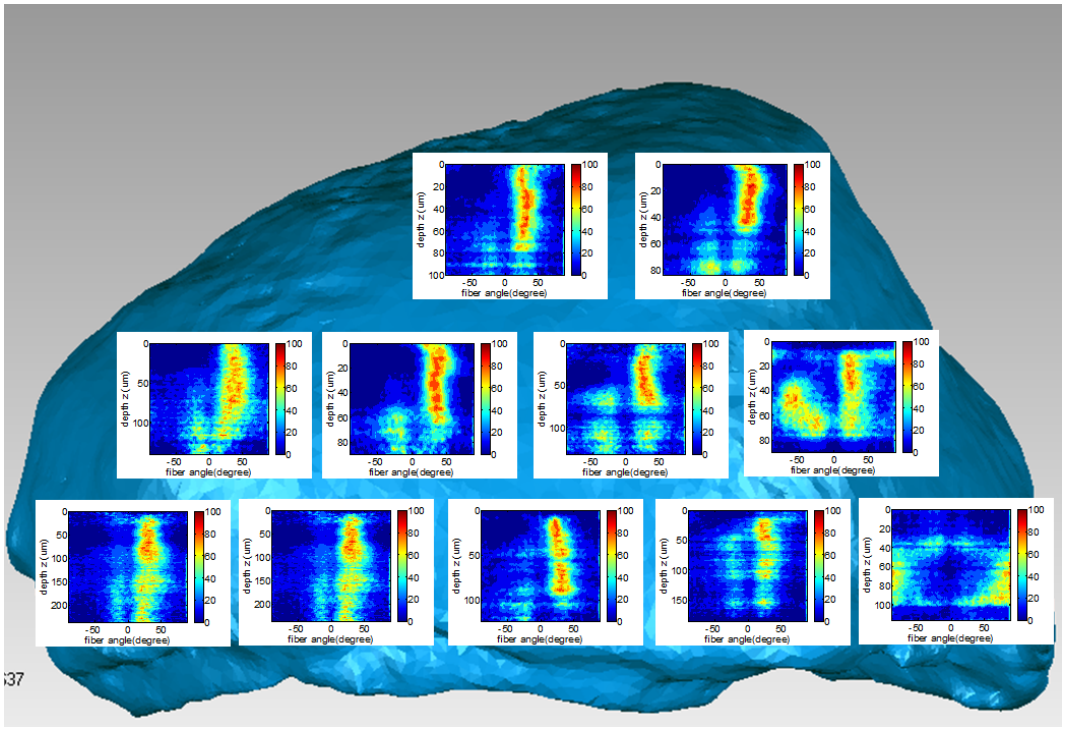

Figure 35. Local Fiber orientation distribution along the wall thickness of 11 MPM imaged regions.

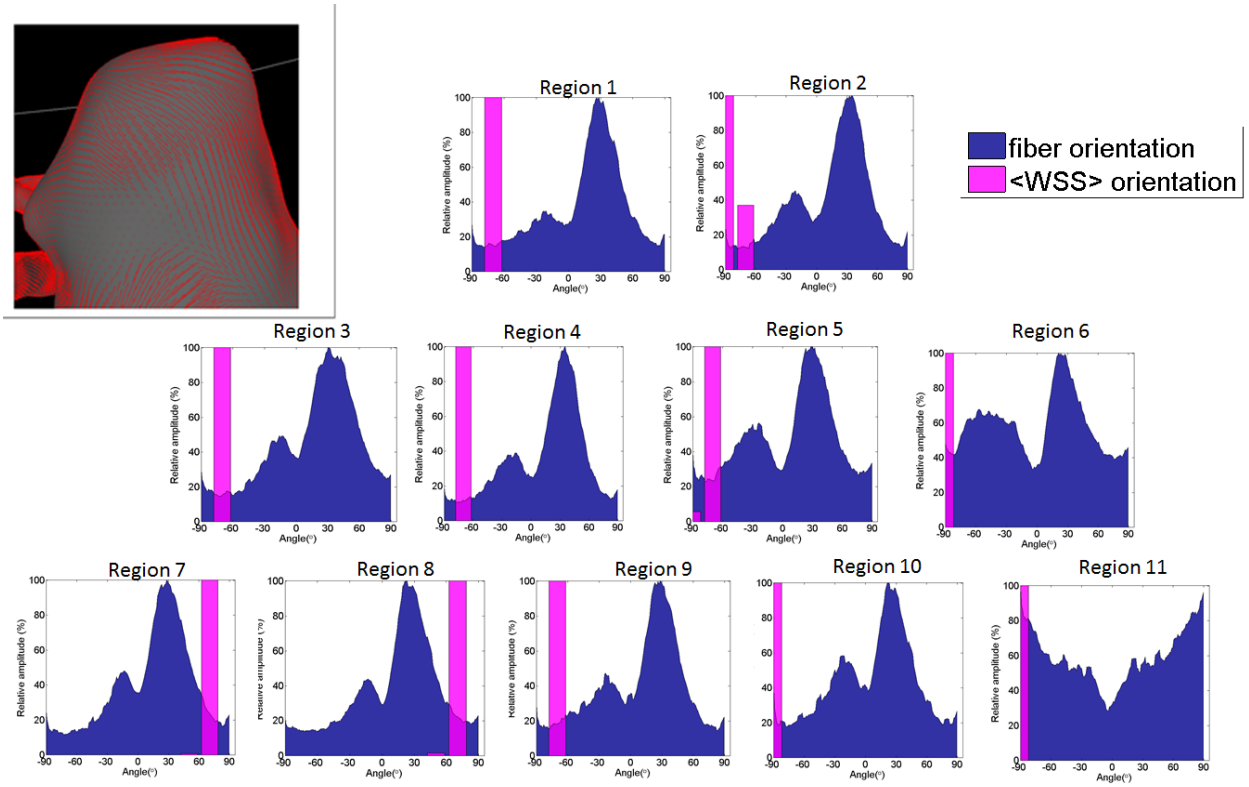

Figure 36. Distribution (histogram) of orientation of collagen fibers (blue) and mean wall shear stress vectors (<wss>, pink bars) for the 11 sub-regions regions shown in Figure 33 (a). The upper left image shows the mean WSS vector directions on the aneurysm sac

5.4 DISCUSSION

Information about the biological responses to hemodynamics loads that affect the structure of the aneurysm wall and consequently its mechanical behavior and strength is extremely important to advance our understanding of the processes governing aneurysm progression and eventual rupture.

Most previous approaches have studied global hemodynamics and/or wall characteristics, i.e. quantities that have been averaged over the aneurysm region [20]. However, both the

intrasaccular hemodynamic environment as well as the structural and mechanical properties of the wall can be heterogeneous, i.e. non uniform over the aneurysm region. Therefore, in order to understand the detailed mechanisms that drive the progressive degradation of the wall, it is important to investigate the relationships between the local hemodynamic characteristics and the local wall structure. This is a challenging problem not only because it requires collecting human aneurysm tissue samples and 3D images for study, but also because it requires mapping the resected samples back to the 3D anatomical models or images.

The current study is a first attempt at tackling this mapping problem. The methodology described in this paper enables the regional comparison of local hemodynamic (e.g. wall shear stress distribution) and wall characteristics (e.g. collagen architecture, wall thickness, cellular content, etc.). In particular, we focused on the relationship between flow induced wall shear stress and the collagen fiber architecture. Our results suggest that the structure of the collagen fibers may be different in region of the aneurysm dome subjected to different levels of wall shear stress. Specifically, we observed more disordered fiber architecture, with thicker, shorter fibers and gaps between fibers in regions of elevated WSS compared to a more organized structure in regions of normal or low WSS.

The current study has several limitations. First, the alignment of the micro-CT reconstruction of the resected dome and the 3D anatomical model is done visually. Although this may not be sufficient for a point-by-point comparison of the wall structure and local hemodynamics, it allows us to perform comparisons of quantities averaged over localized regions of the aneurysm wall. Secondly, artifacts in the shape obtained from micro-CT can affect the final alignment. For instance, the sample is not pressurized when imaged with micro-CT. Presumably, this would not be very important since, unlike the native artery, the aneurysm dome

has been found to have little if any elastic fibers, consistent with the greatly reduced toe region [62]. Additionally, the sample is fixed in solution, which helps keep the dome open and prevents folding of the walls. Thirdly, it may not be possible to obtain reliable alignments for some samples, for example if the dome is nearly spherical, or if the sample is very small, or if for clinical or geometrical reasons it is not possible to use the surgical pen to place marks that help orient the resected sample. Even when marking the sample is not possible, there may be other landmarks or geometrical features (such as blebs, calcifications, regions of high curvature, etc.) that can be used to orient and align the sample. Furthermore, an exact alignment may not be vital in many cases, for example, for aneurysms for which the hemodynamic and/or wall characteristics of interest are relatively uniform. In a larger study using this approach, we will assess the percentage of aneurysm domes that can be aligned with confidence.

Despite these limitations, the current study suggests that it is feasible to perform comparisons of local hemodynamics and wall properties in different regions of resected aneurysm domes. In particular, it is possible to connect the local hemodynamic conditions to the local collagen architecture, the local cellular content, and presumably the local mechanical properties. Thus, this strategy enables, for the first time, the direct study of the local mechano-biological mechanisms of intracranial aneurysms.

5.5 **CONCLUSIONS**

A methodology to identify corresponding regions in 3D image-based anatomical aneurysm models and micro-CT reconstruction of resected domes has been described. This approach

allows us, for the first time, to map the local hemodynamic characteristics to the local wall structure.

Our results support the idea that the local hemodynamic conditions, wall shear stress in particular, are related to the local structure of the wall, more specifically to the collagen fiber architecture. In particular, sparse, inhomogeneous fiber architectures suggestive of impaired remodeling are observed at regions of elevated wall shear stress. Further studies are needed to confirm these associations with more samples and understand the connections between hemodynamic loads, cellular contents and collagen architecture, and how the wall structure determines its mechanical behavior.

APPENDIX A

DERIVATION OF THE LAPLACE LAW

The equilibrium equation for spherical membranes loaded under uniform transmural pressure is

$$t\sigma = d\Delta P / 4 \tag{A1}$$

where t is the wall thickness at loaded state, σ is the Cauchy stress, d is the loaded diameter and ΔP is the transmural pressure, as shown in Figure 37. Assuming incompressibility, we have the relationship between the unloaded and loaded geometric parameters,

$$\frac{t_0}{t} = (\frac{d}{D})^2 \tag{A2}$$

Where t_0 is the unloaded wall thickness and D is the unloaded diameter.

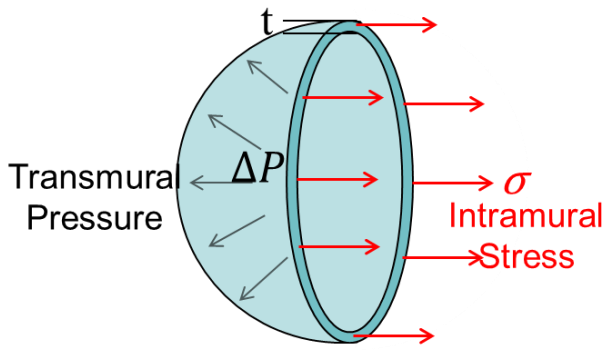

Figure 37. Balance between intramural stress and transmural pressure

Based on equations A1 and A2, we estimate the transmural pressure under which aneurysm would fail ΔP_f

$$\Delta P_f = 4\sigma_f \frac{t_0}{D}(\frac{D}{d})^3 \tag{A3}$$

which is exactly the equation 2 in Chapter 2.

APPENDIX B

HUMAN CEREBRAL ANEURYSM/ARTERY TISSUE IMMUNOHISTOCHEMICAL STAINING PROTOCOL

Fixation

1. Wash tissue 3 x in PBS
2. Fix in 2% paraformaldehyde in PBS at 4 °C for ~ 4 h

a. Overnight may also be acceptable. However, take care not to over-fix

b. Room temperature may also be acceptable. However, 4 °C is preferred

Protocol

1.) Obtain cryostat sections (~6 microns) and put onto glass slides. Some tissues (e.g. blood vessels, brain, fat) may require gelatin coated or poly-lysine coated slides to remain attached to the slide after multiple wash steps. An expensive, but good solution is to use Superfrost Plus Stain Slides (from, e.g., Fischer)

2.) Keep slides at –20oC until ready for use (see above).

3.) Rehydrate tissue sections with 2 washes of 1xPBS, keep in liquid at all times until sample has a gelvatol adhered cover glass

4.) Depending on your protein or cell type of interest, detergent permeabilization may be necessary (10 minutes with PBS + 0.1%Triton X-100).

5.) Block with 2% BSA for 45 minutes. Alternative blocks are using 20% serum in PBS+0.5% BSA (PBB) from the species in which your secondary antibodies are made (e.g. if you secondary antibody is made in goat, use 20% goat serum. Likewise if your secondary is made in donkey, use 20% donkey serum).

6.) Wash sections with 5 times with PBS+0.5% BSA (PBB).

7.) Primary antibody: Dilute to the desired concentration in PBB (vortex gently, spin down for 5 min at 10-12K RPM to get rid of aggregates). Primary antibodies should be 2 ug/mL or 4 ug/mL at final working concentration. Gently drop 70-100 µl antibody solution over the section (so the section is all covered). Incubate for 60 minutes. Longer primary antibody incubations may be necessary and must be determined empirically in your system. Initial antibody optimization should be accomplished in a range up to 5ug/ml antibody in PBB. If longer incubation times are necessary, place a piece of wet paper towel in your slide box (or chamber) with your samples to minimize evaporation of your primary antibody solution. In some cases overnight incubations at 4oC are necessary, you must put your samples in a humid environment (wet paper towel within slide box), avoid disturbing the sample volume on your section. Primary antibodies can be added together, but the host must be from 2 different species (unless the primary antibodies are directly conjugated with the fluorophore).

8.) Wash sections 5 times with PBB.

9.) Secondary antibody: Add secondary antibody to the section for 60 minutes (made in PBB, vortex, spin down at 10-12K RPM for 5 minutes to pellet any aggregates – very important). Secondary antibodies should be half of the primary antibody 1 ug/mL or 2ug/mL at final

working concentration. The secondary antibody step should be kept to within an hour. You may add fluor-conjugated phalloidin (for F-actin counterstain) or Draq5 (a far-red nuclear stain from Biostatus) to your secondary solution. Secondaries can be added together if using more than one, but they must be against two separate species.

10.) Wash sections with 5 times with PBB.

11.) Wash sections with 5 times with PBS to remove the BSA that would bind Hoechst indiscriminately.

12.) Add Hoechst stain 30 seconds to stain the nuclei (Hoechst stain=1 mg/100 ml dH2O, Sigma CatNo.B-2883). (Caution! This substance is carcinogenic and toxic to skin.)

13.) Wash sections 3 times with PBS.

14.) Adhere cover glass over your sample with gelvatol, place slides horizontal in slide box, and allow cover glass to adhere to slide overnight at 4oC in the dark. Gelvatol is water soluble, if needed coverslip may be gently removed by submerging sample in water and allowing coverslip to lift without resistance from the slide.

In some cases non-fixed tissue is used for frozen sectioning. After sectioning, tissue can be fixed in 2% Paraformaldehyde in PBS for 30 min-1 hr.

Primary antibodies used in immunohistochemical staining are listed in the following table.

Table 10. Primary antibodies used in chapter 3

antibody	Product code	size	Dilusion	Vendor
Anti-Collagen I antibody	ab34710	100 µg	1:50	abcam
Anti-Collagen III antibody	ab7778	100 µg	1:50	abcam
Anti-alpha smooth muscle Actin antibody [1A4]	ab7817	500 µl	1:100	abcam

APPENDIX C

MATLAB PROGRAMS FOR 3D COLLAGEN FIBER ORIENTATION ANALYSIS

Sub_projection.m a program for superimposing subset of 2D images into grayscale images

```
clear all
clc
close all
n=55 % number of total images
image=zeros(1024,1024,5);
for z=1:n-4
for i=1:5
filename=sprintf(file_name%3.3d.tif',z+i-1); %read file name
im=imread(filename);
im=im(:,:,1);
image(:,:,i)=im;
end
project=max(image,[],3);
I = mat2gray(project, [0 255]);
```

```
imwrite(I,['subproject',num2str(z),'.tif']); % save projected image as grayscale .tif image file
end
```

Orientation_Analysis_3D.m a program for analyzing fiber orientation in 2D image stacks and generating fiber orientation distribution through the wall thickness. A matlab program "Courtney.m" for analyzing the fiber orientiaon in 2D image developed by Dr. Hill was modified to achieve analysis in 3D [93].

```
clear all;
close all
clc
numb=187; % number of images
toln=0.0044; % Enter tolerance for angles
% File input
imgsiz=1024;
[file,path]=uigetfile('*.tif','Select image file');
img0=imread([path file]);
disp('Select 3 points on the image to average for background')
figure(1)
imshow(img0)
hold on; axis image;
hold off;
% Use ginput to select n points for setting lower threshold level
n=3; % number of points to average for threshold
```

```
[x y] = ginput(n); % note y = row, x = column
x=uint32(x);y=uint32(y); % Convert x and y to integers
img0=double(img0);
upthsh=0;
lowths=0;
i=0;
for i=1:n
lowths=lowths+img0(y(i),x(i));
end
% upthsh=upthsh/3
lowths=lowths/n;

for z=1:numb
   filename=sprintf('subproject%d.tif',z);
   img=imread(filename);
img=double(img); % convert array values from uint8 to double precision
% Find size of image
M=length(img(:,1));
N=length(img(1,:));
clear i j
for i=1:M; % iterate across rows
for j=1:N; % iterate across columns
if img(i,j) <= lowths;
```

```
img(i,j)=0;
end
end
end
% Edge detection
% disp('Enter a value for mask size, 3 works quite well')
% s=input('Enter mask size ');
s=3;
l=2*s+1;
sig=2.0;
clear i j
for i=-s:1:s;
for j=-s:1:s;
hy(i+s+1,j+s+1)=(2*i/sig^2)*exp(-(i^2+j^2)/sig^2);
hx(i+s+1,j+s+1)=(2*j/sig^2)*exp(-(i^2+j^2)/sig^2);
end
end
clear i j
for i=1:M-l+1; % iterate across rows
for j=1:N-l+1; % iterate across columns
gx=0;
gy=0;
for p=1:l; % iterate across rows of kernel over current pixel
```

```
for q=1:l; % iterate across cols of kernel over current pixel
gy=gy+hy(p,q)*img(i-1+p,j-1+q);
gx=gx+hx(p,q)*img(i-1+p,j-1+q);
end
end
Gx(i,j)=gx;
Gy(i,j)=gy;
G(i,j)=(gx^2+gy^2);
if (gx<=0)&&(gy<=0);
phi(i,j)=2;
else
if gx <= 0;
phi(i,j)=2;
else
phi(i,j)=atan(gy/gx);
end
end
end
countdown1=M+1-l-i;
end
t=15;
% typically t=12
k=0;
```

```
i=0;
j=0;
row=0;
for i=1:t:M-l+1;
row=row+1;
col=0;
for j=1:t:N-l+1;
col=col+1;
clear A

if (M-t-i >=t)&&(N-t-j >=t)
theta=0;
k=0;
index=0;
for theta=0:1:179
k=k+1;
radian=theta*pi()/180;
p=0;
q=0;
a=0;
sum=0;
% iterate across subregion
for p=1:t;
```

```
for q=1:t;
if phi(i-1+p,j-1+q)==2;
a=a+0;
else
a=a+G(i-1+p,j-1+q)*(cos(radian-phi(i-1+p,j-1+q)))^2;
end
end
end
A(k)=a; % accumulator bin sum across subregion
end
index=0;
if max(A) <= 0;
maxang(row,col)=200;
else
[y,index]=max(A);
maxang(row,col)=index-1;
end


end
end
countdown2=M+1-l-i;
end
```

```
% Normalize G for image
G=(G./max(max(G))).*255;
G=uint8(G);G=double(G);
% Take natural logarithm of G
clear i j
for i=1:length(G(:,1));
for j=1:length(G(1,:));
if G(i,j)<=0;
Glog(i,j)=0;
else
Glog(i,j)=log(G(i,j));
end
countdown3=length(G(:,1))-i;
end
end
clear x y u v
mag=20;
i=0;
j=0;
n=0;
row=0;
for i=1:t:M-l+1;
```

```
row=row+1;
col=0;
for j=1:t:N-l+1;
col=col+1;
if (M-t-i >=t)&&(N-t-j >=t)
n=n+1;
x(n)=(j+(t/2)-1)+(s+1);
y(n)=(i+(t/2)-1)+(s+1);
if maxang(row,col)==200;
u(n)=0;
v(n)=0;
else
u(n)=mag*sin(maxang(row,col)*pi()/180);
v(n)=-mag*cos(maxang(row,col)*pi()/180);
end
end
end
countdown4=M-l+1-i;
end
clear p
n=0;
for p=0:1:179;
n=n+1;
```

```
abscis(n)=p;
clear i j
ord=0;
for i=1:length(maxang(1,:));
for j=1:length(maxang(:,1));
if maxang(j,i) < 200;
if abs(p-maxang(j,i)) < toln
ord=ord+1;
end
end
end
end
ordina(n)=ord;
anglei(n)=-n+90;
countdown4=179-p;
end
% img=uint8(img);
% G=uint8(G);
ordina=fliplr(ordina);
Ism(:,z)=ordina';
z
end
xlswrite('Orientation_distribution_region.xlsx',Ism); % save data in an excel spreadsheet
```

APPENDIX D

SENSITIVITY STUDY OF ANEURYSM FINITE ELEMENT MODELS

The effect of element size on the maximum von Mises stress on the dome of aneurysm at 300 mmHg transmural pressure was studied by performing a finite element stress analysis using models with various element sizes. As shown in Table 11. Element size of 0.2 mm has been chosen for the final analysis in Chapter 3, in which the maximum stress does not change to the third decimal place with further mesh refinement to 0.1 mm.

Table 11. List of maximum von Mises Stress on the dome of CA-26 from FEA models with element size from 0.1 mm to 0.5 mm. Second column: the corresponding total element numbers of models with different element sizes.

Element Size (mm)	Total Element Number	Max von Mises Stress(MPa)
0.1	12318	0.403
0.2	3882	0.403
0.3	1608	0.403
0.4	873	0.383
0.5	804	0.391

To investigate the effect of parent vascular on the stress distribution at the dome of aneurysm (away from aneurysm neck), finite element models with and without parent vascular were compared. The stress distribution in those two models is shown in Figure 38. The maximum von Mises stress are 0.3999 MPa and 0.4007 MPa for model with and without parent vascular, respectively. The small difference in Max stress (0.2% difference) of those two models suggests that the parent vascular can be excluded from the model without compromising the stress estimation.

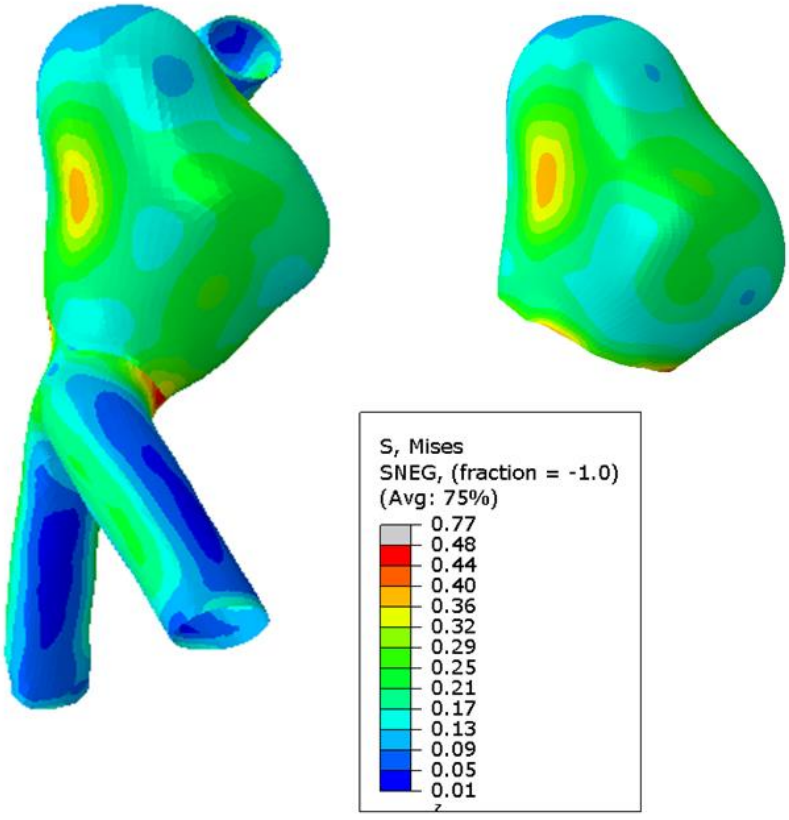

Figure 38. Stress distribution at 300 mmHg, with and without parent vascular. Stress unit: MPa

APPENDIX E

HEMODYNAMIC CHARACTERISTICS OF HUMAN ANEURYSMS

Hemodynamic characteristics, including aneurysmal inflow, streamlines, WSS and vortex corelines of 8 aneurysms were investigated in Chapter 4. However, hemodynamics of only two examples, CA-15 and CA-26 were presented in Figure 25. Other cases, including CA-01, CA-11, CA-12, CA-25, CA-39 and CA-46 are shown in the following figure. This part of work has been done by Dr. Cebral's group at George Mason University.

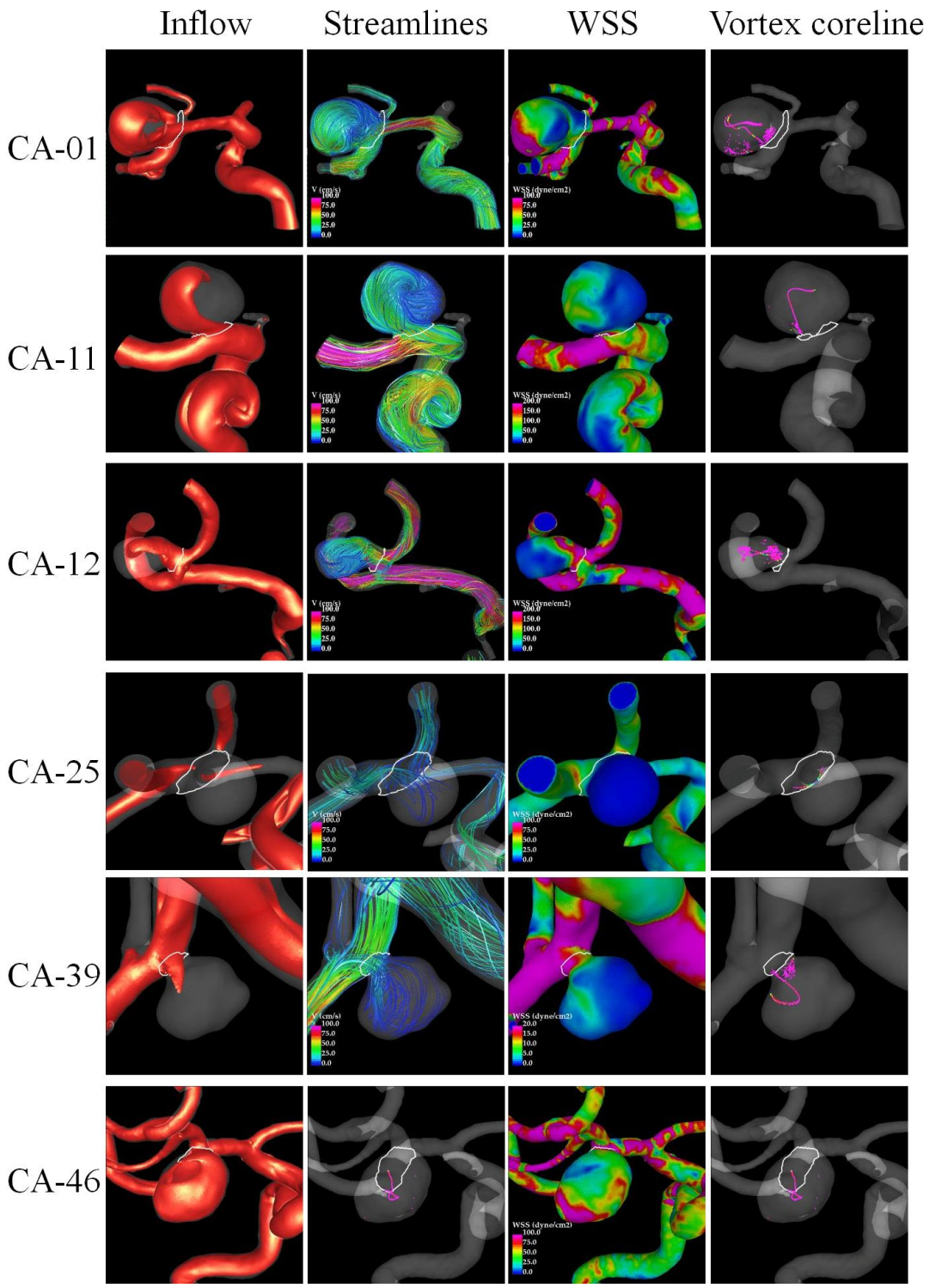

Figure 39. Aneurysmal inflow, stream lines, WSS and vortex corelines at the peak systole of 6 human aneurysms.

APPENDIX F

FIBER DIAMETER MEASUREMENT

In order to quantify the collagen fiber structure in cerebral aneurysms, fiber diameter measurement has been done in Chapter 2. Instructions for fiber diameter measurement are:

1. Superimpose a stack of multiple MPM images into 2D image in ImageJ. (image->stacks->zproject->Max intensity)
2. Place 25 points (5 x 5 matrix) on the image using the following custom matlab program.

```
clear all
clear
clc

convrt=0.5;
len=3;
thick=3;
[file,path]=uigetfile('*.tif','Select image file');
img=imread([path file]);


% Get image info
% imginf=imfinfo([path file])

for i=1:5
for j=1:5
   clear x;
   clear y;
x=(1024*i)/6;
```

```
y=(1024*j)/6;
x=uint32(x);
y=uint32(y); % Convert x and y to real

% red=img(y,x,1)
% green=img(y,x,2)
% blue=img(y,x,3)


ylim=double(uint32(thick));
xlim=double(uint32(len));
for k=x:x+xlim
   for l=y:y+ylim
      k=uint32(k);
      l=uint32(l);
      img(k,l,1)=255;
      img(k,l,2)=255;
      img(k,l,3)=255;
   end
end
end
end

figure(2); imshow(img)
% imwrite(img,[file],'tiff')
imwrite(img,[file(1:length(file)-4) 'dots_on_image.tif'],'tiff')
```

3. Randomly select 15 out of the 25 points on the image.

```
clear all; % This Matlab program is a random number generator.
clc;
rng shuffle; %different seed set every time MATLAB program is run.

for i=1:9
   y=randperm(25,15);
   for j=1:15
      x(i,j)=y(j);
   end
end
```

```
filename='Measurement_Points.xlsx';
xlswrite(filename,x);
close all;
```

4. Find the nearest fiber to the selected point. In cases were fibers were banded, diameters of individual fibers were used.
5. Measure the fiber diameter in ImageJ using straight line function. Press Ctrl+M to get the automatic length measurement. The measured value could be number of pixels. If so, convert it to length in um.
6. Repeat the fiber diameter measurement at other 14 selected locations.

BIBLIOGRAPHY

[1] Brisman, J. L., Song, J. K., & Newell, D. W. (2006). Cerebral aneurysms. New England Journal of Medicine, 355(9), 928-939.

[2] Stehbens, W. E. Pathology of the Cerebral Blood Vessels. St. Louis: C.V. Mosby Co., 1972.

[3] Rinkel, G., M. Djibuti, A. Agra, and J. V. Gijn. Prevalence and risk of rupture of intracranial aneurysms: a systematic review. Stroke 29:251–256, 1998.

[4] Wiebers, D. O., J. C. Torner, and I. Meissner. Impact of unruptured intracranial aneurysms on public health in the United States. Stroke 23:1416–1419, 1992.

[5] Schievink, W. I. (1997). Intracranial aneurysms. New England Journal of Medicine, 336(1), 28-40.

[6] Kelly, P. J., Stein, J., Shafqat, S., Eskey, C., Doherty, D., Chang, Y., ... & Furie, K. L. (2001). Functional recovery after rehabilitation for cerebellar stroke. Stroke, 32(2), 530-534.

[7] Ropper, A. H., & Zervas, N. T. (1984). Outcome 1 year after SAH from cerebral aneurysm: management morbidity, mortality, and functional status in 112 consecutive good-risk patients. Journal of neurosurgery, 60(5), 909-915.

[8] van Gijn, J., & Rinkel, G. J. E. (2001). Subarachnoid haemorrhage: diagnosis, causes and management. Brain, 124(2), 249-278.

[9] Inghall, T.J. and Whisnant J.P.. Subarachnoid hemorrhage. In Epidemiology of Subarachnoid Haemorrhage, pages 63–78. Marcel-Dekker, 1998.

[10] The International Study of Unruptured Intracranial Aneurysms Investigators (1998) Unruptured Intracranial Aneurysms–Risk of Rupture and Risks of Surgical Intervention. N Engl J Med 339(24):1725–33.

[11] Broderick, J. P., Brown, R. D., Sauerbeck, L., Hornung, R., Huston, J., Woo, D., ... & Connolly, E. S. (2009). Greater rupture risk for familial as compared to sporadic unruptured intracranial aneurysms. Stroke 40(6):1952–1957

[12] Wiebers, D. O., & International Study of Unruptured Intracranial Aneurysms Investigators. (2003). Unruptured intracranial aneurysms: natural history, clinical outcome, and risks of surgical and endovascular treatment. The Lancet,362(9378), 103-110.

[13] Lall, R. R., Eddleman, C. S., Bendok, B. R., & Batjer, H. H. (2009). Unruptured intracranial aneurysms and the assessment of rupture risk based on anatomical and morphological factors: sifting through the sands of data. Neurosurg Focus 26(5):E2

[14] Ujiie, H., Tamano, Y., Sasaki, K., & Hori, T. (2001). Is the aspect ratio a reliable index for predicting the rupture of a saccular aneurysm?. Neurosurgery, 48(3), 495-503.

[15] Xiang, J., Natarajan, S. K., Tremmel, M., Ma, D., Mocco, J., Hopkins, L. N., ... & Meng, H. (2011). Hemodynamic–morphologic discriminants for intracranial aneurysm rupture. Stroke, 42(1), 144-152.

[16] Ishibashi, T., Murayama, Y., Urashima, M., Saguchi, T., Ebara, M., Arakawa, H., ... & Abe, T. (2009). Unruptured intracranial aneurysms incidence of rupture and risk factors. Stroke, 40(1), 313-316.

[17] Juvela, S., Porras, M., & Poussa, K. (2000). Natural history of unruptured intracranial aneurysms: probability of and risk factors for aneurysm rupture.Journal of neurosurgery, 93(3), 379-387.

[18] Utter, B., & Rossmann, J. S. (2007). Numerical simulation of saccular aneurysm hemodynamics: influence of morphology on rupture risk. Journal of biomechanics, 40(12), 2716-2722.

[19] Weir, B., Macdonald, R. (1996). Neurosurgery, McGraw-Hill, Intracranial aneurysms and hemorrhage: An overview, 2191–2213.

[20] Cebral, J. R., & Raschi, M. (2013). Suggested connections between risk factors of intracranial aneurysms: A review. Ann Biomed Eng 41(7):1366–1383.

[21] Frösen, J., Piippo, A., Paetau, A., Kangasniemi, M., Niemelä, M., Hernesniemi, J., Jääskeläinen, J. (2004). Remodeling of saccular cerebral artery aneurysm wall is associated with rupture: histological analysis of 24 unruptured and 42 ruptured cases. Stroke 35(10):2287–93

[22] Humphrey, J. D., Canham, P. B. (2000). Structure, mechanical properties, and mechanics of intracranial saccular aneurysms. J Elasticity 61(1-3):49-81.

[23] Cebral, J.R., et al., Association of hemodynamic characteristics and cerebral aneurysm rupture. AJNR. American journal of neuroradiology. 2011. 32(2): p. 264-70.

[24] Cebral, J. R., Mut, F., Sforza, D., Löhner, R., Scrivano, E., Lylyk, P., & Putman, C. (2011). Clinical Application of Image-Based CFD for Cerebral Aneurysms. International Journal for Numerical Methods in Biomedical Engineering, 2011. 27(7): p. 977-992.

[25] Boussel, L., Rayz, V., Martin, A., Acevedo, Bolton, G., Lawton, M. T., Higashida, R., ... & Saloner, D. (2009). Phase contrast magnetic resonance imaging measurements in intracranial aneurysms in vivo of flow patterns, velocity fields, and wall shear stress: Comparison with computational fluid dynamics. Magnetic Resonance in Medicine, 61(2), 409-417.

[26] Castro, M. A., Putman, C. M., Sheridan, M. J., & Cebral, J. R. (2009). Hemodynamic patterns of anterior communicating artery aneurysms: a possible association with rupture. American journal of neuroradiology, 30(2), 297-302.

[27] Cebral, J. R., Castro, M. A., Burgess, J. E., Pergolizzi, R. S., Sheridan, M. J., and Putman, C. M., 2005, Characterization of Cerebral Aneurysms for Assessing Risk of Rupture By Using Patient-Specific Computational Hemodynamics Models. AJNR. Am J Neuroradiology, 26(10), pp. 2550-2559.

[28] Steinman, D. A., Milner, J. S., Norley, C. J., Lownie, S. P., & Holdsworth, D. W. (2003). Image-based computational simulation of flow dynamics in a giant intracranial aneurysm. American Journal of Neuroradiology, 24(4), 559-566.

[29] Jou, L. D., Lee, D. H., Morsi, H., & Mawad, M. E. (2008). Wall shear stress on ruptured and unruptured intracranial aneurysms at the internal carotid artery. American Journal of Neuroradiology, 29(9), 1761-1767.

[30] Robertson, A. M., Watton, P. N. (2012). Computational fluid dynamics in aneurysm research: critical reflections, future directions. AJNR Am J Neuroradiol 33(6):992–995

[31] Byrne, G., Mut, F., & Cebral, J. (2014). Quantifying the large-scale hemodynamics of intracranial aneurysms. American Journal of Neuroradiology, 35(2), 333-338.

[32] Scott, S., Ferguson, G. G., & Roach, M. R. (1972). Comparison of the elastic properties of human intracranial arteries and aneurysms. Canadian Journal of Physiology and Pharmacology, 50, 328–332. doi:10.1139/y72-049

[33] Steiger, H. J., Aaslid, R., Keller, S., Reulen, H. J. (1989). Strength, elasticity and viscoelastic properties of cerebral aneurysms. Heart Vessels 5(1):41–46

[34] Toth, B. K., Nasztanovics, F., & Bojtar, I. (2007). Laboratory tests for strength paramaters of brain aneurysms. Acta of Bioengineering and Biomechanics, 9(2), 3.

[35] MacDougall, J. D., Tuxen, D., Sale, D. G., Moroz, J. R., & Sutton, J. R. (1985). Arterial blood pressure response to heavy resistance exercise. Journal of Applied Physiology (Bethesda, Md. : 1985), 58, 785–790.

[36] Heber, M. E., Raftery, E. B., & Thompson, D. (1988). Intra-arterial ambulatory blood pressure monitoring can save your life—or, acute haemodynamic response to a murderous assault. International journal of cardiology, 20(1), 138-141.

[37] Mitchell, P., Birchall, D., & Mendelow, A. D. (2006). Blood pressure, fatigue, and the pathogenesis of aneurysmal subarachnoid hemorrhage. Surgical neurology, 66(6), 574-580.

[38] Schievink, W. I., Karemaker, J. M., Hageman, L. M., & van der Werf, D. J. (1989). Circumstances surrounding aneurysmal subarachnoid hemorrhage. Surgical neurology, 32(4), 266-272.

[39] Vlak, M. H., Algra, A., Brandenburg, R., & Rinkel, G. J. (2011). Prevalence of unruptured intracranial aneurysms, with emphasis on sex, age, comorbidity, country, and time period: a systematic review and meta-analysis. The Lancet Neurology, 10(7), 626-636.

[40] Isaksen, J. G., Bazilevs, Y., Kvamsdal, T., Zhang, Y., Kaspersen, J. H., Waterloo, K., ... & Ingebrigtsen, T. (2008). Determination of wall tension in cerebral artery aneurysms by numerical simulation. Stroke, 39(12), 3172-3178.

[41] Sanchez, M., Ambard, D., Costalat, V., Mendez, S., Jourdan, F., Nicoud, F. (2013). Biomechanical assessment of the individual risk of rupture of cerebral aneurysms: A proof of concept. Ann Biomed Eng 41(1):28–40.

[42] Geest, J. P. V., Wang, D. H., Wisniewski, S. R., Makaroun, M. S., & Vorp, D. A. (2006). Towards a noninvasive method for determination of patient-specific wall strength distribution in abdominal aortic aneurysms. Annals of biomedical engineering, 34(7), 1098-1106.

[43] Raghavan, M. L., Vorp, D. A., Federle, M. P., Makaroun, M. S., & Webster, M. W. (2000). Wall stress distribution on three-dimensionally reconstructed models of human abdominal aortic aneurysm. Journal of Vascular Surgery, 31(4), 760-769.

[44] Cebral, J. R., Mut, F., Weir, J., Putman, C. (2011). Quantitative characterization of the hemodynamic environment in ruptured and unruptured brain aneurysms. AJNR Am J Neuroradiol 32(1):145–51

[45] Hill, M. R., Duan, X., Gibson, G. A., Watkins, S., & Robertson, A. M. (2012). A theoretical and non-destructive experimental approach for direct inclusion of measured

collagen orientation and recruitment into mechanical models of the artery wall. Journal of biomechanics, 45(5), 762-771.

[46] Robertson, A. M., Hill, M. R., Li, D. Structurally motivated damage models for arterial walls—theory and application. In: Modelling of Physiological Flows, Modeling, Simulation and Applications, Vol. 5, edited by D. Ambrosi, A. Quarteroni, and G. Rozza. New York: Springer, 2011.

[47] Canham, P. B., & Ferguson, G. G. (1985). A Mathematical Model For the Mechanics Of Saccular Aneurysms. J. Neurosurger 17, 291–295.

[48] Robertson, A. M., and Watton, P. N. Mechanobiology of the arterial wall, chap 8. In: Transport in Biological Media, edited by S. Becker, and A. Kuznetsov. New York: Elsevier, 2013, pp. 275–347.

[49] Austin, G., Fisher, S., Dickson, D., Anderson, D., Richardson, S. (1993). The Significance of the Extracellular Matrix in Intracranial Aneurysms. Ann Clin Lab Sci 23(2):97–105

[50] Stehbens, W. E. (1972). Pathology of the Cerebral Blood Vessels. C.V. Mosby Co.

[51] Haykowsky, M. J., Findlay, J. M., & Ignaszewski, A. P. (1996). Aneurysmal subarachnoid hemorrhage associated with weight training: three case reports. Clin J Sport Med, 6(1), 52–55.

[52] Schievink, W. I., Karemaker, J. M., Hageman, L.M., van der Werf, D. J. (1989). Circumstances surrounding aneurysmal subarachnoid hemorrhage. Surgical Neurology 32(4):266–272

[53] Schmid, H., Watton, P. N., Maurer, M. M., Wimmer, J., Winkler, P., Wang, Y. K., Röhrle, O., Itskov, M. (2010). Impact of transmural heterogeneities on arterial adaptation: application to aneurysm formation. Biomech Model Mechan 9(3):295–315.

[54] Costalat, V., Sanchez, M., Ambard, D., Thines, L., Lonjon, N., Nicoud, F., ... & Jourdan, F. (2011). Biomechanical wall properties of human intracranial aneurysms resected following surgical clipping (IRRAs Project). Journal of biomechanics, 44(15), 2685-2691.

[55] Stemper, B. D., Yoganandan, N., Stineman, M. R., Gennarelli, T. A., Baisden, J. L., & Pintar, F. A. (2007). Mechanics of fresh, refrigerated, and frozen arterial tissue. Journal of Surgical Research, 139(2), 236-242.

[56] Frösen, J., Tulamo, R., Paetau, A., Laaksamo, E., Korja, M., Laakso, A., Niemelä, M., Hernesniemi, J. (2012). Saccular intracranial aneurysm: pathology and mechanisms. Acta Neuropathologica 123(6):773–786.

[57] Kadirvel, R., Ding, Y. H., Dai, D., Zakaria, H., Robertson, A., Danielson, M., Lewis, D., Cloft, H., Kallmes, D. (2007). The influence of hemodynamic forces on biomarkers in the walls of elastase-induced aneurysms in rabbits. Neuroradiology 49(12):1041–1053.

[58] Krings, T., Mandell, D. M., Kiehl, T.R., Geibprasert, S., Tymianski, M., Alvarez, H., TerBrugge, K.G., Hans, F. J. (2011). Intracranial aneurysms: from vessel wall pathology to therapeutic approach. Nat Rev Neurology 7(10):547–59.

[59] Stehbens, W. E. (1989). Etiology of intracranial berry aneurysms. J Neurosurger 70(6):823 –831.

[60] Kallmes, D. F. (2012). Point: CFD–computational fluid dynamics or con- founding factor dissemination. AJNR Am J Neuroradiol 33(3):395–6

[61] Cebral, J. R., Meng, H. (2012). Counterpoint: realizing the clinical utility of computational fluid dynamics–Closing the gap. AJNR Am J Neuroradiol 33(3):396–8

[62] Robertson, A. M., Duan, X., Aziz, K. M., Hill, M. R., Watkins, S. C., & Cebral, J. R. (2015). Diversity in the strength and structure of unruptured cerebral aneurysms. Annals of biomedical engineering, 1-14.

[63] Humphrey, J.D. and P.B. Canham, Structure, Mechanical Properties, and Mechanics of Intracranial Saccular Aneurysms. Journal of Elasticity, 2000. 61(1): p. 49-81.

[64] Sforza, D., C.M. Putman, and J.R. Cebral, Hemodynamics of Cerebral Aneurysms. Ann Rev Fluid Mechanics, 2009. 41: p. 91-107.

[65] Cebral, J. R., Vazquez, M., Sforza, D. M., Houzeaux, G., Tateshima, S., Scrivano, E., ...& Putman, C. M. (2014). Analysis of hemodynamics and wall mechanics at sites of cerebral aneurysm rupture. Journal of neurointerventional surgery, neurintsurg-2014.

[66] Schriefl, A.J., A.J. Reinisch, S. Sankaran, D.M. Pierce, and G.A. Holzapfel, Quantitative assessment of collagen fibre orientations from two-dimensional images of soft biological tissues. J R Soc Interface, 2012. 9(76): p. 3081-93.

[67] Castro, M. A., Olivares, M. C. A., Putman, C. M., & Cebral, J. R. (2013, December). Wall motion and hemodynamics in intracranial aneurysms. InJournal of Physics: Conference Series (Vol. 477, No. 1, p. 012004). IOP Publishing.

[68] Dempere-Marco, L., Oubel, E., Castro, M., Putman, C., Frangi, A., & Cebral, J. (2006). CFD analysis incorporating the influence of wall motion: application to intracranial

aneurysms. In Medical Image Computing and Computer-Assisted Intervention–MICCAI 2006 (pp. 438-445). Springer Berlin Heidelberg.

[69] Sarrami-Foroushani, A., M.C. Villa-Uriol, M. Nasr Esfahany, S.C. Coley, L.Y. Di Marco, A.F. Frangi, and A. Marzo, Modeling of the acute effects of primary hypertension and hypotension on the hemodynamics of intracranial aneurysms. Ann Biomed Eng, 2015. 43(1): p. 207-21.

[70] Malek, A.M., S.L. Alper, and S. Izumo, Hemodynamic shear stress and its role in atherosclerosis. JAMA, 1999. 282(21): p. 2035-42.

[71] Taylor, C. L., Yuan, Z., Selman, W. R., Ratcheson, R. A., & Rimm, A. A. (1995). Cerebral arterial aneurysm formation and rupture in 20,767 elderly patients: hypertension and other risk factors. Journal of neurosurgery, 83(5), 812-819.

[72] Duan, X., Chung, B.J., Cebral, J.R., Aziz,K., Robertson, A.M.. Effective Remodeling in Cerebral Aneurysm: a Case Study. 2015 Summer Biomechanics, Bioengineering and Biotransport Conference (SB3C 2015).

[73] Wulandana, R., & Robertson, A. M. (2005). An inelastic multi-mechanism constitutive equation for cerebral arterial tissue. Biomechanics and Modeling in Mechanobiology, 4(4), 235-248.

[74] Ma, B., Lu, J., Harbaugh, R. E., & Raghavan, M. L. (2007). Nonlinear anisotropic stress analysis of anatomically realistic cerebral aneurysms. Journal of biomechanical engineering, 129(1), 88-96.

[75] MacDonald, D. J., Finlay, H. M., & Canham, P. B. (2000). Directional wall strength in saccular brain aneurysms from polarized light microscopy. Annals of biomedical engineering, 28(5), 533-542.

[76] Mimata, C., Kitaoka, M., Nagahiro, S., Iyama, K. I., Hori, H., Yoshioka, H., & Ushio, Y. (1997). Differential distribution and expressions of collagens in the cerebral aneurysmal wall. Acta neuropathologica, 94(3), 197-206.

[77] Samuel, A., & Weir, J. Introduction to Engineering Design: Modelling, Synthesis and Problem Solving Strategies, 1999. 1-5.

[78] Humphrey, J. D., & Holzapfel, G. A. (2012). Mechanics, mechanobiology, and modeling of human abdominal aorta and aneurysms. Journal of biomechanics, 45(5), 805-814.

[79] Fillinger, M. F., Raghavan, M. L., Marra, S. P., Cronenwett, J. L., & Kennedy, F. E. (2002). In vivo analysis of mechanical wall stress and abdominal aortic aneurysm rupture risk. Journal of vascular surgery, 36(3), 589-597. Fillinger, M. F., Raghavan, M. L., Marra, S. P., Cronenwett, J. L., & Kennedy, F. E. (2002). In vivo analysis of mechanical

wall stress and abdominal aortic aneurysm rupture risk. Journal of vascular surgery, 36(3), 589-597.

[80] Stenmark, K. R., Yeager, M. E., El Kasmi, K. C., Nozik-Grayck, E., Gerasimovskaya, E. V., Li, M., ... & Frid, M. G. (2013). The adventitia: essential regulator of vascular wall structure and function. Annual review of physiology, 75, 23.

[81] Hu, Y., & Xu, Q. (2011). Adventitial Biology Differentiation and Function. Arteriosclerosis, Thrombosis, and Vascular Biology, 31(7), 1523-1529.

[82] Shojima, M., Oshima, M., Takagi, K., Torii, R., Hayakawa, M., Katada, K., Morita, A., and Kirino, T., (2004), Magnitude and role of wall shear stress on cerebral aneurysm: computational fluid dynamic study of 20 middle cerebral artery aneurysms," Stroke, 35(11), pp. 2500-2505.

[83] Karmonik, C., Yen, C., Diaz, O., Klucznik, R., Grossman, R. G., and Benndorf, G., "Temporal variations of wall shear stress parameters in intracranial aneurysms-importance of patient-specific inflow waveforms for CFD calculations," Acta Neurochir (Wien).

[84] Hassan, T., Timofeev, E. V., Saito, T., Shimizu, H., Ezura, M., Matsumoto, Y., Takayama, K., Tominaga, T., and Takahashi, A., 2005, A proposed parent vessel geometry-based categorization of saccular intracranial aneurysms: computational flow dynamics analysis of the risk factors for lesion rupture. Journal of Neurosurgery, 103(4), pp. 662-680.

[85] Parlea, L., Fahrig, R., Holdsworth, D. W., and Lownie, S. P., 1999, An analysis of the geometry of saccular intracranial aneurysms. AJNR. American Journal of Neuroradiology, 20(6), pp. 1079-1089.

[86] Ujiie, H., Tachibana, H., Hiramatsu, O., Hazel, A. L., Matsumoto, T., Ogasawara, Y., Nakajima, H., Hori, T., Takakura, K., and Kajiya, F., 1999, "Effects of size and shape (aspect ratio) on the hemodynamics of saccular aneurysms: a possible index for surgical treatment of intracranial aneurysms," Neurosurgery, 45(1), pp. 119-129; discussion 129-130.

[87] Ujiie, H., Tamano, Y., Sasaki, K., and Hori, T., 2001, "Is the aspect ratio a reliable index for predicting the rupture of a saccular aneurysm?" Neurosurgery, 48(3), pp. 495-502; discussion 502-493.

[88] Cebral, J.R., M.A. Castro, S. Appanaboyina, C.M. Putman, D. Millan, and A.F. Frangi, Efficient pipeline for image-based patient-specific analysis of cerebral aneurysm hemodynamics: Technique and sensitivity. IEEE Trans Med Imag, 2005. 24(1): p. 457-467.

[89] Ford, M.D., N. Alperin, S.H. Lee, D.W. Holdsworth, and D.A. Steinman, Characterization of volumetric flow rate waveforms in the normal internal carotid and vertebral arteries. Physiol Meas, 2005. 26: p. 477-488.

[90] Cebral, J.R., M.A. Castro, C.M. Putman, and N. Alperin, Flow-area relationship in internal carotid and vertebral arteries. Physiol Meas, 2008. 29: p. 585-594.

[91] Mut, F., R. Löhner, A. Chien, S. Tateshima, F. Viñuela, C.M. Putman, and J.R. Cebral, Computational hemodynamics framework for the analysis of cerebral aneurysms. Int J Num Meth Biomed Eng, 2011. 27(6): p. 822-839.

[92] Byrne, G., F. Mut, and J.R. Cebral, Quantifying the large-scale gemodynamics of intracanial aneurysms. AJNR Am J Neuroradiol, 2014. 35(2): p. 333-338.

[93] Hill, Michael (2012) A novel approach for combining biomechanical and micro-structural analyses to assess the mechanical and damage properties of the artery wall. Doctoral Dissertation, University of Pittsburgh.